Mechanosensing and Routes of Glioblastoma Dissemination

A THESIS SUBMITTED TO

THE FACULTY OF MEDICINE AND HEALTH

OF THE UNIVERSITY OF SYDNEY

IN FULFILMENT OF THE REQUIREMENTS FOR THE DEGREE OF

DOCTOR OF PHILOSOPHY

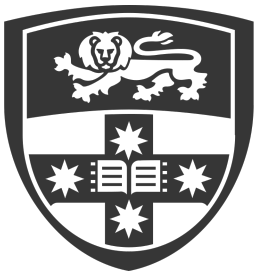

THE UNIVERSITY OF SYDNEY

Dr Thuvarahan Jegathees BSc(Adv), MD

Faculty of Medicine and Health

The University of Sydney

May 2025

Mechanosensing and Routes of Glioblastoma Dissemination

Dr Thuvarahan Jegathees BSc(Adv), MD

Supervisor: Professor Geraldine O'Neill

The Children's Hospital at Westmead, Westmead
Faculty of Medicine and Health
The University of Sydney

This research reported in this thesis was supported by the award of a Research Training Program scholarship to the PhD Candidate.

Copyright in Relation to This Thesis

Statement of Original Authorship

The work contained in this thesis has not been previously submitted to meet requirements for an award at this or any other higher education institution. To the best of my knowledge and belief, the thesis contains no material previously published or written by another person except where due reference is made.

Signature:

Date: 6th May 2025

Authorship Contribution Statement

Data presented in Chapter 3, Figure 3.3b has been previously published by Dr Thomas J Grundy in his PhD thesis (Grundy, T. J. (2019). *Mechanoregulation of glioblastoma by extracellular biophysical stimuli*. PhD thesis, The University of Sydney, Sydney, NSW, Australia.). Data Presented in Chapter 4, Figure 4.2 has been previously published by Dr Heeva Barharlou in his PhD thesis (Baharlou, H. (2022). *The role of Anogenital Mononuclear Phagocytes in HIV transmission*. PhD thesis, The University of Sydney, Sydney, NSW, Australia.)

Cell line maintenance, multicellular tumour spheroid generation and imaging in Chapter 3 was performed by Dr Victoria Prior, Dr Amy Sarker and Samuel Bax.

Statistical analysis of spheroid data and RNA sequencing data in Chapter 3 was performed with assistance from Dr Christoph Mark.

Sectioning, staining and imaging of thin sections presented in Chapter 4 was performed commercially through Katharina Gaus Light Microscopy Facility at The University of New South Wales.

Systematic review data presented in Chapter 5 was performed alongside Professor Geraldine O'Neill as the second reviewer.

In addition to the statements above, in cases where I am not the corresponding author of a published item, permission to include the published material has been granted by the corresponding author.

Dr Thuvarahan Jegathees
6th May 2025

As primary supervisor for the candidature upon which this thesis is based, I can confirm that the
authorship attribution statements above are correct.

Professor Geraldine O'Neill
6th May 2025

To my family, old and new

Abstract

Gliomas are the most common malignant primary brain tumours, with high-grade gliomas (HGG) such as glioblastoma multiforme (GBM) showing significant resistance to current standard-of-care treatment approaches of extensive surgical removal and chemoradiation. Despite extensive research efforts over the past few decades, patient outcomes remain unfavourable, highlighting the need to understand the causes of therapeutic failure.

The dynamic interaction between the tumour and its surrounding tumour microenvironment (TME) is increasingly recognised as a key driver of cellular migration, tumour diversity, and resistance to therapy. In addition to ongoing research on the biochemical composition and architecture of the TME, recent investigations point to the increasing importance of the mechanical characteristics of the TME in driving GBM invasion and migration. Understanding the influence of these biophysical aspects of the TME on the heterogeneity and adaptation of GBM is essential for developing novel therapies to present new avenues for treatment. Specifically, the poor progression of therapies designated as successful in pre-clinical studies into clinical practice has been attributed to an incomplete understanding of the mechanical properties of the TME, the mechanisms

of mechanical signal transduction, and the influence of surrounding cells on this process.

This thesis explored how cell-cell interactions influence HGG migration within a spheroid model using patient-derived GBM cells on biomechanically relevant substrates. The findings revealed unique and shared migration patterns among different cell lines, highlighting a complex interaction between the cell-cell and cell-substrate dynamics that may be facilitated by focal adhesions (FA) and that this interaction is likely independent of the GBM subtype. Furthermore, the impact of cell-cell interactions and cell-substrate adhesions in a mouse xenograft model with the same patient-derived cell lines highlighted the role of epithelial growth factor receptor (EGFR) and focal adhesion kinase (FAK) signalling in directing GBM invasion routes. The viscoelastic characteristics of the brain under conditions of health, disease, and treatment were investigated through a systematic review of the literature. This review emphasises the lack of longitudinal data on how the mechanical properties of the brain change with therapy, a necessary understanding for the development of innovative and more precise treatments for HGG. Overall, this body of work provides insight into the role of the mechanical properties of TME in directing the GBM dissemination routes in the hope of generating successful therapies for this debilitating disease.

Acknowledgments

It feels almost unreal as I prepare to submit this work, which has encompassed the past eight years of my life. This thesis owes its existence to the patience, support, and generosity of numerous individuals, to whom I extend my sincere gratitude.

Firstly, I express my gratitude to my supervisor, Geraldine. When I first stepped into your office as a first-year medical student eager to delve into research, I was captivated by your passion for the field, your constant friendly demeanour, and your brilliance. Despite my shifts in medical training specialities, relocating to various hospitals, and even being interstate for two years, you have remained a constant figure in my career. People often ask why I continued to pursue research in GBM while now training in Dermatology, and the answer is clear. It's because mentors like you are a rare find. Therefore, I am immensely thankful for your unwavering support, your flexibility with my often chaotic schedule, and your motivation, particularly when it came to writing. I am grateful for the numerous hours you have dedicated to reviewing my data, revising my writing, and subsequently revisiting it when it was not up to standard. Thank you for instilling in me a commitment to uphold the highest standards in my work—a principle I will carry

throughout my career. I am deeply grateful for your inspiration and encouragement to continue to reach higher. I am truly lucky to have you as my supervisor.

Over the past eight years, I have had the privilege of collaborating with numerous individuals to whom I am deeply grateful. To Kaitlyn and Tom, thank you for warmly welcoming me when I first joined and introducing me to the GONspel, which forms the foundation of my scientific approach. To Aysen and Yuyan, I appreciate your patience in addressing all my questions and requests and your constant readiness to assist me. To Victoria, Amy, and Sam, thank you for always being available for a chat whenever I unexpectedly visited the lab, and for your support whenever I was away from Westmead. Without your contributions, half of the data in my thesis might not exist. To Christoph, I am grateful for your assistance with my statistics questions, even from halfway across the globe! To Maninda, what started as a fortunate coincidence of being on the same floor grew into unwavering support both inside and outside the lab—thank you.

To the many who have grown up with me in the 2145, thank you for your patience when work got a bit busy, and then also thank you for convincing me that I need to take a break to maintain my sanity. You have all been an integral part of my life for as long as I can remember.

To Amma, Appa, and Sharuja, I am grateful for your love, your constant inquiries into my PhD progress, and for delivering snacks to my desk in the early stages of my studies. I owe you thanks for nurturing curiosity and wonder in my upbringing and for prompting me to discover new things. I would also like to thank my extended family, old and new, in Sydney, Melbourne, and beyond, for assisting with all the relocations in recent years,

ensuring I had a place to pursue my research, and for always being there as a source of support when I faced challenges.

To Sonea, I struggle to express the depth of gratitude I have for your assistance throughout this journey. It's funny to think that your entire time with me has been during my PhD candidature so I am looking forward to when we can do things without my PhD being a constant focus. I'm deeply thankful for everything you've shouldered at home, especially over these past few years, to support me. I love you.

Table of Contents

Abstract **vii**

Acknowledgments **ix**

Nomenclature **xxiii**

List of Figures **xxxiv**

List of Tables **xxxvii**

1 Literature Review **1**

1.1 Glioblastomas are High Grade Gliomas 1

1.1.1 Primary and Secondary GBM 3

1.1.2 Histology of GBM 3

1.1.3 Molecular Landscape of GBM 4

1.1.4 Anatomical Locations of GBM 9

1.2 Management of GBM 10

1.2.1 Role of O(6)-methylguanine-DNA methyltransferase (MGMT) . 12

1.2.2 Mechano-Pharmacology 13

1.3 GBM as an Invasive Disease 15

1.3.1 Secondary Structures of Scherer 17

1.4 Tissue Mechanics in the Brain in Development and Disease 18

1.5 Mechanosensitive Migration and Invasion of HGG 24

1.5.1 Mechanosensation 26

1.6 Measurement of Tissue Stiffness 30

1.6.1 Young's Modulus 31

1.6.2 Brain Tissue is Viscoelastic 32

1.6.3 Magnetic Resonance Elastography as A Non-Invasive Approach to Measure Stiffness 34

1.7 Primary Patient Derived Cells 35

1.8 Modelling the Mechanical Properties of the Brain 37

1.8.1 2D Models of The Brain Mechanobiology 38

1.8.2 Increased Dimensionality with 3D Models 38

1.8.3 Spheroids as a Model of GBM 40

1.8.4 Gold Standard: Xenografts 41

1.9 Study Aims and Overview 43

2 Materials And Methods **45**

2.1 Materials 45

2.1.1 Chemicals, reagents and commercially purchased kits 45

2.1.2 Solutions 49

2.1.3 Antibodies 50

2.1.4 Microscope Systems 53

2.1.5 Software 55

2.2 Cell Biology Techniques 55

2.2.1 Glioblastoma Cell Lines 55

2.2.2 Primary Tumour Cell Line Maintenance 58

2.2.3 Spheroid Formation and Culture 60

2.2.4 Spheroid Invasion Assay 61

2.2.5 Mouse Xenograft Models 62

2.3 Immunohistology And Microscopy 63

2.3.1 Tissue Blocks 63

2.3.2 Tissue Sectioning of Thick Sections 64

2.3.3 Deparaffinisation and Rehydration of Thick Sections 64

2.3.4 Fluorescence immunohistochemistry of thick tissues 64

2.3.5 Measurement of Auto-Fluorescence Spectra 65

2.3.6 Assessment of Effect of Auto-Fluorescence Quenching 66

2.3.7 Immunofluorescence Analysis of Thin Sections 67

2.3.8 OPAL Multiplex Immunofluorescence Imaging of Thin Sections . 69

2.3.9 Image analysis of thin histological sections 71

2.4 Spheroid Invasion Assay Imaging 74

2.4.1 Pre-processing of Spheroid Invasion Assay Images 75

2.4.2 High Throughput Analysis of Spheroid Core 77

2.4.3 High Throughput Analysis of Spheroid Periphery 79

2.4.4 High Throughput Analysis of Cells Migrating as a Group Using a Spheroid Assay 82

2.5 Systematic Review 86

2.5.1 Search Methods 86

2.5.2 Study Screening 87

2.5.3 Data Extraction 88

2.5.4 Data Analysis 90

3 Mechano-Regulation of Single-Cell & Multi-cellular Emigration 91

3.1 Tumour Spheroid Model 93

3.1.1 Migration of HGG Cells From the Spheroid Bulk Form Distinct Regions . . . 94

3.1.2 Initial Migration of HGG Cells From the Spheroid Vary Between Cell Lines . . . 95

3.1.3 Morphological Distinctions of Migrating Cells Inherent to Cell Lines and Substrate Stiffness . . . 100

3.2 Single-Cell Emigration . . . 103

3.2.1 Stiffer Substrates Increase Single-Cell Emigration . . . 105

3.3 Collective-Cell Emigration . . . 106

3.3.1 The Area of Collective-Cell Emigration from the Spheroid is Dynamic . . . 108

3.3.2 Substrate Stiffness Influences the Proportion of Collective Emigration . . . 109

3.4 Focal Adhesions May Be Implicated In Mechanosensitive Behaviour . . . 113

3.4.1 Cell-lines Differ in the Fraction of Differentially Expressed Genes using RNA-Sequencing . . . 113

3.4.2 Association of Differentially Expressed Genes with Emigration Pattern . . . 114

3.5 Chapter Discussion:Cells Act Differently When They Socialise as A Group 115

3.5.1 The Influence of The Mechanical Environment on Morphology and Emigration of HGG Cells 118

3.5.2 Genetic Basis for Mechanosensation 122

3.5.3 Considerations of Using a Canny Edge Detection tool to measure the Collective Area of Single-Cell Emigration 124

3.6 Concluding Remarks 125

4 Relationship Between Spatial Arrangement of Glioblastoma Cells and Protein Expression 127

4.1 Thick Section Analysis Is Hampered By Auto-Fluorescence 129

4.1.1 Auto-fluorescence of FFPE Sections is a Hindrance to Multiplex IF 130

4.1.2 Sudan Black B Quenches Auto-Fluorescence in Thick FFPE Sections but Also Hinders Staining 132

4.2 The Opal Staining Method 136

4.2.1 IHC and Uniplex IF Validation 136

4.2.2 Mulitplex IF Validation 140

4.2.3 Multiplex IF of Study Sections 140

4.2.4 Segmentation of Cells and Blood Vessels 146

4.2.5 Classification of GBM Cells Migrating Individually or in a Cluster 147

4.2.6 Cell-Line Specific Associations with Blood Vessels 149

4.2.7 Cell-Line Specific Behaviours in Individually Migrating Cells and Cell Migration in Clusters 149

4.2.8 Cell-Line-Dependent Phosphorylation of EGFR is Correlated to the Distance From Blood Vessel 157

4.2.9 Cell-Line-Dependent FAK Phosphorylation is Correlated to the Distance From Blood Vessel 157

4.2.10 The Correlation of EGFR Phosphorylation to the Distance from Blood Vessels is Diminished in Single-Cell Migration in a Cell-Dependent Manner 158

4.2.11 The Correlation of FAK Phosphorylation to the Distance from Blood Vessels is Diminished in Single-Cell Migration in a Cell-Dependent Manner 163

4.3 Chapter Discussion 164

4.3.1 The Difficulties of IF on Thick FFPE Sections 164

4.3.2 Single-Cells Cells Differ From Cells Which Cluster 166

4.4 Concluding Remarks 171

5 Mechanical Properties of Brain Tumours and Normal Brain 173

5.1 Literature Search 174

5.2 Data Extraction 177

5.3 Data Analysis 178

5.4 Storage Modulus of Normal Brain 181

5.5 Loss Modulus of Normal Brain 186

5.6 Shear Modulus of Normal Brain 189

5.7 Complex Shear Modulus of Normal Brain 191

5.8 MRE of Human Brain Tumours 194

5.9 MRE on Animal Brain 199

5.10 Chapter Discussion 200

5.10.1 Stiffness Values are Influenced by Measurement Modality 200

5.10.2 Brain Tumours 203

5.10.3 Modelling in the Murine brain 205

5.10.4 Future Directions 206

5.11 Chapter Conclusions 208

6 Conclusions and Outlook **211**

6.1 Cell-Cell Interactions Modulate Mechanosensation 212

6.2 EGFR and FAK Signalling May Direct Routes of Dissemination 214

6.3 MRE Stiffness Values are Influenced by Measurement Modality, Transducer Frequency and Region of Interest 216

6.4 Conclusion 217

Literature Cited **281**

Nomenclature

Abbreviations

.png	portable network graphic
ABCG2	ATP binding cassette subfamily G member 2
AF	autofluorescence
AFM	atomic force microscopy
ANOVA	analysis of variance
APS	ammonium persulfate
ATP	adenosine triphosphate
bFGF	basic fibroblast growth factor
BSA	bovine serum albumin
CAM	cell adhesion molecules
CDK4	cyclin-dependent kinase 4
CDK6	cyclin-dependent kinase 6

Continued on next page

(Continued)

CNS	central nervous system
CS	combined score
CSC	cancer stem cells
DAB	3,3-diaminobenzidine
DAPI	4,6-diamidino-2-phenyindole
DLS	digital light sheet
DMEM	Dulbecco's Modified Eagle Medium
DMSO	dimethyl sulfoxide
DPBS	Dulbecco's phosphate buffered solution
ECM	extracellular matrix
EDTA	ethylenediamine tetra-acetic acid
EGF	epithelial growth factor
EGFR	epithelial growth factor receptor
F-actin	actin filament
FA	focal adhesions
FAK	focal adhesion kinase
FBS	fetal bovine serum
FFPE	formalin-fixed, paraffin-embedded

Continued on next page

(Continued)

FGF2	fibroblast growth factor basic
G-actin	globular actin
GBM	glioblastoma multiforme
GelMA	gelatin methacrylate
GFR	growth factor reduced
GLUT1	glucose transporter 1
GNS	Glioma NeuralStem Media
GSEA	gene set enrichment analysis
HE	haematoxylin and eosin
HA	hyaluronic acid
HAMA	HA methacrylate
HCl	hydrochloric acid
HGG	high grade glioma
HIER	heat induced epitope retrieval
HLA	human leukocyte antigen
HRP	horseradish peroxidase
HTS	high throughput system
IDH1	isocitrate dehydrogenase 1

Continued on next page

(Continued)

IF	immunofluorescence
IGF-1	insulin-like growth factor 1
IHC	immunohistochemistry
KCl	potassium chloride
LAS	Leica application suite
LDEV	lactate dehydrogenase elevating virus
MAPK	mitogen-activated protein kinase
MCTS	multicellular tumour spheroids
MDM2	mouse double minute 2
MEM	minimal essential media
MGMT	O(6)-methyl-guanine-DNA methyl-transferase
MRE	magnetic resonance elastography
MSM	monolayer stress microscopy
mTOR	mammalian target of rapamycin
NaCl	sodium chloride
NaOH	sodium hydroxide
NF1	neurofibromatosis type 1
NSCLC	non-small cell lung cancer

Continued on next page

(Continued)

p-EGFR	phosphorylated EGFR
p-FAK	phosphorylated FAK
PAHG	polyacrylamide hydrogels
PBS	phosphate buffered solution
PDGF	platelet-derived growth factor
PDGFRA	platelet-derived growth factor receptor alpha
PEG	polyethylene glycol
PFA	para-formaldehyde
PI3K	phosphatidyl-inositol 3-kinase
PKB	protein kinase B
PMT	photomultiplier tube
PRISMA	Preferred Reporting Items for Systematic Reviews and Meta-Analysis
PROSPERO	Prospective Register of Systematic Reviews
PTEN	phosphatase and tensin homolog
QIMR	Queensland Institute of Medical Research
RB	retinoblastoma
rBM	reconstituted basement membrane
ROI	region of interest

Continued on next page

(Continued)

SBB	Sudan Black B
SCFS	single-cell force spectroscopy
SDS	sodium dodecyl sulfate
TBS	tris buffered solution
TME	tumour micro-environment
TMZ	temozolomide
TP53	tumour protein p53
TSA	tyramide signal amplification
WHO	World Health Organisation

Symbols

$\|G^*\|$	complex shear modulus
Hz	Hertz
kPa	kilopascal
G''	loss modulus
μm	micrometre
mg	milligram
mL	millilitre

Continued on next page

(Continued)

min	minute
nm	nanometre
px	pixel
μ	shear modulus
G'	storage (elastic) modulus
E	Young's Modulus

List of Figures

1.1 Stiffness of Tissues In the Body Compared to Culture Plates 18

1.2 Composition of the ECM in Normal Brain and the Subtype Specific TME in GBM 21

2.1 Plate Map Used for Spheroid Invasion Assay 62

2.2 Segmentation of Spheroid Images 83

3.1 Migration of HGG Cells From the Spheroid form Distinct Regions. 96

3.2 Migration of HGG Cells from Spheroids on Polyacrylamide Hydrogels for Four Patient-Derived Primary Cell Lines 98

3.3 Area of Spheroids After Compaction Varies Between Cell Lines 99

3.4 Morphology of Migrating HGG Cells Over Increasing Substrate Stiffness 101

3.5 Single-Cell Emigration of HGG Cells from a Spheroid is Differentially Regulated by Substrate Stiffness 104

3.6 Collective Emigration of HGG Cells is a Dynamic Process 107

3.7 Rate of Change in Collective Emigration Area 110

3.8 Switch-Point Analysis 111

3.9 Percentage of Differentially Expressed Genes in Cell Lines from the Q-Cell Database 114

3.10 Gene Set Enrichment Analysis of Differentially Expressed Genes in Cell Lines from the Q-Cell Database 116

4.1 Demonstration of Loss of Data with Thin Sections in Comparison to Thick Sections 131

4.2 Auto-fluorescence in FFPE Sections 133

4.3 Steps in Immunofluorescence 133

4.4 Comparison of the Effect of Sudan Black B on Autofluorescence Quenching 135

4.5 IHC and Uniplex IF Validation of EGFR and p-EGFR Staining 141

4.6 IHC and Uniplex IF Validation of FAK and p-FAK Staining 142

4.7 IHC and Uniplex IF Validation of HLA and GLUT-1 Staining 143

4.8 Multiplex IF on Human Placenta 144

4.9 Multiplex IF of Study Sections 145

4.10 Segmentation of HLA positive cells and GLUT-1 Positive Blood Vessels . 148

4.11 Proportion of Xenograft GBM Cells Located as Individual Cells 150

4.12 Distance of Human Xenograft GBM Cells From the GLUT-1 Positive Blood Vessels 152

4.13 Phosphorylation of EGFR and FAK in Human JK2 GBM Xenograft Relation to Distance from GLUT-1 Positive Blood Vessels in the Mouse Brain 153

4.14 Phosphorylation of EGFR and FAK in Human RN1 GBM Xenograft Relation to Distance from GLUT-1 Positive Blood Vessels in the Mouse Brain 154

4.15 Phosphorylation of EGFR and FAK in Human SJH1 GBM Xenograft Relation to Distance from GLUT-1 Positive Blood Vessels in the Mouse Brain 155

4.16 Phosphorylation of EGFR and FAK in Human WK1 GBM Xenograft Relation to Distance from GLUT-1 Positive Blood Vessels in the Mouse Brain 156

4.17 Phosphorylation of EGFR and FAK in Human JK2 GBM Xenograft in Relation to Distance from the GLUT-1 Positive Blood Vessels in the Mouse Brain, Segmented by Cells Found Individually and as Clusters 159

4.18 Phosphorylation of EGFR and FAK in Human JK2 GBM Xenograft in Relation to Distance from the GLUT-1 Positive Blood Vessels in the Mouse Brain, Segmented by Cells Found Individually and as Clusters 160

4.19 Phosphorylation of EGFR and FAK in Human SJH1 GBM Xenograft in Relation to Distance from the GLUT-1 Positive Blood Vessels in the Mouse Brain, Segmented by Cells Found Individually and as Clusters . . 161

4.20 Phosphorylation of EGFR and FAK in Human WK1 GBM Xenograft in Relation to Distance from the GLUT-1 Positive Blood Vessels in the Mouse Brain, Segmented by Cells Found Individually and as Clusters . . 162

5.1 PRSIMA Flow Diagram describing article screening and selection process. 176

5.2 Human Whole Brain Coronal Sections 180

5.3 Population estimates for storage, loss, shear and complex shear modulus of human whole brain, white matter and grey matter was determined by meta-analysis of published MRE studies in human subjects. 182

List of Tables

2.1 Chemicals, drugs & commercially purchased kits. List of all commercially purchased reagents used in this thesis. 45

2.2 Composition of Solutions Used in this Thesis 49

2.3 Primary Antibodies Used in 3,3-Diaminobenzidine (DAB) Staining . . . 50

2.4 Primary Antibodies Used In Monoplex IF. The antigen retrieval buffer used, incubation time and the OPAL secondary pair used is also listed . . 51

2.5 Primary Antibodies Used In Multiplex IF. The order of the antibodies used, antigen retrieval buffer used, incubation time and the OPAL secondary pair used is also listed 52

2.6 Microscope Systems Used 53

2.7 Major Genetic and Epigenetic Features of GBM Cell Lines 56

2.8 Characterisation Data of Patient-Derived GBM Cell Lines Used In This Thesis 57

2.9 QuPath Settings for Cell Detection 72

2.10 QuPath Settings for Blood Vessel Segmentation 73

3.1 Morphology of individually emigrating HGG cells, relative to substrate stiffness 103

3.2 Comparison of Morphology and Emigration of HGG Cells During Single-Cell Emigration on Soft and Stiff Substrates 106

3.3 Behaviour of HGG cells during Single-Cell and Collective Emigration . . 112

4.1 Staining patterns expected and seen in IHC and IF staining 138

4.2 QuPath Settings for Cell Detection 146

4.3 QuPath Settings for Blood Vessel Segmentation 147

4.4 Mean Distance away from blood vessels (μm) for JK2, RN1, SJH1 and WK1 human GBM xenograft in mouse brain 151

5.1 Population estimates for storage modulus of human brain and sub-regions 183

5.2 Population estimates for loss modulus of human brain and sub-regions . . 186

5.3 Population estimates for shear modulus of human brain and sub-regions . 190

5.4 Population estimates for complex shear modulus of human brain and sub-regions 192

5.5 Population estimates for storage, loss, and complex shear modulus of human brain tumours in published MRE studies 196

5.6 Population estimates for storage, loss, and complex shear modulus of animal brain tumours with or without healthy controls 199

Chapter 1

Literature Review

1.1 Glioblastomas are High Grade Gliomas

Gliomas are brain tumours that arise from non-neural cells called glial cells. They constitute 28% of all brain tumours and 80% of malignant brain tumours (Ostrom et al. [2015], Weller et al. [2015]). There are four types of glial cells in the central nervous system (CNS); microglia, ependymal cells, oligodendrocytes, and astrocytes. With the recent revision of the World Health Organisation (WHO) Classification of Central Nervous System Tumours in (2021), gliomas are now classified into tumour types based on both histopathologic appearance and well established molecular parameters into the groups (Louis et al. [2016, 2021], Reifenberger et al. [2017], Wirsching et al. [2016]):

- Adult-type diffuse gliomas
- Paediatric-type diffuse low-grade gliomas

- Paediatric-type diffuse high-grade gliomas
- Circumscribed astrocytic gliomas
- Glioneuronal and neuronal tumours
- Ependymomas

In addition to tumour typing, each type of tumour is assigned a histological grade, based on the presence or absence of anaplastic features, reflected in the degree of malignancy and the presumed natural course of the disease. This grade ranges from WHO grade 1 to 4, with WHO grade 1 indicating the least malignant behaviour and WHO grade 4 indicating the most malignant behaviour (Louis et al. [2021], Reifenberger et al. [2017]).

Glioblastoma, *isocitrate dehydrogenase* (*IDH*)-wild-type (GBM), a WHO grade 4 glioma, is the most common malignant primary brain tumour in adults and accounts for 15% of all primary tumours, 45% of all primary brain tumours and >54% of all gliomas (Ostrom et al. [2013, 2015], Rosenthal et al. [2006]). According to the most recent revision of the WHO Classification of Central Nervous System Tumours (Louis et al. [2021]), GBM falls into the category of the adult-type diffuse glioma family that also includes astrocytoma *IDH*-mutant (WHO grade 2, 3, or 4) and oligodendroglioma, *IDH*-mutant and 1p/19q-codeleted (WHO grade 2 or 3). The annual incidence of GBM is 3.4 per 100,000 in Australia with a slight male predominance reported in both Australia and the United States. The causes of this asymmetric distribution have yet to be elucidated (Dobes et al. [2011], Gan et al. [2015], Ostrom et al. [2013], Rosenthal et al. [2006], Smoll et al. [2013]).

1.1.1 Primary and Secondary GBM

Most GBM arise de novo ("primary" GBM), that is, they occur as tumours without clinical, histopathological or radiological evidence of a less malignant precursor lesion and typically occur in older patients with a mean age of 53-61 years (Nobusawa et al. [2009], Ohgaki et al. [2004], Parsons et al. [2008]). In contrast, "secondary" GBM arise from the malignant transformation of WHO grade II and II gliomas, are quite rare, and have a mean age of diagnosis of 33-48 years (Nobusawa et al. [2009], Parsons et al. [2008]).

1.1.2 Histology of GBM

GBM are distinguished histologically by the presence of a focal "core" of necrosis, surrounded by layers of tumour cells moving away from the necrotic core called pseudopalisades forming a "halo" (Brat et al. [2004], Rong et al. [2006]). In addition, GBM typically have microvascular proliferation and glomeruloid vascular structures (Louis et al. [2016], Rojiani and Dorovini-Zis [1996], Weller et al. [2015]), which contribute to the highly aggressive nature of these tumours. This is reflected in the extremely poor prognosis of the tumour, echoed by a median survival of just under 15 months and a 5-year survival rate of only 3-5% (Gan et al. [2015], Ostrom et al. [2014], Rosenthal et al. [2006], Stupp et al. [2005]).

A poor prognosis underscores the need to improve existing treatment protocols, which simply extend patient survival by a few months (Stupp et al. [2005]). This is in part due

to the fact that GBM is highly heterogeneous with a variety of functionally diverse cell types. Furthermore, tumour cells exhibit a highly infiltrative phenotype, resulting in very indistinct tumour margins. (Aum et al. [2014], Giese et al. [2003], Koo et al. [2012], Møller et al. [2013], Weller et al. [2015]).

1.1.3 Molecular Landscape of GBM

In 2006, Phillips et al. pioneered the classification of gliomas through a DNA microarray of glioma samples and examined the differential expression of markers associated with clinical outcome, revealing three main subclasses of gliomas; proneural, mesenchymal and proliferative. Of 183 grade 4 glioma samples examined, 31% were proneural, 20% were proliferative, and 49% were mesenchymal (Phillips et al. [2006]). Verhaak et al. furthered this study in 2010 to classify 200 gliomas into 4 subtypes; classical, mesenchymal, neural, and proneural (Verhaak et al. [2010]). The findings of a more recent comprehensive analysis of the glioma tumour transcriptome by Wang et al. have reverted the number of glioma molecular subtypes to the original 3 proposed by Phillips et al., with the existence of neural classification in the Verhaak et al. study probably due to contamination of non-GBM cells in the samples used (Wang et al. [2017]).

GBM mutations converge primarily in three main signalling pathways that are frequently activated: the PI3K – AKT – mTOR and Ras / MAPK / ERK pathways, the p14 ARF – MDM2 – MDM4 – p53 pathway, and the CDK4 / 6 - CDKN2A / B - RB1 cell cycle pathway (Ah-Pine et al. [2023], Brennan et al. [2013]). Up to 90% of GBM possess at least one activation alteration in the PI3K pathway, including *RTK*, *PI3K*, and

PTEN, which along the MAPK pathway, regulate many cellular processes such as cell proliferation (Brennan et al. [2013]). In this modification, PTEN plays a crucial role in endowing a more proliferative phenotype, with its mutations or deletions occurring exclusively to PI3K mutations. Regarding the MAPK pathway, NF1 is either deleted or mutated in 10% of the cases and never co-occurs with BRAF alterations, which are present in 2% of gliomas (Brennan et al. [2013]). Up to 90% of GBM have an altered p53 pathway which is commonly altered in many different cancers. Analysis of whole-exome sequencing data from 291 patients revealed that mutations or deletions of *TP53* (28%), amplifications of *MDM1/2/4* (15%), and deletions of *CDKN2A* (58%) comprise the majority of p53 pathway alterations (Brennan et al. [2013]). Similarly, up to 80% of GBM have an alteration in the pRB pathway, representing a cell cycle checkpoint, with alterations including *CDKN2A* deletions, amplifications of *CDK4/CDK6*, and inactivating alterations of *RB1* (Brennan et al. [2013]). In general, these alterations of the molecular pathways of GBM result in persistent activation of cell proliferation signals and resistance to apoptotic signals, while also allowing cells to bypass cell cycle checkpoints, senescence, and apoptosis (Alifieris and Trafalis [2015], Brennan et al. [2013], Uyar [2022]).

Originally, the classifications of GBM into classical, proneural and mesenchymal subtypes depended on the expression patterns of more than 600 genes; however, later research has demonstrated that this can be effectively simplified to a dependence on only 12 genes, with Acyl-CoA Synthetase Bubblegum Family Member 1 (*ACSBG1*) and Potassium Voltage-Gated Channel Modifier Subfamily F Member 1 (*KCNF1*) helping define

the classical subtype; Purinergic Receptor P2X 7 (*P2RX7*), Stathmin 4 (*STMN4*), SRY-Box Transcription Factor 10 (*SOX10*), and Erb-B2 Receptor Tyrosine Kinase 3 (*ERBB3*) helping define the proneural subtype; and S100 Calcium Binding Protein A1 (*S100A*), DAB Adaptor Protein 2 (*DAB2*), Transforming Growth Factor Beta 1 (*TGFB1*), Thrombospondin 1 (*THBS1*), Collagen Type I Alpha 1 Chain (*COL1A1*) and Collagen Type I Alpha 2 Chain (*COL1A2*) defining the mesenchymal subtype with excellent concordance (Ah-Pine et al. [2023], Behnan et al. [2017], Chen et al. [2012]).

The classical subtype is characterised by a highly proliferative phenotype often associated with the loss of chromosome 10 and the amplification of chromosome 7, along with the amplification of epithelial growth factor receptor (*EGFR*). Additionally, altered levels of pro-apoptotic proteins, as well as components of the mitogen-activated protein kinase (MAPK) pathway, and variations in Notch1 and Notch3 proteins are often described (Brennan et al. [2013], Verhaak et al. [2010], Xie et al. [2014]). Median age at diagnosis is 58 years with survival reported as 15.2 months (95% CI: 14.1-17.7 months) after diagnosis (Chen et al. [2017b], Wang et al. [2017]).

In contrast, the mesenchymal phenotype describes a more invasive phenotype, characterised by low expression of neurofibromatosis Type 1 (*NF1*), which encodes neurofibromin that functions as a negative regulator of RAS signaling, on chromosome 17q11.2, point mutations in phosphatase and tensin homolog (*PTEN*) and tumour protein p53 (*TP53*), activation of the MAPK pathway, and downregulation of mammalian target of rapamycin (mTOR) signalling (Verhaak et al. [2010]). Median age at diagnosis is 58 years with survival reported as 12.5 months (95% CI:11.4-16.2 months) after diagnosis

(Chen et al. [2017b], Wang et al. [2017]).

The proneural subtype is associated with amplifications in platelet-derived growth factor receptor alpha (*PDGFRA*), *TP53*, cyclin-dependent kinase 4 (*CDK4*), cyclin-dependent kinase 6 (*CDK6*), and frequent isocitrate dehydrogenase 1 (*IDH1*) mutations, activation of phosphatidylinositol 3-kinase (PI3K), and inhibition of the translation repressor *4EBP1* (Verhaak et al. [2010]). Compared to the other two subtypes, the proneural subtype is associated with a younger median age at diagnosis of 52 years and median survival after diagnosis of 11.1 months (95% CI: 8.47-13.83 months) (Chen et al. [2017b], Furnari et al. [2007], Verhaak et al. [2010], Wang et al. [2017], Watanabe et al. [1996], Yan et al. [2009]).

Further classification of gliomas based on *IDH1* mutational status to predict prognosis have also been proposed (Louis et al. [2016, 2021]). Traditionally in the clinical setting, GBM has been designated as “primary”or “secondary” based on the presence or absence of a pre-existing lesion (Kleihues and Ohgaki [1999], Ohgaki and Kleihues [2005, 2007]). Before the discovery of mutations in the metabolic enzyme IDH1 as a potential molecular marker (Balss et al. [2008], Nobusawa et al. [2009], Parsons et al. [2008], Yan et al. [2009]), these designations were more clinical concepts rather than strict diagnostic terms, since primary and secondary GBM are histologically indistinguishable (Kleihues and Ohgaki [1999]). However, further insights in genetics and epigenetics have allowed the WHO in 2016 to divide GBM into *IDH*-wildtype GBM and *IDH*-mutant GBM, with *IDH*-mutants conferring a recurrent phenotype (Balss et al. [2008], Louis et al. [2016], Nobusawa et al. [2009], Parsons et al. [2008], Yan et al. [2009]).

According to WHO CNS5, introduced in 2021, a GBM is now defined in adult *IDH*-wildtype diffuse and astrocytic glioma by the presence of microvascular proliferation or necrosis or *TERT* promoter mutation or *EGFR* gene amplification, or 7 (gain)/10 (loss) chromosome alterations as there is evidence that the presence of 1 or more of 3 genetic parameters (*TERT* promoter mutation, *EGFR* gene amplification, combined gain of entire chromosome 7 and loss of entire chromosome 10) is sufficient to assign a WHO grade 4 (Louis et al. [2021]). Conversely, all *IDH*-mutant diffuse astrocytic tumours are categorised as one type—Astrocytoma*, IDH-mutant*—and assigned a CNS WHO grade of 2, 3, or 4. Additionally, grading now incorporates more than just histology; a *CDKN2A/B* homozygous deletion elevates the tumour to CNS WHO grade 4, even if there is no microvascular proliferation or necrosis (Louis et al. [2021]).

IDH1, an enzyme in the citric acid cycle, is commonly mutated in secondary GBM (53-63%) and grade II and II gliomas (59.9%), but not primary GBM (7-14%), and so is used as a marker of "secondary" GBM (Li et al. [2015], Zou et al. [2013]). *IDH*-wildtype GBM and *IDH*-mutant gliomas are distinct entities which develop in patients of different age groups and have significantly different clinical outcomes (Louis et al. [2016], Ohgaki et al. [2004], Ohgaki and Kleihues [2005, 2007, 2013], Weller et al. [2015]).

Approximately 90% of grade 4 gliomas occur as *IDH*-wildtype GBM tumours typically occur in older patients with a mean age of 53-61 years (Nobusawa et al. [2009], Ohgaki et al. [2004], Parsons et al. [2008]). *IDH*-wildtype GBM are characterised by overexpression of *EGFR* (63% in IDH-wildtype GBM vs 10% in *IDH*-mutant gliomas) (Agnihotri et al. [2013], Ohgaki and Kleihues [2007], Watanabe et al. [1996]); loss of

heterozygosity of chromosome 10q which contains the tumour suppressor *PTEN* (25% in *IDH*-wildtype GBM vs 4% in *IDH*-mutant GBM) (Agnihotri et al. [2013], Ohgaki et al. [2004], Ohgaki and Kleihues [2007]); overexpression of mouse double minute 2 (*MDM2*) (31% in *IDH*-wildtype GBM vs 0% in *IDH*-mutant GBM) (Agnihotri et al. [2013], Biernat et al. [1997], Ohgaki and Kleihues [2007]); and deletion of *p16* (31% in *IDH*-wildtype GBM vs 19% in *IDH*-mutant GBM) (Agnihotri et al. [2013], Ohgaki et al. [2004], Ohgaki and Kleihues [2007]). In contrast, *IDH*-mutant GBM are quite rare, and have a mean age of diagnosis of 33-48 years (Nobusawa et al. [2009], Parsons et al. [2008]). *IDH*-mutant GBM are characterised by mutations in *TP53* (65% in *IDH*-mutant GBM vs 28% in *IDH*-wildtype GBM) (Agnihotri et al. [2013], Ohgaki et al. [2004], Ohgaki and Kleihues [2007]); hypermethylation of the retinoblastoma (*RB*) promoter (43% in *IDH*-mutant GBM vs 14% in *IDH*-wildtype GBM) (Agnihotri and Zadeh [2016], Nakamura et al. [2001], Ohgaki and Kleihues [2013]); and loss of heterozygosity of *19q* (54% in *IDH*-mutant GBM vs 6% in *IDH*-wildtype GBM) (Agnihotri et al. [2013], Nakamura et al. [2000], Ohgaki and Kleihues [2007]).

1.1.4 Anatomical Locations of GBM

Most GBM tumours are found in the supertentoral compartment of the cranial cavity, most commonly found in the frontal, temporal, and parietal lobes in that order; however, they have also been reported in the cerebellum, brainstem, and spinal cord (Gan et al. [2015], Ostrom et al. [2013], Wirsching et al. [2016]). Despite the highly invasive nature of GBM, tumour cells rarely metastasise from the site of origin (less than 1% of all cases),

and local invasion and tumour recurrence are the leading causes of death (Cuddapah et al. [2014], Garcia-Diaz et al. [2023], Gupta et al. [2024], Ostrom et al. [2015], Pietschmann et al. [2015], Weller et al. [2015]). Possibly, the short survival time after diagnosis may explain the rarity of metastatic GBM cases which have been reported in the lungs, lymph nodes and bones (Pasquier et al. [1980], Piccirilli et al. [2008]). Alternatively, the unique vasculature of the brain, in particular the presence of the blood-brain barrier, may provide an additional barrier to metastasis (Lun et al. [2011]). The exact mechanism of extra-neural metastasis of GBM remains unclear, however, direct penetration through the dura mater and bone, venous spread through the leptomeningeal sinuses or intra-cerebral veins, and lymphatic outflow of cerebrospinal fluid into extra-neural tissues have been postulated as potential mechanisms (Majd et al. [2024]).

1.2 Management of GBM

The standard of care for those with a diagnosis of GBM is surgical debulking of the tumour, and, where feasible, maximal surgical resection is preferred (Weller et al. [2014]). However, a study conducted in Australia found that only 32% newly diagnosed GBM patients were able to undergo a gross macroscopic resection, with 37% of these patients receiving a partial debulking surgery and 24% of GBM patients having only had a biopsy performed (Gan et al. [2015]). Of these patients, 87% were referred for postoperative treatment, with 69% receiving some form of postoperative treatment. The most common reasons for non-referral included multiple co-morbidities, neurological deficits, perceived poor prognosis, or advanced age (Gan et al. [2015]).

The benefits of radiation therapy and the dose response relationship in GBM have been known for many decades (Gzell et al. [2017], Walker et al. [1979]). Before 2005, surgical intervention was followed by radiotherapy as standard clinical practice with only occasional use of chemotherapy, as the benefits of chemotherapy in these situations were generally considered modest (Gan et al. [2015], Stewart [2002]). However, a landmark clinical study by Stupp et al., the EORTC 26981/NCIC-CE3 Phase 3 study, found that concurrent treatment (84% of patients had previous debulking surgery) with radiotherapy and the alkylating agent temozolomide (TMZ) (75 mg/m2 per day) followed by 6 months of TMZ (150-200 mg/m2 for 5 days during each 28-day cycle) increased the median overall survival time from 12.1 months for those receiving radiotherapy alone to 14.6 months for those receiving both radiotherapy and TMZ. Since 2005, the Stupp protocol has been widely adopted with similar survival improvements in the Australian population (Gan et al. [2015], Stupp et al. [2005]).

An additional study in Australian patients treated with the Stupp protocol evaluated the time to recurrence, indicating a median progression period of 7.0 months (Parakh et al. [2016]). In contrast to the initial presentation of GBM, there is no standard of care in the management of recurrent glioblastoma, with no survival benefit in repeat surgery for recurrent GBM unless complete resection can be achieved (González et al. [2022], Parakh et al. [2016], Suchorska et al. [2016]). This poor prognosis highlights the need for novel approaches to treatment.

1.2.1 Role of O(6)-methylguanine-DNA methyltransferase (MGMT)

The O(6)-methylguanine-DNA methyltransferase (MGMT) status is a predictor of the response to TMZ (Hegi et al. [2005], Olson et al. [2011], Rivera et al. [2010]). TMZ causes DNA damage and cell death by transferring alkyl groups to guanine bases, which, if not repaired, causes cell apoptosis (Hegi et al. [2005], Thakkar et al. [2014]).

MGMT is a DNA repair protein that removes alkyl groups from guanine, so high levels of MGMT confer resistance to the chemotherapeutic effects of TMZ (Hegi et al. [2005], Rivera et al. [2010], Thakkar et al. [2014]). Methylation of the MGMT promoter causes silencing of the *MGMT* gene which inhibits DNA repair and therefore increases sensitivity to the effects of TMZ (Hegi et al. [2005], Watts et al. [1997]).

The promoter of *MGMT* is methylated in approximately 45-50% of newly diagnosed GBM and is associated with a more favourable prognosis (Hegi et al. [2005], Olson et al. [2011], Preusser et al. [2008]). *MGMT* methylation is commonly associated with secondary GBM, where 75% of the tumours show methylation of the promoter region of *MGMT*, compared to primary GBM where only 36% of the tumours show methylation of the promoter region of *MGMT* (Nakamura et al. [2001]). For those who received the Stupp et al. protocol, *MGMT* methylation conferred higher survival with a median duration of 21.7 months for those with methylation of the *MGMT* promoter compared to 12.7 months for those without methylation of the *MGMT* promoter (Hegi et al. [2005]).

1.2.2 Mechano-Pharmacology

Despite advancements in GBM research, there are still no robust therapies for HGG with only a handful of therapies approved for clinical use (Shergalis et al. [2018], Weller et al. [2015], Yang et al. [2022]). Radical surgical removal rarely eliminates GBM, as the widespread infiltration of GBM cells into brain tissue makes comprehensive resection unattainable. Tumour recurrence and regrowth usually occur 2-3 cm from the initial resection site due to cells that have spread beyond surgical boundaries (Cuddapah et al. [2014], Garcia-Diaz et al. [2023], Gupta et al. [2024], Jue and McDonald [2016]). Even with the implementation of the Stupp protocol, only modest survival benefits are observed (Bhargav et al. [2022], Stupp et al. [2005], Yang et al. [2022]). The limited transition of treatments that showed promise in preclinical trials to practical clinical applications has been a persistent issue in the pharmaceutical development sector with contributing factors include the reliance on non-human cells, inadequate experimental designs, and intra-tumoral heterogeneity (Krishnan et al. [2015], Stewart [2002]).

It has been increasingly recognised that the soft tumour microenvironment (TME) of the brain parenchyma alters protein expression and signalling (Budday et al. [2020], Pillai and Franze [2024], Sarker et al. [2020], Umesh et al. [2014]). Krishnan et al. introduced the term “Mechano-pharmacology” to describe how tissue mechanics influence drug target accessibility, protein expression, and molecular interactions, which ultimately determine the drug’s effectiveness *in-vivo* (Grundy et al. [2022], Krishnan et al. [2015], Sarker et al. [2020]). GBM cells exhibit greater resistance to TMZ when grown in more stiff 3D chitosan-hyaluronic acid scaffolds than in softer scaffolds, despite no differences

in cell metabolism between the two conditions (Erickson et al. [2018]). Furthermore, the ATP binding cassette subfamily G member 2 (*ABCG2*) gene, which is related to drug resistance through its function as an efflux pump for chemotherapeutic drugs like TMZ, are also upregulated in stiff scaffolds (Emery et al. [2017], Erickson et al. [2018]). Similarly, HGG cells cultured in 3D embedded polyethylene glycol (PEG) hydrogels show increased resistance to 30 μM TMZ in stiffer 26.6 kPa hydrogels with 93% tumour viability compared to 58% cell viability in 0.04 kPa hydrogels (Kondapaneni et al. [2024], Wang et al. [2021]). In contrast, other investigations have revealed that resistance to TMZ and Carmustine was significantly higher in GBM cells cultured in soft polyacrylamide hydrogels (PAHG) compared to GBM cells cultured in traditional stiff polystyrene tissue culture plates (Chang et al. [2018], Kondapaneni et al. [2024], Wang et al. [2016b]), highlighting the complex role of the TME and culture conditions in GBM resistance to conventional therapies. Whilst many therapies fail at the pre-clinical stages of drug discovery (Takebe et al. [2018]), the impact of the TME on mechano-pharmacology may elucidate the common inconsistency whereby treatments demonstrating efficacy in preclinical trials on rigid culture substrates frequently fail to produce the anticipated outcomes in human clinical environments. This situation highlights the necessity of advancing our understanding and emulation of the TME's mechanical characteristics. (Budday et al. [2020], Pillai and Franze [2024], Sarker et al. [2020], Sohrabi et al. [2023]).

It is crucial to recognise that GBM, like many other types of cancer, presents molecular heterogeneity and genetic instability, complicating research efforts (Zhang et al. [2020]). Studies have indicated that a GBM tumour sample from a single patient can

manifest multiple subpopulations of GBM at once, allowing certain cells to evade treatment. (Sottoriva et al. [2013], Stringer et al. [2019], Zhang et al. [2020]). In addition, over time, cancer tumours can develop multiple mutations, increasing genetic diversity. Consequently, single-target therapies may not always succeed in treating GBM. (Hanahan and Weinberg [2011], Shergalis et al. [2018]).

1.3 GBM as an Invasive Disease

In 2000, Hanahan and Weinberg published their seminal review: the hallmarks of cancer, whereby they distilled the complexity of cancer into six biological capabilities that are acquired during malignant transformation of normal cells (Hanahan and Weinberg [2000]). In an updated review published a decade later in 2011, two additional hallmarks and two additional traits were added. Of these, tumour invasion and metastasis are the major causes of mortality in those with cancer (Hanahan and Weinberg [2011]).

The growth of GBM is established by the proliferation of tumour cells in the growing tumour mass and subsequent invasion of the tumour cells into the surrounding brain parenchyma (Xie et al. [2014]). The invasive front significantly surpasses the borders of the contrast-enhancing lesion observed in radiological exams, frequently affecting the opposite hemisphere. (Claes et al. [2007], Dandy [1928], Earnest et al. [1988], Ganslandt et al. [2005]). Diffuse migration makes GBM particularly insulated from surgical, medical, and radiological interventions. Unlike other tumours, GBM rarely infiltrates the vasculature and lymphatic systems and thus rarely metastasises outside the CNS, rather

preferentially invades brain tissue (Beauchesne [2011], Subramanian et al. [2002], Zhong et al. [2010]).

A more recent review in 2022 has identified two additional emerging hallmarks, namely unlocking phenotypic plasticity and senescent cells, as well as two novel enabling characteristics: non-mutational epigenetic reprogramming and polymorphic microbiomes (Hanahan [2022]). The phenomenon of "unlocking phenotypic plasticity" is exemplified in GBM, where proneural tumours transition to a mesenchymal subtype following therapeutic intervention and relapse, akin to the epithelial-to-mesenchymal transition observed in various other cancers (Fedele et al. [2019], Wang et al. [2016a, 2017]). Senescent cells, characterised by cell cycle arrest mediated through the p53/p21 and/or p16/Rb pathways, exhibit distinctive attributes such as a secretory phenotype associated with senescence, an anti-apoptotic program, and augmented lysosomal content. These senescent cells have been detected within GBM, and their removal has been associated with extended survival durations in GBM mouse models (Salam et al. [2023]). Non-mutational epigenetic reprogramming is most effectively illustrated by the methylation of the promoter of the *MGMT* gene, which imparts resistance to TMZ, as detailed in section 1.2.1 (Hegi et al. [2005], Rivera et al. [2010], Thakkar et al. [2014]). Current insights into the influence of the microbiota on gliomas are increasingly recognised, with evidence indicating that alterations in the gut microbiota, induced by antibiotic therapies, lead to decreased subsets of cytotoxic natural killer cells and modifications in the expression of inflammatory and homeostatic proteins in microglia, ultimately correlated with increased glioma growth in a mouse model of glioma (D'Alessandro et al. [2020]).

1.3.1 Secondary Structures of Scherer

The brain parenchyma is a soft tissue with a low Young's modulus (E) quoted between 0.1-1 kPa (Budday et al. [2015], Butcher et al. [2009], Christ et al. [2010], Elkin et al. [2007], Taylor and Miller [2004]). In contrast, the value of E in hard tissues is estimated to be 100 kPa (Engler et al. [2006]) (Figure 1.1). The brain parenchyma itself is heterogeneous and consists of structures and regions such as grey matter, fibre tracts of white matter, and infiltrating vasculature that may provide pathways of dissemination from the tumour mass (Budday et al. [2015], Hrapko et al. [2008]). The local mechanics of the TME is influenced by the composition of the local tissue and this may influence the invasion patterns of GBM seen *in-vivo* (Budday et al. [2020], Pillai and Franze [2024]).

Histopathological studies of brains with gliomas by Scherer in 1938 demonstrated that the invasion of GBM did not occur in a random manner, but rather through distinct anatomical structures collectively referred to as the secondary structures of Scherer. These GBM cells migrate through the normal parenchyma, just below the pia of the brain (sub-pial spread), surrounding neurons (peri-neuronal spread), along existing normal blood vessels of the brain (perivascular spread), surrounding nerve fascicles (perifacicular spread) and within nerve fascicles (intra-facicular spread) (Cuddapah et al. [2014], Hambardzumyan et al. [2016], Scherer [1938]). In addition, invading GBM cells adopt the physical shape of the occupied space, so the shape of cells from the same tumour mass can appear different , depending on the structure along which they invaded (Scherer [1940]).

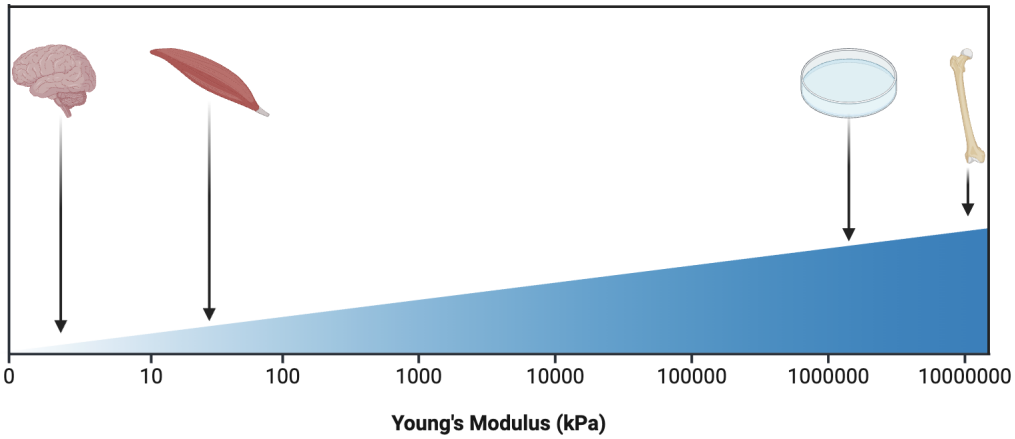

Figure 1.1: **Stiffness of Tissues In the Body Compared to Culture Plates**

Stiffness can be quantified by Young's modulus (E) which related to a material's resistance to length alteration under axial loads. (E) of brain (0.1-1 kPa) has been reported to be softer than muscle (25-100 kPa), and many magnitudes softer than bone (15,000,000 - 20,000,000 kPa) and culture plates (3,000,000 kPa) (Budday et al. [2015], Butcher et al. [2009], Christ et al. [2010], Elkin et al. [2007], Gómez-Oliva et al. [2021], Kondapaneni et al. [2024], Ogneva et al. [2010], Rho et al. [1993], Taylor and Miller [2004])

1.4 Tissue Mechanics in the Brain in Development and Disease

Cells react to mechanical signals in the TME, engaging in a multifaceted interaction between the extracellular matrix (ECM), neighbouring cells, and the cytoskeleton of each cell, in a process termed mechanosensation (Sarker et al. [2020]). The ECM constitutes an intricate structure composed of diverse macromolecules, systematically organised in a tissue-specific manner, and is present within both normal and pathological tissue environments.

Components of the Brain ECM

The brain ECM is characterised by a distinctive composition comprising fibronectin, laminins, and tenascins among glycoproteins, as well as glycosaminoglycans, including

hyaluronic acid (HA) and proteoglycans such as chondroitin sulphate proteoglycan (Figure 1.2) (Lau et al. [2013]). In contrast to other body tissues, collagen is less prevalent within the brain ECM, located primarily in the basement membranes of blood vessels and the glia limitans. In adult brains, the ECM is predominantly made up of a hyaluronan-lectican-tenascin-R matrix (Yamaguchi [2000]). Proteins within the ECM engage in interactions both with one another and with adjacent cells through specific matrix receptors, facilitating the ECM's role in modulating various cellular signalling pathways. This modulation affects cell fate, migration, maturation, differentiation, and survival, while also maintaining tissue homeostasis within the brain (Mohiuddin and Wakimoto [2021]).

Components of the GBM ECM and TME

The ECM components found in the brain are preserved in the ECM of GBM (Figure 1.2). However, glioma cells exhibit increased expression of specific ECM elements like HA, brevican, tenascin-C, fibronectin, and thrombospondin (Mohiuddin and Wakimoto [2021]). The presence of fibronectin and HA plays a crucial role in promoting glioma cell motility and invasiveness, with higher levels of HA associated with a higher degree of tumour malignancy (David et al. [2004], Pedron et al. [2013]). In addition, the TME of GBM consists of brain-specific cell types, including astrocytes, oligodendrocytes, and neurones, along with immune and endothelial cells. The mesenchymal subtype of GBM, often characterised by *NF1* deletions or mutations, is linked to a greater presence of immune cells associated with tumours, such as macrophages, microglia, CD4 T cells, and neutrophils in TME. Conversely, the TMEs of the proneural and classical subtypes

do not exhibit such an abundance of immune cells. Likewise, PD-L1 expression is more prevalent in mesenchymal tumours compared to classical and proneural subtypes.

Stiffness and Tissue Mechanics

Stiffness can be quantified by Young's modulus (E) which related to a material's resistance to length alteration under axial loads. Cells have a contractile actomyosin cytoskeleton coupled to the external TME through transmembrane proteins such as integrins and cadherins. Through this interaction, the actomyosin cytoskeleton can exert a force on neighbouring cells and the ECM. Similarly, neighbouring cells can exert forces back and the ECM can resist forces and deformation, which contributes to a feed-forward loop which can sustain disease progression (Bonnans et al. [2014], Pillai and Franze [2024], Winkler et al. [2020]). The macro-molecular structure through which the transmembrane protein integrins, transmit their signalling to the intracellular kinase-mediated signalling cascades are termed focal adhesions (FA).

The cytoskeleton constantly remodels itself to adapt to alterations in mechanical TME and is composed of different elements that each carry different types of mechanical forces (Xin et al. [2023]). Actin filament (F-actin) bears tensile forces, microtubules bear compressive forces, while intermediate filaments bear both (Xin et al. [2023]). In cells undergoing migration, actin controls the movement of the leading edge, whereas microtubules manage the withdrawal of the trailing edge (Wehrle-Haller and Imhof [2003]). The polymerisation of actin is crucial for the formation of cell protrusions, and the level of actin polymerisation can be represented by the ratio of F-actin to globular actin (G-actin)

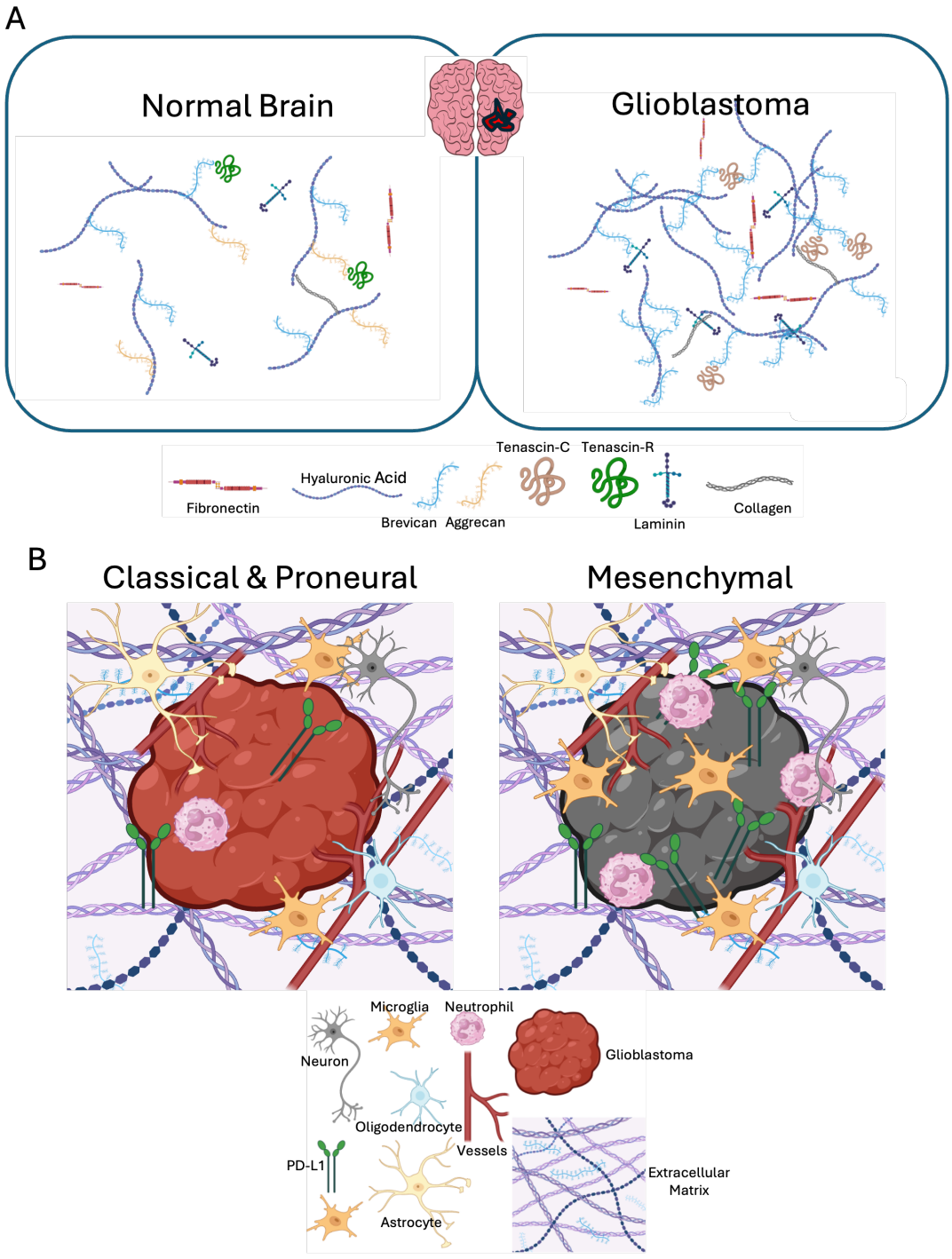

Figure 1.2: **Composition of the ECM in Normal Brain and the Subtype Specific TME in GBM**

A) Compared to the extracellular matrix (ECM) of normal brain, the ECM of GBM demonstrates an overexpression of hyaluronic acid, brevican, tenascin-C, fibronectin which alters the composition, mechanics and physiochemical properties of the tumour micro-environment (TME) **B)** The TME of the mesenchymal GBM subtype is characterised by a higher number of tumour-associated immune cells with increased numbers of microglia and neutrophils compared to non-mesenchymal subtypes. In addition, the TME of mesenchymal GBM is associated with increased expression of the immunosuppressive Programmed death-ligand 1 (PD-L1).

(Dickinson et al. [2004], Fife et al. [2014], Fletcher and Mullins [2010]). Both high and low ratios of F-actin to G-actin correlate with the invasiveness of colon cancer cells with higher F-actin to microtubule ratio correlated with higher malignant grade and cell stiffness (Wehrle-Haller and Imhof [2003], Xin et al. [2023]).

Mechanosensation is essential in many physiological and pathological processes (Pillai and Franze [2024], Rea et al. [2013], Sarker et al. [2020], Umesh et al. [2014]). The mechanical properties of the surrounding tissue are vitally important, with a landmark study by Engler et al. suggesting that matrix elasticity can specify the lineage adopted by naive mesenchymal stem cells independent of the induction culture medium (Engler et al. [2006]). In this study Engler et al. utilised an *in-vitro* model with mechanically tunable PAHG coated with collagen to allow an interface for the stem cells. The stiffness of the PAHG ranged from soft to stiff depending on the degree of chemical cross-linking in the PAHG. They report that on soft substrates, akin to the stiffnesses in brain tissue, the mesenchymal stem cells express neuronal signalling as assessed by microarray analysis. Similarly, on moderate stiffnesses that resemble muscle tissue, the same stem cells adopt myoblast signalling, and on stiff substrates resembling bone, stem cells became a representative of osteoblasts (Engler et al. [2006]).

The stability of cell lines to these lineage was further queried with the addition of specialised culture medium that promoted a different cell lineage (Engler et al. [2006]). When cells were treated after 1 week of growth in mechanically tunable PAHG with culture medium from another lineage, the cell lineage was altered. However, when cells were treated after 3 weeks of growth in mechanically tunable PAHG with culture medium

used to promote another cell lineage, the cell lineage could not be altered, highlighting the importance of providing the appropriate mechanical environment during cell culture when modelling disease (Engelhardt and Ransohoff [2012]).

Tissue stiffness plays an important role in typical brain development, characterised by stiffness gradients evident at different stages of embryogenesis. These gradients are crucial during the migration of neural stem cell populations and neural precursors within the brain's subventricular zones and contribute to cortical folding in the brains of large mammals (Barnes et al. [2017], Bhargav et al. [2022], Franze [2013], Llinares-Benadero and Borrell [2019], Pillai and Franze [2024], Silva et al. [2019]). Human brains gradually stiffen during development and maturation into adulthood (Guo et al. [2019], Pillai and Franze [2024], Thompson et al. [2019]), however, the tissue mechanics of the brain is altered in many disease states and after trauma (Franze [2013], Pillai and Franze [2024]).

There is controversy surrounding the correlation of tumour stiffness and GBM progression (Pillai and Franze [2024]). Some studies show that increased ECM stiffness is associated with higher grades of glioma in *in-vitro* studies and human tumour specimens, with increased ECM stiffness in human tumour samples associated with a worse clinical prognoses (Miroshnikova et al. [2016]). In contrast, other studies demonstrate that gliomas are softer than normal brain tissue with a softer ECM correlated to a higher grade of glioma (Bhargav et al. [2022], Reiss-Zimmermann et al. [2015], Streitberger et al. [2020, 2014]), potentially reflecting the complexity of measuring the TME in GBM. This further underscores the need to standardise measurement techniques for more accurate pre-clinical modelling.

1.5 Mechanosensitive Migration and Invasion of HGG

Crawling cell migration is an evolutionarily ancient feature of eukaryotes, central to processes such as development, immunity, and disease progression in multicellular animals (Friedl and Alexander [2011], Fritz-Laylin et al. [2010]). Migratory behaviours of cells are highly plastic and depend on cell type, environmental conditions, and physical constraints (Liu et al. [2015], Ruprecht et al. [2015]). Individual cancer cells can invade tissues from the tumour mass by degrading the ECM to pass through, squeezing through the pores in the ECM by modifying the cell shape, or using a combination of the two (Brábek et al. [2010], Talkenberger et al. [2017]). Traditionally, migration is classified into amoeboid and mesenchymal migration. Amoeboid migration is characterised by rounded, deformable cell bodies, weak adhesion to the ECM and rapid migration (Friedl and Alexander [2011], Panková et al. [2010]). In contrast, mesenchymal migration is characterised by the degradation of the ECM by proteases, cell polarisation, elongated cell morphology and strong attachment to the surrounding ECM (Friedl and Wolf [2010]). An individual cell's migration style is not constant; cells have been found to switch dynamically between two modes, influenced by the stiffness of the tissue around them (Friedl and Alexander [2011], Taddei et al. [2013], Talkenberger et al. [2017]). Under low adhesion, high confinement conditions, fibroblasts switch from mesenchymal migration to faster amoeboid modes, a transition termed the mesenchymal to amoeboid transition (MAT) (Liu et al. [2015]). Two distinct amoeboid subtypes emerge: the pseudopod mode, characterised by actin-rich pseudopods at the leading edge, and the stable bleb mode, which involves the formation of a stable bleb deficient in actin (Liu et al. [2015], Welch

[2015]). The pseudopod mode is associated with localised actin assembly and moderate contractility, while the stable bleb mode is driven by high global cortical contractility and rearward flow of actomyosin (Liu et al. [2015], Welch [2015]).

The stable bleb is especially prevalent in transformed and tumour cells, as well as in leukocytes, and depends on reduced adhesion signalling and increased myosin II activity. Mathematical models and live imaging support a mechanism in which local contractility fluctuations initiate bleb formation, which is stabilised by polarised cortical flow (Liu et al. [2015], Ruprecht et al. [2015]).

Findings in zebrafish embryonic progenitor cells, show that stable bleb migration can be induced by lysophosphatidic acid (LPA) or physical confinement. Elevated cortical contractility, either pharmacologically induced or arising during wound healing, promotes stable bleb-like migration *in vivo*. Cells expressing constitutively active RhoA recapitulate this behaviour, confirming contractility as a key driver of stable bleb motility (Ruprecht et al. [2015]).

Together, these studies demonstrate that pseudopod and stable bleb modes represent adaptable migration strategies conserved across eukaryotes. The stable bleb mode, in particular, may be critical in embryonic morphogenesis and cancer cell invasion, offering a mechanistic link between cell motility and tissue dynamics in both physiological and pathological contexts (Liu et al. [2015], Ruprecht et al. [2015], Welch [2015]).

GBM cells face challenges due to the limited extracellular space within the brain parenchyma, which is densely packed with ECM proteins, as well as neuronal and glial

cell structures. *In-vivo* measurements by Thorne and Nicholson on the murine neocortex indicate that the undisturbed extracellular space is significantly narrower than a GBM cell, making their migratory capability quite surprising (Cuddapah et al. [2014], Thorne and Nicholson [2006]). Furthermore, unlike other body tissues, the brain ECM has lower levels of rigid structural proteins such as collagen and laminin, and instead the most prevalent component of the ECM of the brain are glycosaminoglycans such as HA (Bellail et al. [2004]). The abundant negative charges on HA draw water into the brain, causing the ECM to swell to ten times the size of the HA matrix itself, resulting in a mechanically soft brain parenchyma (Bellail et al. [2004]). GBM cells produce more HA in TME compared to normal glial cells, and this is associated with the progression of GBM tumours (Pibuel et al. [2021]). In gelatin methacrylate (GelMA) hydrogels containing various ratios of HA methacrylate (HAMA), GBM cells showed greater invasion in softer gels (Chen et al. [2017a], Kondapaneni et al. [2024]). Although these models face constraints due to the use of UV light and photo-initiators leading to cellular harm, as well as the methyl acrylate modifications altering how cells interact with the binding domains of the extracellular matrix, these studies emphasise the significance of TME stiffness in the movement of HGG cells (Lu et al. [2024]).

1.5.1 Mechanosensation

As mentioned, FA are the macromolecular structures through which heterodimeric transmembrane integrins allow for the coupling of the mechanical TME to the intracellular kinase-mediated signalling cascade (Burridge et al. [1988], Buxboim et al. [2010], Rea

et al. [2013], Sarker et al. [2020]). Integrins are composed of α and β subunits that bind to specific ECM ligands (Xin et al. [2023]). In non-small cell lung carcinoma (NSCLC) cells, the absence of integrin $\alpha 11$ correlates with reduced collagen reorganization in TME and diminished tissue stiffness, which subsequently hinders the proliferation (Navab et al. [2016]). In colorectal cancer cells, the $\beta 1$ subunit is associated with increased matrix stiffness, which promotes cancer cell proliferation though an increase in Focal Adhesion Kinase (FAK)-Src phosphorylation (Baker et al. [2013]). Similarly, in GBM cells, the same $\beta 1$ subunit increases tumour cell motility through FAK signalling (Barnes et al. [2018]). In a mammary epithelial cell model, the $\alpha 5\beta 1$ integrin unit is associated with a stiffer ECM and promotes a malignant phenotype through the PI3K-extracellular signal-regulated kinase (ERK) pathway (Miroshnikova et al. [2017]).

EGFR, a type of receptor tyrosine kinase, is overexpressed in nearly half of patients with GBM and correlates with lower overall survival rates (Furnari et al. [2007], Jones and Holland [2011], Shinojima et al. [2003], Verhaak et al. [2010]). Umesh et al. demonstrated increased expression of EGFR with increased substrate stiffness in a 2D cell culture assay (Furnari et al. [2007], Umesh et al. [2014], Verhaak et al. [2010]). This increase in EGFR was also shown to co-localise with FA markers on stiff substrates but not on soft substrates, suggesting that mechanical signals in the TME may be transduced into the intracellular machinery by physical clustering of EGFR (Umesh et al. [2014]). EGFR phosphorylation (p-EGFR) is associated with cell proliferation and invasion, mediated by the downstream phosphorylation of protein kinase B (PKB or Akt) and PI3K (Burgess et al. [2019], Sarker et al. [2020], Umesh et al. [2014]).

FAK is a non-receptor tyrosine kinase that has been shown to bind to EGFR through the FAK FERM domain and to FA through the FAK FAT during integrin activation. FAK, a component of FA, are found at areas of traction force on stiff substrates rather than soft ones in 2D cell cultures utilising deformable micropillar arrays (Zhou et al. [2021]).

In-vivo, cancer cells do not exist in isolation, but rather interact with other cells through cell adhesion molecules (CAM) that mediate cell-cell interactions and cell-ECM adhesion (Xin et al. [2023]). Cadherins are transmembrane proteins that regulate cell-cell interactions. Increased E-cadherin production corresponds with decreased invasiveness across three distinct human breast cancer cell lines (MCF-7, T47D, and MDA-MB-231), as well as an increase in cell-cell adhesive forces, assessed using atomic force microscopy (AFM)-based single-cell force spectroscopy (SCFS). (Omidvar et al. [2014]). This observation contradicts the finding that the majority of breast cancers are invasive ductal carcinomas, which express E-cadherin in both primary tumours and metastases (Li et al. [2003]). In both mouse and human luminal and ductal basal invasive carcinoma models, the absence of E-cadherin was found to increase invasion. However, it also led to decreased cancer cell proliferation and survival, in addition to a reduction in circulating tumour cells, cancer cell seeding in distant organs, and metastatic growth. This indicates that in invasive ductal carcinomas, E-cadherin acts as a survival factor during detachment, systemic spread, and metastasis by inhibiting reactive oxygen species-induced apoptosis (Padmanaban et al. [2019]). In monolayers of normal breast epithelial cells (MCF10A) grown on collagen-coated PAHG, P-cadherin influences the strength of intercellular adhesion forces, whereas E-cadherin controls the speed at which these forces

are established (Bazellières et al. [2015]). The intercellular tension forces were measured using monolayer stress microscopy (MSM), which calculates the state of mechanical stress (force per unit of cross-sectional area) within the cell sheet and is based on the principle that the traction forces applied at the cell-gel interface must be balanced by intracellular and intercellular forces (Bazellières et al. [2015]). Sullivan et al. employed a co-immunoprecipitation model with HEK293T cells, known for their lack of endogenous E-cadherin and minimal EGFR expression, to illustrate the E-cadherin-driven activation of EGFR signalling. The HEK293T cells were transfected with plasmids to express both EGFR and E-cadherin to first show that E-cadherin and EGFR form a heteroreceptor complex at the membrane. Further, the interactions between E-cadherin and EGFR at the plasma membrane are interrupted by tensile forces on homophilic E-cadherin, even in the absence of EGF. This disruption permits EGFR monomers to dimerize, bind to EGF, and initiate downstream signalling (Sullivan et al. [2022]). Finally, interruption of the integrin-FAK-Src signalling pathway inhibits collective cell migration in human squamous carcinoma cells, underscoring the interdependence between cell-cell and cell-ECM adhesions (Canel et al. [2010], Xin et al. [2023]).

The adhesion between cells, as well as the attachment of cells to ECM, are crucial and evolve dynamically throughout tumour progression. In the early phases of invasion, a decrease in cell-cell adhesion is necessary to permit the detachment of cells from the tumour mass into adjacent tissues. (Cavallaro and Christofori [2001], Paschos et al. [2009]). Despite this, invasive breast cancer cells demonstrate higher cell-cell adhesion

compared to normal cells (Cavallaro and Christofori [2001], Paschos et al. [2009], Pawlizak et al. [2015], Xin et al. [2023]). The cause of this may be related to two modes of migration described in the literature. In single cell migration, there is a reduction in cell-cell adhesions whilst in collective migration, cell-cell interactions are required for cells to migrate and invade as sheets, ropes and clusters. (Janiszewska et al. [2020], Wolf et al. [2007], Xin et al. [2023]).

GBM is capable of infiltrating three-dimensional astrocyte matrices, mouse brain xenografts, and human tumour samples both individually and in groups (Gritsenko et al. [2017]). Specifically, GBM cells maintain intercellular contacts as they invade along blood vessels and astrocyte-rich brain stroma, indicating that collective migration plays a crucial role in the infiltration of brain tissue by HGG cells (Cuddapah et al. [2014], Farin et al. [2006], Gritsenko et al. [2017], Volovetz et al. [2020], Winkler et al. [2009]). Similarly, in collagen-embedded spheroids HGG cells have a clear proclivity to move collectively (Grundy et al. [2016]) and in patient-derived HGG xenografts in the mouse brain, HGG cells create multicellular networks that connect individual cells, facilitating GBM invasion (Osswald et al. [2015]).

1.6 Measurement of Tissue Stiffness

Research involving xenograft models, cancer cell lines, and clinical specimens indicates that cells from cancers such as bladder, breast, ovarian, lung, pancreas, prostate, and thyroid exhibit reduced stiffness relative to normal cells, while liver, lymphoid, and myeloid

cancer cell lines demonstrate increased stiffness compared to their normal counterparts (Cross et al. [2007], Lekka et al. [2012], Xin et al. [2023]). Investigations reveal that for both breast and ovarian cancers, cell stiffness shows an inverse correlation with invasiveness (Han et al. [2020], Nyberg et al. [2017], Swaminathan et al. [2011], Xin et al. [2023]). In contrast, invasive prostate cancer cells tend to be stiffer than those with a less invasive phenotype (Faria et al. [2008], Swaminathan et al. [2011]). These instances underscore the possibility that the relationship between cell stiffness and malignancy is cancer-type dependent (Xin et al. [2023]). Furthermore, as the poor progression of preclinical studies to clinical trials has been partly attributed to altered HGG signalling in the mechanically soft brain, to better develop successful therapies *in-vivo*, the mechanical properties of the brain must first be defined (Mai et al. [2024], Sarker et al. [2020], Seker-Polat et al. [2022]).

1.6.1 Young's Modulus

As highlighted, the literature value for E in the brain varies from 0.1 to 1 kPa (Budday et al. [2015], Butcher et al. [2009], Christ et al. [2010], Elkin et al. [2007], Taylor and Miller [2004]). Variability in these measurements may be due to differences in protocols, brain donor species, age of the brain donor and the heterogeneity of the brain parenchyma (Hrapko et al. [2008]), with white matter 39% stiffer than grey matter when measured by indentation in fresh bovine brains (Budday et al. [2015]). The idea that biomechanical stiffness impacts cellular function is critically significant. In 2009, Ulrich et al. showed that with increased ECM stiffness, glioma cells migrate more rapidly and are able to form

FA and stress fibres more quickly when compared to lower stiffness substrates (Manini et al. [2018], Ulrich et al. [2009]).

Malignant brain tumours were traditionally believed to exhibit greater firmness compared to normal brain tissue (Northcott et al. [2018], Northey et al. [2017]). Studies using atomic force microscopy (AFM) in fresh frozen human brain samples revealed that gliomas become stiffer with increasing grade, marked by a notable increase in hyaluronic acid (HA) and tenascin C levels, which increased with grade of glioma (Miroshnikova et al. [2016]). Crucially, ECM stiffness did not show correlation with the levels or distribution of type I collagen, blood vessels, or cell density. In line with epidemiological data (Ohgaki and Kleihues [2005]), the *IDH1* mutational status, via ectopic expression of the R132H *IDH1* mutation, significantly extended the survival of nude mice implanted with xenografts from either primary GBM cells or the U87 cell line. In particular, the protective effect of the *IDH1* mutation waned as the stiffness of the substrate increased. Recent research indicates that GBM could potentially be mechanically softer than healthy brain tissue (Jamin et al. [2015], Janas et al. [2024], Pillai and Franze [2024], Streitberger et al. [2014]). This may be due in part to improvements in the sensitivity of mechanical testing and advancements in force sensor technology used in recent studies (Budday et al. [2020]).

1.6.2 Brain Tissue is Viscoelastic

It is important to note that there is no single value that characterises the mechanical properties of the brain parenchyma, as the tissue is viscoelastic; having elastic and viscous

properties (Franze et al. [2013], Manduca et al. [2021], Pillai and Franze [2024]). Elasticity refers to the storage of applied energy as mechanical deformation which is returned when the object resumes its shape and is characterised by a storage (elastic) modulus (G'). Viscosity refers to the dissipation of applied energy through mechanical deformation and is characterised by a loss modulus (G'') (Manduca et al. [2021]). $\mid G^* \mid$ refers to the absolute value of the complex shear modulus and is related to both G' (elastic component) and G'' (viscous component) (Manduca et al. [2021], Schregel et al. [2020]):

$$|G^*| = G' + G'' \tag{1.1}$$

The term "shear stiffness" is reported in the literature and inconsistently refers to either the complex shear modulus or to density x wave speed^2 (Manduca et al. [2021]).

Viscoelastic materials are characterised by a deformation that is time dependent; meaning the longer the application of an applied force, the greater the deformation of the object. As such, these materials are softer when the forces are measured on a slower time scale compared to forces that are applied more rapidly. This is in part due because on slower time scales, the forces applied to the material have more time to dissipate through viscous flow (Franze et al. [2013], Manduca et al. [2021], Pillai and Franze [2024]). Consequently, in viscoelastic materials, the use of higher transducer frequency in methods like magnetic resonance elastography (MRE)—a non-invasive technique that combines standard magnetic resonance imaging with an externally induced shear wave in the tissue through a transducer—results in increased values for G' and G'', and subsequently $\mid G^* \mid$

(Budday et al. [2020], Manduca et al. [2021], Mariappan et al. [2010], Muthupillai et al. [1995], Pillai and Franze [2024]). MRE can be performed at multiple frequencies to probe this behaviour and rheological models are commonly used to report a single stiffness value (Manduca et al. [2021]). Common models used include Voigt, Maxwell, Zener, and spring-pot models, which each vary according to the assumptions used (these models are not discussed in this thesis. Please refer to Manduca et al. [2021] for more information).

1.6.3 Magnetic Resonance Elastography as A Non-Invasive Approach to Measure Stiffness

MRE offers a distinct advantage over other methods by facilitating the assessment of *in-vivo* tissues, taking into account the supplementary mechanical constraints imposed on brain tissues by the skull, meninges, and cerebrospinal fluid (Pillai and Franze [2024]). In addition, preparation of *ex vivo* tissue samples for alternative measurements methods, such as freezing, drying, or fixation, can substantially alter the mechanical characteristics of the samples themselves (Pillai and Franze [2024]). Similarly, tissue mechanical properties change rapidly within hours after death, underscoring the benefits of evaluating *in-vivo* samples (Gautier et al. [2015], Pillai and Franze [2024]). Furthermore, conventional rheometric techniques exhibit spatial resolutions in the centimetre range, while MRE offers resolutions in the millimetre range (Pillai and Franze [2024]). AFM-based indentation techniques have effectively mapped tissue stiffness at the cellular scale, yet these measurements are confined to the tissue surface and cannot reach deeper levels (Christ et al. [2010], Koser et al. [2016], Pillai and Franze [2024], Thompson et al. [2019]).

Research has also explored the stiffness of brain tissue as an indicator of therapy response (Feng et al. [2016], Schregel et al. [2020]). Currently, the success of brain tumour treatments is typically evaluated by observing alterations in tumour size (James et al. [1999], Macdonald et al. [1990]). However, changes in size do not always represent shifts in the tumour's internal characteristics (Feng et al. [2016], Schregel et al. [2020]). In a mouse GBM model, anti-VEGF therapy led to enlargement and increased tumour stiffness (Schregel et al. [2020]). This increase in stiffness was associated with prolonged survival in tumours treated with therapy compared to untreated controls (Schregel et al. [2020]). As such, to best develop successful HGG therapies *in-vitro*, models must be explored that not only replicate the mechanical TME of GBM and in healthy brain, but also model and respond to changes in TME during disease and therapies.

1.7 Primary Patient Derived Cells

Commercially available cells lines are commonly used in research as they are less expensive compared to patient-derived samples, can be propagated in culture virtually indefinitely, and do not pose ethical concerns (Lenting et al. [2017], Paolillo et al. [2021]). These continuously cultured cell lines are established from patient tissue, but are immortalised by genetic mutation or modification (Lenting et al. [2017]). The most commonly used HGG cell lines, U87-MG and U251-MG, were generated in the 1960s and have since been used in more than 1000 published studies (Lenting et al. [2017]). However, the use of these cell lines requires careful consideration as it has been widely recognised that the cell culture conditions themselves act as a selection pressure in GBM (Pollard et al. [2009]).

Repeated subculture of cell lines can introduce both genotypic and phenotypic changes over time, further complicating the intricate landscape of glioma genotypes (Paolillo et al. [2021]). The widespread use of U87-MG cell lines around the world has led to a large number of subclones of U87-MG which may further affect experimental reproducibility (Lenting et al. [2017]). Genetic profiling and transcriptome analysis of both the U87-MG cell line and the originating tumour have revealed discrepancies, leading to the suggestion that the U87-MG cell line is probably a glioblastoma cell line of human origin, but its precise origin remains uncertain (Allen et al. [2016]).

Historically, HGG cells have been grown using Dulbecco's Modified Eagle Medium (DMEM) enriched with 10% fetal bovine serum (FBS). In 2003, the discovery of cancer stem cells (CSCs) in GBM raised issues regarding serum-supplemented media and the potential induction of stem cell differentiation (Ledur et al. [2017], Quiñones-Hinojosa et al. [2007], Singh et al. [2003]). Culturing patient-derived HGG cells in a serum-free Neurobasal medium supplemented with EGF and FGF-2 resulted in cells that more closely resembled the original tumour, as opposed to cells grown in DMEM medium with serum. (Lee et al. [2006]). Despite this, only 45% of the primary cell lines created from the tumour mass cell maintained their original molecular subtype (Xie et al. [2015]), highlighting the ongoing need for research in this area to preserve the *in-vivo* characteristics of GBM.

1.8 Modelling the Mechanical Properties of the Brain

Various models have been used to advance understanding and representation of GBM TME, with the aim of investigating the influence of the mechanical environment on the mechanisms of GBM invasion (Gritsenko et al. [2017], Pillai and Franze [2024], Rao et al. [2014], Xin et al. [2023]). Single cell 2D cell culture assays have been widely used due to their ease of use and low cost. They are based on the coating of tissue culture plates with ECM molecules, including laminin, fibronectin, or collagen to allow cell adherence (Chen and Nalbantoglu [2014], Gritsenko et al. [2017], Nakada et al. [2013]). Although these assays have significantly advanced our knowledge of cancer cell biology, they do not adequately represent the fundamental aspects of the 3D brain, including cell-cell interactions, the intricate 3D arrangement of infiltrating structures such as blood vessels and white matter tracts, low substrate stiffness, and 3D spatial constraints that facilitate adhesion-dependent and adhesion-independent migration (Cukierman et al. [2001], Haeger et al. [2015], Kondapaneni et al. [2024], Rape et al. [2014], Simian and Bissell [2017], Vollmann-Zwerenz et al. [2020]). In particular, the stiffness of polystyrene tissue culture plates is many orders of magnitude stiffer compared to brain tissues ($\sim$ 3,000,000 kPa vs $\sim$ 1kPa) (Figure 1.1) (Budday et al. [2015], Butcher et al. [2009], Christ et al. [2010], Elkin et al. [2007], Gómez-Oliva et al. [2021], Kondapaneni et al. [2024], Taylor and Miller [2004]).

1.8.1 2D Models of The Brain Mechanobiology

To more accurately simulate brain stiffness, two-dimensional migration assays have employed cell culture plates coated with both natural and synthetic hydrogels with a diversity of molecular constituents, such as fibrillar collagen, reconstituted basement membrane (rBM) abundant in laminin and type IV collagen, as well as composite PAHG (Ananthanarayanan et al. [2011], Gritsenko et al. [2017], Ulrich et al. [2009], Yang et al. [2010]). PAHGs are biologically inert and mechanically tunable by modulating concentrations of acrylamide and bisacrylamide to alter the density of fibre crosslinking (Grundy et al. [2016]). Mechano-sensitive and insensitive phenotypes in GBM have been described (Grundy et al. [2016]). Individual primary patient-derived HGG cells plated on rBM coated mechanically tunable PAHG representing the range of physiological and pathological stiffnesses in the brain demonstrated increased migration speed and distance in response to increased PAHG stiffness for mechano-sensitive cell lines. In contrast, mechano-insensitive cell lines did not demonstrate these behaviours (Grundy et al. [2016]). This has implications for GBM dissemination *in-vivo* as mechano-sensitive HGG phenotypes may demonstrate a preference for more stiff regions such as myelinated fibres and blood vessels (Gritsenko et al. [2017], Grundy et al. [2016]).

1.8.2 Increased Dimensionality with 3D Models

Whilst 2D assays allow a ready comparison with the widely published literature by restricting migration and invasion in a single plane, the limited dimensionality can have implications on cell behaviour. 3D scaffolds have been used in the literature and are

generally based on the seeding of cells in a pre-fabricated scaffold used to mimic tissue properties such as porosity and structure (Kondapaneni et al. [2024], Paolillo et al. [2021]). Culture conditions can impact morphology and protein expression of cells. U118 glioma cells morphologically formed spheres, increased expression of stem markers and demonstrated increased invasive capacity in 3D scaffolds compared to traditional 2D culture (Florczyk et al. [2013]). Similarly, HGG cells in a 3D collagen scaffold demonstrated increased resistance to commonly used alkylating agents in GBM, greater stemness, and upregulation of *MGMT*, mimicking resistance patterns seen in glioma patients, compared to cells cultured in 2D (Lv et al. [2020]). While cells embedded in hydrogels experience ECM signals from all angles, similar to their normal states, major drawbacks of this model include the requirement of synthetic materials to be coated in ECM proteins to allow cell adhesion and the inability of models to provide a dynamic TME replicating the continuous remodelling and healing processes *in-vivo* (Ahmed [2023], Kondapaneni et al. [2024], Paolillo et al. [2021]). Natural collagen scaffolds have been shown to be invaded by gliomas cells (Gritsenko et al. [2017], Grundy et al. [2016], Yang et al. [2010]), however, in the unperturbed brain, collagens are expressed primarily along blood vessels and not the general brain parenchyma (Bellail et al. [2004], Gritsenko et al. [2012]) and hence the relevance of these findings to elucidate the migration patterns of GBM *in-vivo* remain unclear (Gritsenko et al. [2017], Rape et al. [2014]).

1.8.3 Spheroids as a Model of GBM

The need to study the behaviour of HGG cells within models of higher dimensionality to more accurately mimic *in-vivo* environments has driven the development of spheroid models. As the name suggests, these models involve the aggregation of tumour cells in a mass and can be plated onto a substrate or embedded in a scaffold. Spheroids have the advantage that they replicate gradients in oxygen, nutrients, growth factors, and signalling, as well as simulate cell interactions with each other and tumour architecture (Ahmed [2023], Costa et al. [2016], Mark et al. [2020], Nath and Devi [2016], Nunes et al. [2019], Ryan et al. [2001]). There are various protocols to generate spheroid including hanging drop, ultra-low attachment plates, spinner plates, and 3D printing (Costa et al. [2016], Nath and Devi [2016]). The restricted movement of oxygen and nutrients into the mass of the spheroid, along with the accumulation of metabolic waste, results in the creation of three separate concentric zones: a necrotic hypoxic core, a middle zone of inactive cells, and an outer region of actively dividing cells (Han et al. [2021], Nath and Devi [2016]). When these spheroids are plated or embedded in an adhesive substrate, the introduction of cell-substrate interactions coupled with biochemical pressures induced HGG cells to invade the substrate away from the spheroid bulk (Berrier and Yamada [2007], Friedl et al. [2012], Friedl and Wolf [2003]. The spheroid model also offers the benefit of exploring the roles played by cells migrating individually and in groups when exiting the spheroid. In many cases, a "leader cell" guides collective migration by adopting a mesenchymal phenotype that enzymatically modifies the ECM, forming routes for the other cells to traverse (Khalil and Friedl [2010], Mayor and Etienne-Manneville

[2016]). It is unclear why certain cells stay within the spheroid, some persist in migrating collectively, and others opt for solitary migration. Potentially, the differences may represent heterogeneity within spheroids (Patel et al. [2014]). In a breast cancer spheroid model, cancer cells at the invasive front are softer and larger compared to those cells in the core when measured using confocal microscopy and optical tweezers (Han et al. [2020]). Additionally, using nanoscale atomic force microscopy of breast tissues, the stromal stiffness of the tumour edge is four times stiffer compared to the centre (Paszek et al. [2005]). The potential differences between these populations could be significant with implications for therapeutic interventions (Garcia-Diaz et al. [2023]).

1.8.4 Gold Standard: Xenografts

Patient-derived xenograft models offer an enormous advantage over *in-vitro* models in modelling the complex TME, however are limited by high costs, limited availability and inability to control elements of the TME which limits use in high through-put analysis (Kondapaneni et al. [2024], Simeonova and Huillard [2014]). Utilising intravital microscopy alongside particle tracking micro-rheology to assess tumour stiffness *in-vivo*, it was demonstrated that the stiffness of cancer cells in xenografts exceeds that of both 2D cultured cells and tumour spheroids within 3D matrices (Wang et al. [2022]).

The additional dimensionality and introduction of *in-vivo*-like conditions in xenografts may generate differences in the TME at the central core and the invading edge (Garcia-Diaz et al. [2023]). The core is marked by a hypoxic centre, whereas the invasive margin features relatively normal tissue (Garcia-Diaz et al. [2023], Patel et al. [2014], Sottoriva

et al. [2013], Verhaak et al. [2010]). Recent advances in single-cell RNA sequencing have enabled the exploration of intratumoral heterogeneity with these two areas displaying different molecular characteristics. Within the tumour mass, HGG cells are enriched with markers indicative of an injury-like state, whereas in the invasive margin, HGG cells show markers that are development-like. (Brooks and Parrinello [2017], Garcia-Diaz et al. [2023], Glas et al. [2010], Stringer et al. [2019], Venkataramani et al. [2022]). Although single-cell RNA sequencing has progressed significantly, it lacks the necessary spatial context to correlate transcriptional changes with the tumour's physical architecture. Spatial transcriptomics complements single-cell RNA sequencing by providing gene expression information alongside the 2D spatial arrangement of cells. This combination offers a holistic picture of transcriptional diversity within the tumour microenvironment, with research in oral squamous cell carcinomas revealing distinct transcriptional profiles, neighbouring cell compositions, and ligand-receptor interactions between the leading edge and core (Arora et al. [2023]). Nevertheless, existing insights into the biology of GBM largely originate from studying samples of the main tumour mass, as opposed to examining the invasive peripheral cells that play a role in tumour recurrence following surgical procedures. (Gupta et al. [2024]).

In summary, a single model is insufficient to thoroughly and accurately represent the intricate TME in GBM. To enhance our understanding of both healthy and diseased brain conditions, it is essential to employ a combination of modelling approaches.

1.9 Study Aims and Overview

Gliomas are the most prevalent malignant primary brain tumours, with high-grade gliomas, such as GBM, being especially resistant to conventional treatments of maximal surgical resection and chemo-radiation. The outlook for patients with GBM remains bleak despite the available therapies, highlighting the importance of understanding why treatments fail. The interaction between the tumour and its surrounding microenvironment is increasingly acknowledged as a crucial factor in the development of cellular adaptation, tumour heterogeneity, and resistance to treatment. In particular, the study of the mechanical environment and role of mechano-sensation is gaining traction in explaining the poor progression of therapies trialled as successful *in-vitro* into clinical practice.

To this end, this thesis aimed to further characterise HGG migration and invasion as a result of the mechanical environment of the brain *in-vivo* to better generate models to test therapies *in-vitro*. Chapter 3 explores the migration patterns of four patient-derived cell lines. A spheroid model was used to examine how alterations in cell-cell and cell-substrate adhesions are influenced by the varying substrate stiffness. The identified behaviours were then correlated to differentially expressed genes identified from publicly available RNA sequencing data. Chapter 4 builds upon this to elucidate the spatial arrangement of key components in the mechanosensation signalling pathway, EGFR and FAK, to more stiff structures such as blood vessels using human xenografts in a whole brain slice mouse model with the same four primary patient-derived GBM cell lines. Finally, chapter 5 aims to clarify the reported changes in tumour mass stiffness and surrounding brain parenchyma induced by radiation therapy, chemotherapy, and surgical intervention using

a systematic review of the literature.

Overall, this body of work defines the stiffness of the normal and diseased brain and then the impact of the mechanical environment on the routes of dissemination of GBM cells. The insights gained in this thesis will inform the design of improved preclinical models for HGG that incorporate key elements of the *in-vivo* tissue environment and thus allow improved preclinical assessment of novel therapies.

Chapter 2

Materials And Methods

2.1 Materials

2.1.1 Chemicals, reagents and commercially purchased kits

All chemicals and reagents used were of analytical grade or higher.

Table 2.1: Chemicals, drugs & commercially purchased kits. List of all commercially purchased reagents used in this thesis.

Item	**Catalogue Number**	**Supplier**
1X Opal Anti-Ms + Rb HRP	#ARH1001EA	Akoya Biosciences (Massachusetts, USA)
1X OPAL Antibody Diluent / Block	#ARD1001EA	Akoya Biosciences (Massachusetts, USA)
3,3-diaminobenzidine (DAB) detection ((BOND Polymer Refine Detection)	#DS9800	Leica Biosystems (Nussloch, Germany)
4,6-diamidino-2-phenyindole (DAPI)	#D9564	Sigma-Aldrich (Hesse, Germany)
Accutase	#A6964	Sigma-Aldrich (Hesse, Germany)
Acrylamide/Bis solution	#161-0156	Bio-Rad (California, USA)

Continued on next page

Table 2.1: Chemicals, drugs & commercially purchased kits. List of all commercially purchased reagents used in this thesis. (Continued)

Agarose	#0710	Amresco (Pennsylvania, USA)
Ammonium persulfate (APS)	#A3678	Sigma-Aldrich (Hesse, Germany)
Antibiotic-antimycotic 100x	#15240062	Life Technologies (subsidiary of Thermo Fisher Scientific, Massachusetts, USA)
Aprotinin from bovine lung	#A1153	Life Technologies (subsidiary of Thermo Fisher Scientific, Massachusetts, USA)
B27™ without vitamin A supplement 50x	#12587	Life Technologies (subsidiary of Thermo Fisher Scientific, Massachusetts, USA)
CellAdhere dilution buffer	#07183	StemCell Technologies (British Columbia, Canada)
Citrate pH 6.0 antigen retrieving buffer	#K8005	DAKO (Glostrup, Denmark)
Citrate-based pH 6.0 epitope retrieval solution	#AR9961	Leica Biosystems (Nussloch, Germany)
CO2-independent medium	#18045088	Life Technologies (subsidiary of Thermo Fisher Scientific, Massachusetts, USA)
Collagen 1 (from rat tail)	#354236	Corning (New York, USA)
Dimethyl sulfoxide (DMSO)	#D2650	Sigma-Aldrich (Hesse, Germany)
Donkey Serum	#D9663	Sigma-Aldrich (Hesse, Germany)
Dulbecco's modified eagle medium (DMEM) high glucose, pyruvate	#11995065	Life Technologies (subsidiary of Thermo Fisher Scientific, Massachusetts, USA)
Dulbecco's modified eagle medium (DMEM) nutrient mixture F-12	#11320033	Life Technologies (subsidiary of Thermo Fisher Scientific, Massachusetts, USA)
Dulbecco's phosphate buffered solution (DPBS) without calcium magnesium	#14190250	Life Technologies (subsidiary of Thermo Fisher Scientific, Massachusetts, USA)
EDTA pH 9.0 antigen retrieving buffer	#K8004	DAKO (Glostrup, Denmark)
EDTA-based pH 9.0 epitope retrieval solution	#AR9640	Leica Biosystems (Nussloch, Germany)
Epidermal Growth Factor (EGF)-human recombinant	#100-26	Shenandoah Biotechnologies (Pennsylvania, USA)

Continued on next page

Table 2.1: Chemicals, drugs & commercially purchased kits. List of all commercially purchased reagents used in this thesis. (Continued)

Ethylenediamine tetraacetic acid (ETDA) 0.5M pH 8 RNase-free	#AM9260G	Invitrogen (subsidiary of Thermo Fisher Scientific, Massachusetts, USA)
Fetal bovine serum (FBS)	#10099-141	Life Technologies (subsidiary of Thermo Fisher Scientific, Massachusetts, USA)
Fibroblast growth factor basic 154aa (FGF2)-human recombinant	#100-146	Shenandoah Biotechnologies (Pennsylvania, USA)
FluorSave™ reagent	#345789	Sigma-Aldrich (Hesse, Germany)
Glycerol	#0854	Amresco (Pennsylvania, USA)
Glycine	#0167	VWR International (Pennsylvania, USA)
Harris Hematoxylin	#3801560	Leica Biosystems (Nussloch, Germany)
Heparin solution (2mg/mL)	#07980	StemCell Technologies (British Columbia, Canada)
Matrigel™ growth factor reduced basement membrane matrix, lactate dehydrogenase elevating virus (LDEV)-free	#354428	Corning (New York, USA)
Minimal essential media (MEM) non-essential amino acids solution 100x	#11140050	Life Technologies (subsidiary of Thermo-Fisher Scientific, Massachusetts, USA)
N-2 supplement 100x solution	#17502001	Life Technologies (subsidiary of Thermo Fisher Scientific, Massachusetts, USA)
Nuclease-free water	#1039498	QIAGEN (Hilden, Germany)
Opal 7-Color Automation IHC Kit	#NEL821001	Akoya Biosciences (Massachusetts, USA)
Opal Polaris 480 reagent pack	#FP1500001	Akoya Biosciences (Massachusetts, USA)
Opal Polaris 780 reagent pack	#FP1501001	Akoya Biosciences (Massachusetts, USA)
PAP pen	#Z377821	Sigma-Aldrich (Hesse, Germany)
Paraformaldehyde	#158127	Sigma-Aldrich (Hesse, Germany)
Penicillin-streptomycin	#15070063	Life Technologies (subsidiary of Thermo Fisher Scientific, Massachusetts, USA)
Prolong Gold antifade reagent with DAPI (Mounting media)	#P36935	Thermo Fisher Scientific, Massachusetts, USA)

Continued on next page

Table 2.1: Chemicals, drugs & commercially purchased kits. List of all commercially purchased reagents used in this thesis. (Continued)

Phalloidin AlexaFluor® 488	#A12379	Life Technologies (subsidiary of Thermo Fisher Scientific, Massachusetts, USA)
Phalloidin AlexaFluor® 568	#A12380	Life Technologies (subsidiary of Thermo Fisher Scientific, Massachusetts, USA)
Platelet derived growth factor (PDGF)-AA	#100-16	Shenandoah Biotechnologies (Pennsylvania, USA)
Platelet derived growth factor (PDGF)-BB	#100-18	Shenandoah Biotechnologies (Pennsylvania, USA)
Potassium chloride	#P9451	Sigma-Aldrich (Hesse, Germany)
Potassium phosphate monobasic	#P5655	Sigma-Aldrich (Hesse, Germany)
Sodium chloride	#BIOSB0476	Astral Scientific (New South Wales, Australia)
Sodium citrate	#BIOCB0035	Astral Scientific (New South Wales, Australia)
Sodium phosphate dibasic	#S29763	Sigma-Aldrich (Hesse, Germany)
StemPro™ Neural Supplement	#A1050801	Life Technologies (subsidiary of Thermo Fisher Scientific, Massachusetts, USA)
Sucrose	#S7903	Sigma-Aldrich (Hesse, Germany)
Sudan Black	#199664	Sigma-Aldrich (Hesse, Germany)
Tris	#BIO3094T	Amresco (Pennsylvania, USA)
Tris-Buffered-Saline (TBS)	#K8007	DAKO (Glostrup, Denmark)
TritonX-100	#T8787	Sigma-Aldrich (Hesse, Germany)
Trypsin-EDTA 0.5% (v/v) with phenol red	#25300054	Sigma-Aldrich (Hesse, Germany)
Trypsin inhibitor from glycine max (soybean)	#T9003	Sigma-Aldrich (Hesse, Germany)
Tween-20	#P1379	Sigma-Aldrich (Hesse, Germany)
Urea	#U3578	Sigma-Aldrich (Hesse, Germany)

2.1.2 Solutions

All chemicals and reagents used were analytical grade or higher.

Table 2.2: Composition of Solutions Used in this Thesis

Solution/Buffer	Constituants
1% Matrigel Solution	1% (v/v) Matrigel™ in DMEM media
1.5% agarose solution for spheroid formation	1.5% (w/v) agarose in DMEM media
4% Paraformaldehyde (PFA) solution	4% PFA (v/v) in 1x PBS
16% PFA solution	16% (w/v) PFA in ddH_20, pH adjusted to 7.2 with 0.5M NaOH pellets
20% Sodium dodecyl sulfate (SDS) solution	20% SDS (w/v) in ddH_20
300mM Tris- hydrochloride (HCl)	300mM Tris in ddH_20, pH adjusted to 6.8 with HCl
0.1M Tris-HCl	0.1M Tris in ddH_20, pH adjusted to 6.8 with HCl
0.25M Tris-HCl	0.25M Tris in ddH_20, pH adjusted to 6.8 with HCl
1M Sodium hydroxide (NaOH) solution	1M NaOH in ddH_20
1M Tris-HCl	1M Tris in ddH_20, pH adjusted to 6.8 with HCl
1.5M Glycine solution	1.5M glycine in 1xPBS
1x PBS with TritonX-100 (PBS-T)	0.2% (v/v) TritonX-100, 1x PBS
1 x Phosphate-buffered saline (1 x PBS)	10%(v/v) 10x phospahte-buffered saline in autoclaved, distilled water
1x TBS with Tween-20 (TBS-T)	% (v/v) Tween-20, 1x TBS
10x Tris-buffered saline (TBS)	0.1M Tris-HCl, 0.15M NaCl in ddH_20, pH adjusted to 7.5

Continued on next page

Table 2.2: Composition of Solutions Used in this Thesis (Continued)

10 x Phosphate-buffered saline (10 x PBS)	1.4 M sodium chloride (NaCl) , 0.03 M potassium chloride (KCL), 0.1 M sodium phosphate dibasic (Na2HPO4), 0.02 M potassium phosphate monobasic (KH_2PO_4) in autoclaved, distilled water with pH adjusted to 7.4
Blocking buffer	10% (v/v) normal serum in 1x PBS
Sodium citrate buffer with 0.05% Tween-20	0.01 M sodium citrate, 0.05% (v/v) Tween-20 in autoclaved, distilled water with pH adjusted to 6.0
Sudan Black Solution	0.1% (w/v) Sudan black in 70% ethanol
Trypsin inhibitor solution	1mg/mL trypsin inhibitor from glycine max in ddH20
Wash buffer	0.5% (w/v) BSA in 1x PBS

2.1.3 Antibodies

The antibodies used in this thesis are listed below and are segregated by application.

Table 2.3: Primary Antibodies Used in 3,3-Diaminobenzidine (DAB) Staining

Tissue	Antibody (clone)	Catalogue Number	Dilution	Antigen Retrival Buffer
Human GBM (Xenograft)	HLA (EMR8-5)	#ab70328	1:200	Citrate pH 6.0
Human Placenta	EGFR (E235)	# ab32077	1:200	Citrate pH 6.0
	p-EGFR (EP774, phospho Y1068)	# ab40815	1:500	EDTA pH 9.0
	FAK	#3285	1:100	EDTA pH 9.0
	p-FAK (TYr397)	#44-625G	1:200	EDTA pH 9.0
	HLA (EMR8-5)	#ab70328	1:500	EDTA pH 9.0
Human Spleen	HLA (EMR8-5)	#ab70328	1:500	Citrate pH 6.0
	FAK	#3285	1:500	EDTA pH 9.0
	p-FAK (TYr397)	#44-625G	1:500	Citrate pH 6.0
Mouse Brain	HLA (EMR8-5)	#ab70328	1:500	EDTA pH 9.0
	EGFR (E235)	# ab32077	1:200	Citrate pH 6.0
	p-EGFR (EP774, phospho Y1068)	# ab40815	1:500	EDTA pH 9.0
	FAK	#3285	1:100	EDTA pH 9.0

Continued on next page

Table 2.3: Primary Antibodies Used in 3,3-Diaminobenzidine (DAB) Staining (Continued)

	p-FAK (TYr397)	#44-625G	1:200	EDTA pH 9.0

Table 2.4: Primary Antibodies Used In Monoplex IF. The antigen retrieval buffer used, incubation time and the OPAL secondary pair used is also listed

Tissue	**Antibody (clone)**	**Catalogue Number**	**Dilution**	**Antigen Retrival Buffer**	**OPAL Pair (nm)**	**Incubation time (min)**
Human GBM (Xenograft)	HLA (EMR8-5)	#ab70328	1:200	Citrate pH 6.0	480	60
	GLUT1 (SPM498)	#NBP1-35926	1:200	Citrate pH 6.0	520	60
	EGFR (E235)	#ab32077	1:200	Citrate pH 6.0	780	60
	p-EGFR (EP774, phospho Y1068)	#ab40815	1:500	EDTA pH 9.0	570	60
	FAK	#3285	1:50	EDTA pH 9.0	620	60
	p-FAK (TYr397)	#44-625G	1:50	Citrate pH 6.0	690	60
Human Placenta	EGFR (E235)	#ab32077	1:200	Citrate pH 6.0	780	60
	p-EGFR (EP774, phospho Y1068)	#ab40815	1:500	EDTA pH 9.0	570	60
	FAK	#3285	1:50	EDTA pH 9.0	620	60
	p-FAK (TYr397)	#44-625G	1:50	Citrate pH 6.0	690	60
	HLA (EMR8-5)	#ab70328	1:500	Citrate pH 6.0	780	60
Human Spleen	p-EGFR (EP774, phospho Y1068)	#ab40815	1:500	EDTA pH 9.0	570	60

Table 2.5: Primary Antibodies Used In Multiplex IF. The order of the antibodies used, antigen retrieval buffer used, incubation time and the OPAL secondary pair used is also listed

Multiplex-Staining Order	**Antibody (clone)**	**Catalogue Number**	**Dilution**	**Antigen-Retrieval Buffer**	**OPAL Pair(nm)**	**Incubation time (min)**	**Manufacturer**
1	GLUT1 (SPM498)	#NBP1-35926	1:200	Citrate pH 6.0	520	60	Novus Biologicals (Colorado, USA)
2	p-EGFR (EP774, phospho Y1068)	# ab40815	1:500	EDTA pH 9.0	570	60	Abcam (Cambridge, UK)
3	p-FAK (TYr397)	#44-625G	1:50	Citrate pH 6.0	690	60	Invitrogen (subsidiary of Thermo Fisher Scientific, Massachusetts, USA)
4	FAK	#3285	1:50	EDTA pH 9.0	620	60	Cell Signalling Technologies (CST, Massachusetts, USA)
5	HLA (EMR8-5)	#ab70328	1:100	Citrate pH 6.0	480	60	Abcam (Cambridge, UK)
6	EGFR (E235)	# ab32077	1:200	Citrate pH 6.0	780	60	Abcam (Cambridge, UK)

2.1.4 Microscope Systems

Table 2.6: Microscope Systems Used

Microscope System	Objectives	Accessories	Associated Software	Manufacturer
Incucyte S3 Live Cell in-incubator Analysis System	4x/0.20 PLAN APO, 10x/ PLAN APO (Nikon, Japan)	-Camera: CMOS Ace (Basler, Germany) -Filters: 'Green' (ex: 460nm, em: 524nm) 'Red' (ex: 585, em: 635nm) -Automated X-Y-Z stage	Incucyte® Live-cell Analysis Suite	Sartorius (Göttingen, Germany)
JuLi™ Stage Real- Time Cell History Recorder (incubator imaging system)	UPLANFL N 4x/0.13, UPLANFL N 10x/ , UPLANFL N 20x/ , UPLANFL N (Olympus, Japan)	-Camera: Monochrome CCD (SONY, Japan) -Filters: DAPI/GFP/RFP -Automated X-Y-Z stage	JuLi™ Stage Analysis Suite	NanoEntek (South Korea)
TCS SP5 Inverted Confocal System with environmental chamber (37°C, 5% CO_2)	HCX PL APO CS 10.0x/0.40, UV, HCX PL APO CS 40.0x/1.30 Oil UV, HCX PL APO CS 63.0x/1.40 Oil (Leica Biosystems, Nussloch, Germany), 20x/1.0X LUMPLFLN water immersion (Olympus, Japan)	-Fitted with Photomultiplier tubes (PMT) and Hybrid (HyD) detector -Laser: 488nm-argon, 405nm-diode, 561nm-DPSS, 633nm-HeNe -DM600 automated X-Y-Z stage (ITK, Germany)	Leica Application Suite (LAS) AF Software v.2.7.3.9723	Leica Biosystems (Hesse, Germany)

Continued on next page

Table 2.6: Microscope Systems Used (Continued)

TCS SP8 DLS (Digital Light-Sheet) inverted laser scanning microscope	10x/0.4 HC PL APO Dry, 20x/0.75 HC PL APO Dry, 40x/1.3 HC PL APO Oil, 63x/1.4 HC PL APO Oil (Leica Biosystems, Hesse, Germany)	-Fitted with Photomultiplier tubes (PMT) and Hybrid (HyD) detector -Camera: Orca Flash 4.0 V2 camera (Hamamatsu, Japan) -Laser: Laser: 488nm-argon, 405nm-diode, 561nm-DPSS, 633nm-HeNe -Filters: DAPI/GFP/DsRed/DLS 575-615nm/DLS 575-635nm -Automated X-Y-Z stage: Super Z Galvo flow	Leica Application Suite (LAS) AF Software v.2.7.3.9723	Leica Biosystems (Hesse, Germany)

2.1.5 Software

Software	Developer/Supplier
Adobe Creative Cloud	Adobe Inc. (California, USA)
CellEYE	Open Source - Dr Pablo Galvez, Children's Medical Research Institute, Westmead, Australia
CIADIAC Spheroid Analyser	Open source (Cisneros Castillo et al. [2016])
Fiji (is just Image J) software	ImageJ Open Source Software (Schindelin et al. [2012])
GIMP-GNU image manipulation program	GIMP Development Team (California, USA)
GraphPad Prism v.9.0	GraphPad (California, USA)
JuLi™ Stage Analysis Suite	NanoEnTek (South Korea)
Leica imaging software (LAS X, LAS AF)	Leica Biosystems (Hesse, Germany
Microsoft Office 365	Microsoft Corporation (Washington, USA)
Python 3.9 (via Anaconda Distribution v 2-2.4.0)	Python Software Foundation (Delaware, USA)/Anaconda Software Distribution (Texas, USA)
QuPath v0.4.4	Open Source (Bankhead et al. [2017])
Rstudio	R Studio (Massachusetts, USA)
ZEN 2 (Blue Edition)	Zeiss (Germany)

2.2 Cell Biology Techniques

2.2.1 Glioblastoma Cell Lines

"Primary patient-derived cell lines" refers to cell lines established in a defined serum-free culture to retain *in-vivo*-like tumour characteristics with limited number of passages. This differs from "continuously cultured" cell lines, which are immortalised cell lines, cultured in media that may contain serum, with no restrictions on sub-culturing. In this thesis, only primary patient-derived cell lines were used.

Four primary patient-derived GBM cell lines were kindly gifted by Professor Bryan Day, Dr Brett Stringer and Professor Andrew Boyd from QIMR Berghofer Medical Research Institute (Herston, Qld, Australia) (Stringer et al. [2019]). These cell lines were created by surgical aspiration after tumour excision of the GBM tumour that was mechanically and enzymatically disassociated prior to maintenance in cell culture.

The cell line characterisation data of the four cell lines; WK1, RN1, JK2, SJH1; have been made publicly available on the Q-Cell website (https://www.qimrb.edu.au/qcell) and are summarised in Tables 2.7 & 2.8(Stringer et al. [2019])

Table 2.7: Major Genetic and Epigenetic Features of GBM Cell Lines

Cell Line	**Major Genetic and Epigenetic Features**	**Subtype**
JK2	*TP53* R110L mutation, *PTEN* Homozygous deletion, *CDKN2A* Homozygous deletion, *CDKN2B* Heterozygous deletion	Proneural
SJH1	*MET* H289R mutation, *EPHA2* V589 & R721Q mutation,*P53* G105C mutation, *PTEN* Homozygous deletion, *CDKN2A* Homozygous deletion, *CDKN2B* Homozygous deletion, *NF1* split junction mutation	Proneural
RN1	*EGFR* gain, *MET* T992I mutation, *DKN2A* Homozygous deletion, *CDKN2B* Homozygous deletion	Mesenchymal
WK1	*PIK3CA* H1047Y mutation, *SETD2* E670K mutation, *PTEN* Homozygous deletion, *CDKN2A* Homozygous deletion, *CDKN2B* Homozygous deletion	Classical

Table 2.8: Characterisation Data of Patient-Derived GBM Cell Lines Used In This Thesis

Cell Line	Cell Type	Culutre Type	Patient Details	Derivation	Culture Conditions	Supplier
JK2	Human Glioblastoma	Primary patient-derived	-75-year-old male -Right frontal lobe -Primary tumour -178 day survival -WHO grade IV	Isolated from surgical aspirate (Day et al. 2013)	-Maintained in Glioma NeuralStem Media (GNS) media consisting of: KnockOut™DMEM F-12, 1x StemPro™ Neural Supplement, 1x Penicillin/streptomycin, 2mM L-glutamine, 20ng/mL Heparin, 20ng/mL EGF, 10ng/mL FGF -Adherent culture on 1% (v/v) Matrigel-coated plates -Sub-cultured at a ratio of 1:3-1:4 twice a week	Kindly Supplied by Brett Stringer and Bryan Day (QIMR Berghofer Medical Research Institute, QLD, Australia)
RN1	Human Glioblastoma	Primary patient-derived	-56-year-old male -Left temporal lobe -Primary tumour -243 days survival -WHO grade IV	Isolated from surgical aspirate (Day et al. 2013)	-Maintained in Glioma NeuralStem Media -Adherent culture on 1% (v/v) Matrigel-coated plates -Sub-cultured at a ratio of 1:2 once a week	Kindly Supplied by Brett Stringer and Bryan Day (QIMR Berghofer Medical Research Institute, QLD, Australia
SJH1	Human Glioblastoma	Primary patient-derived	-72-year-old male -Left temporal lobe -Primary tumour -45 days survival -WHO grade IV	Isolated from surgical aspirate (Day et al. 2013)	-Maintained in Glioma Neural Stem Media -Adherent culture on 1% (v/v) Matrigel-coated plates -Sub-cultured at a ratio of 1:2 once a week	Kindly Supplied by Brett Stringer and Bryan Day (QIMR Berghofer Medical Research Institute, QLD, Australia
WK1	Human Glioblastoma	Primary patient-derived	-77-year-old male -Right parietal/occipital lobes -Primary tumour -121 days survival -WHO grade IV	Isolated from surgical aspirate (Day et al. 2013)	-Maintained in Glioma Neural Stem Media -Adherent culture on 1% (v/v) Matrigel-coated plates -Sub-cultured at a ratio of 1:3-1:4 twice a week	Kindly Supplied by Brett Stringer and Bryan Day (QIMR Berghofer Medical Research Institute, QLD, Australia

2.2.2 Primary Tumour Cell Line Maintenance

All cell lines were maintained by Dr Victoria Prior, Dr Farhana Sakar and Samuel Bax at 37°C with 5% CO2 in a humidified Forma™ Steri-cycle™ incubator (Thermo Fisher Scientific, Massachusetts, USA) under sterile conditions in a Model BH143 Biological Biohazard Safety Cabinet Class 2 (Gelman Sciences Corporation, Michigan, USA). Cells were cultured in Matrigel™-coated, T25, T75 or T150 filter-capped plastic tissue flasks (ThermoFisher Scientific, Massachusetts, USA) as an adherent monolayer. Matrigel™ (Corning, New York, USA) is a solution of ECM proteins extracted from murine Englebreth-Holm-Swarm tumours that provides adhesive ligands to allow a successful adherent culture of HGG cells (D'Souza et al. [2020], Kleinman and Martin [2005], Pollard et al. [2009]). The coating of the tissue flasks was carried out by applying a thin layer of 1% (v/v) Matrigel solution (Matrigel™ GFR Basement Membrane Matrix LDEV-Free (v/v), DMEM High Glucose Pyruvate). The "growth factor reduced" (GFR) variety of Matrigel™ (Corning, New York, USA) was exclusively used in lieu of non-GFR Matrigel™ (Corning, New York, USA) as non-GFR Matrigel™ (Corning, New York, USA) contains growth factors such as epidermal growth factor (EGF), basic fibroblast growth factor (bFGF), insulin-like growth factor 1 (IGF-1) and platelet-derived growth factor (PDGF) which in themselves can act as a selection pressure for cells (Pollard et al. [2009]). Concurrently, culture media was supplemented with growth factors essential for the maintenance of cells. The coated tissue flasks were sealed with Parafilm (Bemis, Wisconsin, USA) and incubated overnight at 4°C. Before use, excess Matrigel™ solution (Corning, New York, USA) was aspirated and flasks were rinsed in Dulbecco's phosphate

buffered saline (DPBS; Thermo Fisher Scientific, Massachusetts, USA). Similar procedures were used for all types of plates and coverslips.

Cells were maintained in Glioma Neural Stem (GNS) media consisting of Knock-Out™DMEM F-12 (Thermo Fisher Scientific, Massachusetts, USA), 1x StemPro™ Neural Supplement (Thermo Fisher Scientific, Massachusetts, USA), 1x penicillin-streptomycin (Thermo Fisher Scientific, Massachusetts, USA), 2mM L-glutamine (Thermo Fisher Scientific, Massachusetts, USA), 20ng / mL Heparin (Sigma-Aldrich, Hesse, Germany), recombinant Human 20ng / mL EGF (Thermo Fisher Scientific, Massachusetts, USA), recombinant Human 10ng/mL FGF (Thermo Fisher Scientific, Massachusetts, USA). Media was replenished every 3 days.

The health and progression of all cell lines and cultures were monitored using a CKX41 inverted phase-contrast microscope (Olympus, Tokyo, Japan). Cells were passaged after an observed confluence of 80-90% by rinsing in DPBS before being enzymatically detached with Accutase® (Sigma-Aldrich, Hesse, Germany). Enzymatic activity was quenched with the addition of an equal volume of 1 mg/mL trypsin inhibitor (Sigma-Aldrich, Hesse, Germany). Cells were pelleted by centrifugation at 200x g for three minutes and sub-cultured at a ratio dependent on the cell line. RN1 and SJH1 lines were sub-cultured at a ratio of 1:2 once a week, while JK2 and WK1 cell lines were sub-cultured at a ratio of 1:3-1:4 twice a week (Table 2.8)

It is widely recognised that cell culture conditions act as a selection pressure in primary cell lines and that gene expression in these cell lines has the potential to change with sequential subculture (Pollard et al. [2009]). Despite this, Stringer et al. has shown that

glioma cell lines maintain morphological characteristics up to 50 passages (Stringer et al. [2019]). To minimise the effects of cell culture conditions, the subculture of the cell lines used was restricted to less than 35 passages to maintain *in-vivo* characteristics.

2.2.3 Spheroid Formation and Culture

Spheroids are aggregates of HGG cells that allow the recreation of important characteristics of the tumour microenvironment such as cell-cell interactions, nutrient diffusion and waste accumulation. Spheroid formation was kindly performed by Dr Victoria Prior. For spheroid formation, primary patient-derived GBM cells were cultured in 96-well plates (Corning, New York, USA), coated with sterile agarose solution (1.5% (w / v) Agarose (Amresco, Pennsylvania, USA), DMEM) at a density of $2.0x10^4$ cells per well in 100 μL of GNS medium at 37°C with 5% CO_2. Agarose solution was used to create a low-adherent surface to encourage the compaction of cells into spheroid. Agarose (Amresco, Pennsylvania USA) was liquefied by heating, and agarose coated plates were allowed to solidify for 20 minutes at room temperature before use. Spheroid compaction and formation occurred over five days with half-volume GNS media changes every two-three days, performed using a multichannel pipette. This process resulted in a single spheroid per well. Spheroids were collected using a P1000 pipette and deposited in 1.5 mL micro-centrifuge tubes with one spheroid per tube. The GNS media was aspirated using a P1000 pipette and spheroid washed once in 1x DPBS. DPBS was aspirated before 100 μL of fresh GNS medium was added to each micro-centrifuge tube.

2.2.4 Spheroid Invasion Assay

To replicate the range of stiffness seen in the healthy and diseased brain, a range of polyacrylamide hydrogels (PAHG) with defined Young's modulus (E) were used. The E of PAHG can be tuned by manipulating the ratio of acrylamide to cross-linking bis-acrylamide monomers and is a well-characterised method to investigate the role of the stiffness of ECM in 2D cell culture (Levental et al. [2007]). In this thesis, commercially available 96-well HTS (high-throughput system) dishes from Matrigen®(SW96-HTS-EC-EA, California, USA) were used with pre-filled PAHG of predefined stiffnesses (0.2, 0.5, 1.0, 2.0, 4.0, 8.0, 12.0, 25.0 and 50 kPa). 1% Matrigel solution was used to thinly coat each individual well to allow the adhesion-mediated interaction of spheroids with the underlying PAHG. The excess Matrigel solution was washed off with 1x PBS. Each pre-formed spheroid was washed once in sterile DPBS prior to transfer into each well of the 96 well PAHG-plates, using a P1000 pipette with 100 μL of fresh GNS media. HGG cells freely migrated away from the spheroid across the surface of the PAHG. Time-lapse images were taken every 10 minutes for a period of 48 hours, as described in section 2.4. A total of 5, 1, 3, and 4 biological replicates were performed for the JK2, RN1, SJH1 and WK1 cell lines respectively. Within each biological replicate, 3 technical replicates were performed for each substrate stiffness. Edge effects of the outer wells were accounted for with the use of PBS without a spheroid for these wells. A sample plate map is seen in Figure 2.1

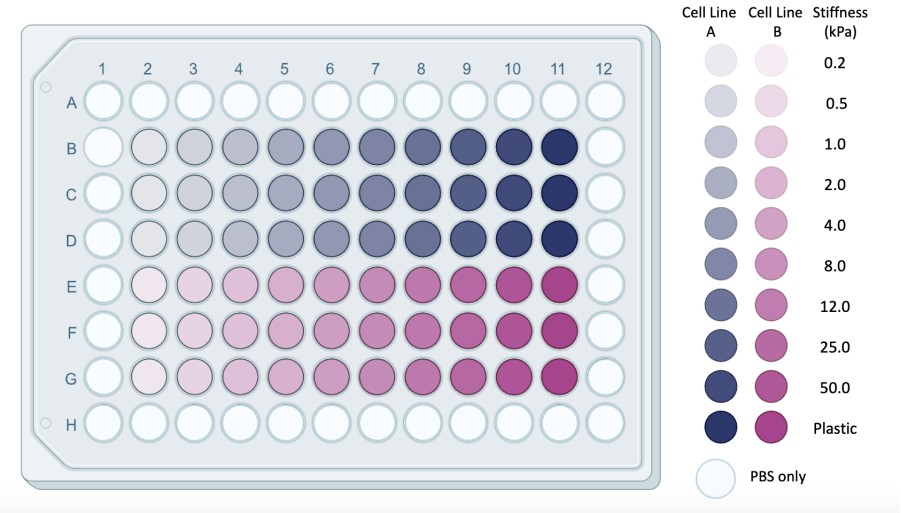

Figure 2.1: **Plate Map Used for Spheroid Invasion Assay**

Commercially available 96-well HTS (high-throughput system) dishes from Matrigen®(California, USA) were used with pre-filled PAHG of predefined stiffnesses (0.2, 0.5, 1.0, 2.0, 4.0, 8.0, 12.0, 25.0 and 50 kPa). Up to two cell lines were included in each biological replicate with three technical replicates plated for each substrate rigidity. PBS alone was used to fill the outer wells to minimise the effects of the edges.

2.2.5 Mouse Xenograft Models

Professor Bryan Day, Dr. Brett Stringer and Dr. Andrew Boyd from QIMR Berghofer Medical Research Institute (Herston, Qld, Australia) kindly donated four primary patient-derived human GBM in mouse brain xenografts as formalin-fixed, paraffin-embedded tissue blocks (FFPE) (Stringer et al. [2019]). These xenograft models were created by first culturing each of the WK1, RN1, JK2, SJH1 cell lines for 2 weeks, before 150,000 cells in 2 μl of 10 ng/ml laminin in PBS was injected 3 mm below the brain surface, 1.6 mm rostral of the bregma and 0.8 mm right of the midline in 5-week old NOD/SCID mice housed under pathogen-free conditions, using a 25G Hamilton needle and a 2 μL syringe in a stereotaxic frame. 2% isoflurane (Abbott, Illinos, USA) in oxygen was used

to anaesthetise the mice and 100 μg carprofen (Pfizer, New York, USA) administered subcutaneously was used as analgesia. The burr hole created to access the brain was sealed with bone wax and the midline scalp incision was closed with Vetbond (3M, Minnesota, USA). Mice were euthanised when they exhibited signs of significant morbidity. Please see Stringer et al. [2019] for more details.

The characterisation data of the xenografts; WK1, RN1, JK2, SJH1; have been made publicly available on the Q-Cell website (https://www.qimrb.edu.au/qcell) and are summarised in Tables 2.7 & 2.8 (Stringer et al. [2019])

2.3 Immunohistology And Microscopy

The concentrations and incubation times for all antibodies for relevant applications are specified in Section 2.1.3.

2.3.1 Tissue Blocks

All tissues were supplied as FFPE tissue blocks. Primary patient-derived human GBM in mouse brain xenografts were gifted by Professor Bryan Day, Dr. Brett Stringer, and Dr. Andrew Boyd from the QIMR Berghofer Medical Research Institute (Herston, Qld, Australia) (Stringer et al. [2019]). Normal mouse brain tissue was gifted by Professor Thomas Fath from the Dementia Research Centre (Macquarie, NSW, Australia). The normal human spleen and placenta tissue was obtained from the Children's Hospital at Westmead biobank (Westmead, NSW, Australia) and Dr. Dinny Graham from Westmead

Institute for Medical Research (Westmead, NSW, Australia).

2.3.2 Tissue Sectioning of Thick Sections

Tissue blocks were soaked in distilled water for 20 seconds prior to sectioning. The sections were cut using a Leica HistoCore BioCut rotary microtome (Leica BioSciences, Hesse, Germany) at 60 μm for thick section analysis. The cut sections were transferred to a waterbath at 40°C to enable attachment onto SuperFrost microscope slides (Thermo Fisher Scientific, Massachusetts, USA). Sections were air-dried overnight prior to de-paraffinisation and rehydration.

2.3.3 Deparaffinisation and Rehydration of Thick Sections

Slides required for staining were retrieved and baked at 58°C for 1 hour to remove excess wax, and then placed in 2 x 10 min changes of xylene to remove the remaining wax. Slides were then rehydrated in successive changes of alcohol (100%, 100%, 95%, 70%, 50%) for 15 minutes each and then submerged in running tap water for 10 min.

2.3.4 Fluorescence immunohistochemistry of thick tissues

Following deparaffinisation and rehydration, sections were washed by immersion in three successive Coplan Jars of PBS for a total of 15 mins. All wash steps described herein were performed as described above unless otherwise specified. Heat-induced epitope retrieval (HIER) was then performed using a pH 6 citrate buffer solution in a decloaking chamber

(Biocare, California, USA) for 3 min at 125°C. Slides were then washed in PBS and blocked for 5 days in 3% goat serum in PBS at 4°C in a wet chamber. Sections were then washed in PBS and incubated with primary rabbit anti-CD31 (Abcam, Cambridge, UK) antibodies over 2 days at 4°C in a wet chamber. Slides were then washed with PBS prior to being incubated with goat anti-rabbit antibodies conjugated to Alexa 568 (Abcam, Cambridge, UK) over 5 days in a wet chamber at 4°C. Sections were then mounted with glass coverslips using ProLong Gold Antifade Reagent with DAPI (Thermo Fisher Scientific, Massachusetts, USA) which provided counter-staining with DAPI. Slides were allowed to cure in a cool dark location at room temperature for at least 24 hours prior to imaging.

2.3.5 Measurement of Auto-Fluorescence Spectra

Measurement of auto-fluorescence (AF) spectra of whole tissue was performed by Dr Heeva Baharlou as part of his PhD thesis (Baharlou [2022]) and permission was granted to include the data in this thesis. 4μm unstained, deparaffinised and rehydrated sections of human colon and skin, mouse brain and rat heart were used. Sections were cut using a Leica HistoCore BioCut rotary microtome (Leica BioSciences, Hesse, Germany) and attached to SuperFrost microscope slides (Thermo Fisher Scientific, Massachusetts, USA). Slides were baked at 60°C for 40 minutes, deparaffinised in xylene and hydrated in 100% ethanol followed by Tris-buffered saline (TBS) (Amresco, Pennsylvania, USA). Following imaging, the intensity of pixels corresponding to auto-fluorescent structures was acquired using an Olympus FV1000 laser scanning confocal microscope with a

x20 objective (Olympus, Tokyo, Japan). The excitation laser lines 405nm, 473nm, and 559nm were used. Emission spectra were acquired using a 20nm wide bandpass filter and shifted in 20nm intervals from 415-795nm, 490-790nm and 575-795nm for each laser line, respectively.

2.3.6 Assessment of Effect of Auto-Fluorescence Quenching

To assess the success of auto-fluorescence quenching with Sudan Black B, 60μm sections of normal mouse brain were deparrafinised and rehydrated as outlined above and washed 3x5mins in PBS prior to incubation with Sudan Black B Solution (0.1% Sudan Black B (w/v) in 70% EtOH) for 1 hour. The effect of Sudan Black B quenching prior to, or after incubation with primary rabbit anti-CD31 (Abcam, Cambridge, UK) and secondary goat anti-rabbit conjugated Alexa 568 (Abcam , Cambridge, UK) antibodies was evaluated by imaging a single area each of grey and white cortical matter using a confocal microscope with a x63 oil immersion objective. A Z stack was acquired through the sections 3μm above and below the focus plane to capture the entirety of the section with a step size of 0.38μm. A 561nm excitation laser was used with detection spectra collected over 585-625nm. A maximum projection of the Z-stack was produced in FIJI (ImageJ, Open Source) and the average pixel intensity of the maximum projection of the z-stack was measured.

2.3.7 Immunofluorescence Analysis of Thin Sections

Sectioning, staining and imaging of thin 5μm sections of tissues was performed commercially through the Katharina Gaus Light Microscopy Facility at the Mark Wainwright Analytical Centre at The University of New South Wales. Freshly cut sections of FFPE tissue were mounted on SuperFrost microscope slides (Thermo Fisher Scientific, Massachusetts, USA) and then air-dried for 1 hour. Following this, slides were baked for 1 hour at 58°C. A Gemini AS Automated Slide Stainer (Thermo Fisher Scientific, Massachusetts, USA) was used with the DEWAX program. Sections were washed with 2 x 5 minute changes of xylene and then rehydrated in successive changes of alcohol (100%, 100%, 100%, 70%) prior to submersion in distilled water for 10 min. HIER was then performed in either pH 6 citrate buffer solution (DAKO, Glostrup, Denmark) or pH 9 EDTA buffer solution (DAKO, Glostrup, Denmark) (Section 2.1.3) in a decloaking chamber (Biocare, California, USA) for 5 min at 110°C. All wash steps were performed with three successive changes of TBS (DAKO, Glostrup, Denmark).

3,3-Diaminobenzidine (DAB) staining was performed on a Leica BOND RX automated immunostainer (Leica BioSciences, Nussloch, Germany) using the IHC F BSP program. HIER retrieved sections were washed prior to quenching endogenous peroxidase activity for 5 minutes in 3% H_2O_2 in distilled water. After repeated washing, the slides were incubated with primary antibody for 60 minutes at room temperature (Table 2.3). After washing, slides were then incubated with Post Primary (Leica BioSciences, Nussloch, Germany) (Rabbit anti-mouse IgG (10 μg/mL) in 10% (v/v) animal serum in TBS/0.1% ProClin ™950) at room temperature for 8 minutes. After washing, slides were

then incubated with Polymer (Leica BioSciences, Nussloch, Germany) Anti-Rabbit Poly-HRP-IgG (10 μg/mL) in 10% (v/v) animal serum in TBS/0.1% ProClin™950) at room temperature for 8 minutes. After washing, slides were incubated in DAB for 10 minutes prior to rinsing in distilled water. The slides were then counter-stained with haematoxylin (Leica BioSciences, Nussloch, Germany) and then washed in distilled water. Slides were then dehydrated in 4x1 minute changes of 100% ethanol followed by 3x1 minute washes in xylene as part of the IHC STD program on the Leica BOND RX automated immunostainer (Leica BioSciences, Nussloch, Germany).

Mono-plex immunofluorescence was performed on HIER retrieved sections which were washed with TBS (DAKO, Glostrup, Denmark) prior to incubation for 40 minutes at room temperature in 0.1M Glycine (VWR International, Pennsylvania, USA) in TBS (DAKO, Glostrup, Denmark). Following washes in distilled water and TBS (DAKO, Glostrup, Denmark), slides were blocked with OPAL blocking solution (Akoya Biosciences, Massachusetts, USA) for 10 minutes at room temperature. Slides were then incubated with primary antibodies for either 30 minutes or 60 minutes at room temperature (Table 2.4). Following washing, slides were next incubated with OPAL HRP Polymer Ms+Rb or Rb (Akoya Biosciences, Massachusetts, USA) for 10 minutes at room temperature. Slides were then incubated with OPAL Flurophone working solution (Akoya Biosciences, Massachusetts, USA) for 10 minutes at room temperature before treatment with an appropriate antigen retrieval buffer in a processing jar (Table 2.4). Slides were then microwaved for 45 seconds at 100% power and 15 minutes at 20% power. After cooling and washing, slides were incubated with DAPI (Sigma Aldrich, Hesse, Germany)

for 5 minutes at room temperature before being cover-slipped and mounted with Prolong Gold Anti-fade Mounting Medium (Thermo Fisher Scientific, Massachusetts, USA).

Imaging was performed using a Vectra Polaris Automated Quantitative Pathology Imaging System (Akoya Biosciences, Massachusetts, USA) with a 20x dry objective lens which captured the entirety of the slide as a stitched image. The excitation lasers lines 405 nm, 440 nm, 475 nm, 510 nm, 550 nm, 630 nm and 660 nm were used. Emission spectra were acquired using a 7 colour whole slide unmixing filter detecting emission spectra of 438-468 nm, 458-498 nm, 523-541 nm, 561-581 nm, 613-653 nm, 689-729 nm and 765-900 nm for each laser line, respectively.

The images were viewed and analysed using the QuPath Software (Bankhead et al. [2017]).

2.3.8 OPAL Multiplex Immunofluorescence Imaging of Thin Sections

Sectioning, staining and imaging of thin 5μm sections of tissues was performed commercially through the Katharina Gaus Light Microscopy Facility at the Mark Wainwright Analytical Centre at The University of New South Wales. Freshly cut sections of FFPE tissue were mounted on SuperFrost microscope slides (Thermo Fisher Scientific, Massachusetts, USA) and then air-dried for 1 hour. Following this, slides were heated for 1 hour at 58°C. In a Gemini AS Automated Slide Stainer (Thermo Fisher Scientific, Massachusetts, USA) using the DEWAX program, sections were washed with 2x5 minute changes of xylene. Sections were then rehydrated in successive changes of alcohol (100%, 100%, 100%, 70%) and then submerged in distilled water for 10 min. HIER was then

performed in either pH 6 citrate buffer solution (DAKO, Glostrup, Denmark) or pH 9 EDTA buffer solution (DAKO, Glostrup, Denmark) in a decloaking chamber (Biocare, California, USA) for 5 min at 110°C. All wash steps were performed with three successive changes of TBS (DAKO, Glostrup, Denmark). Slides were incubated for 40 minutes at room temperature in 0.1M Glycine (VWR International, Pennsylvania, USA) in TBS (DAKO, Glostrup, Denmark). Staining was then performed in a Leica BOND RX automated immunostainer (Leica BioSciences, Nussloch, Germany) with the following steps repeated for each primary antibody (Table 2.5).

Slides were blocked with OPAL blocking solution (Akoya Biosciences, Massachusetts, USA) for 10 minutes at room temperature. Slides were then incubated with primary antibodies for either 30 minutes or 60 minutes at room temperature (Table 2.5). After washing, slides were incubated with OPAL HRP polymer Ms + Rb or Rb (Akoya Biosciences, Massachusetts, USA) for 10 minutes at room temperature. Slides were then incubated with OPAL Flurophone working solution (Akoya Biosciences, Massachusetts, USA) for 10 minutes at room temperature prior. The antigen retrieval function on the Leica BOND RX automated immunostainer (Leica BioSciences, Nussloch, Germany) was performed with either BOND citrate-based pH 6 epitope retrieval solution (Leica BioSciences, Nussloch, Germany) or BOND EDTA-based pH 9 epitope retrieval solution (Leica BioSciences, Hesse, Germany) (Table 2.5). The steps from blocking of slides with OPAL blocking solution onwards were repeated for each primary antibody. After applying all relevant primary and secondary antibodies to the slides, the slides were incubated with DAPI (Sigma Aldrich, Hesse, Germany) for 5 minutes at room temperature before

being covered and mounted with Prolong Gold Antifade Mounting Medium (Thermo Fisher Scientific, Massachusetts, USA).

Imaging was performed using a Vectra Polaris Automated Quantitative Pathology Imaging System (Akoya Biosciences, Massachusetts, USA) with a 20x dry objective lens which captured the entirety of the slide as a stitched image. The excitation laser lines 405 nm, 440 nm, 475 nm, 510 nm, 550 nm, 630 nm and 660 nm were used. Emission spectra were acquired using a 7 colour whole slide unmixing filter detecting emission spectra of 438-468 nm, 458-498 nm, 523-541 nm, 561-581 nm, 613-653 nm, 689-729 nm and 765-900 nm for each laser line, respectively.

2.3.9 Image analysis of thin histological sections

Cell Detection

Stitched whole brain slice images of thin 5μm sections were analysed using QuPath software (Bankhead et al. [2017]). Using the annotation tool, regions of interest (ROI) were drawn around for each brain section. The cells were then segmented using the cell detection tool on the DAPI channel using the following parameters:

Cell Classification

These cell detections were then classified as either mouse cells (negative HLA staining) or glioblastoma cells (positive HLA staining) using the QuPath (Bankhead et al. [2017]) object classifier based on the HLA staining channel in the cytoplasm of detected cells. The

Parameter	Settings
Requested Pixel Size	0.5 μm
Background Radius	8 μm
Use Opening By Reconstruction	Yes
Median Filter Radius	0 μm
Sigma	1.5 μm
Minimum Area	10 μm ^{2}
Maximum Area	250 μm ^{2}
Threshold	2
Split by Shape	Yes
Cell Expansion	2 μm
Include Cell Nucleus	Yes

Table 2.9: **QuPath Settings for Cell Detection**

object classifier was trained using an Artificial Neural Network with a manually selected sample set of >500 glioblastoma cells and >500 mouse cells from each of the xenograft sections. The same object classifier was saved and used to classify cells for each of the xenograft sections.

Blood Vessel Detection

Blood vessel segmentation was performed using QuPath's (Bankhead et al. [2017]) pixel thresholder using the GLUT-1 staining channel with the following settings:
Detections were then created from this thresholder with a minimum size of 2μm applied to remove background noise.

Parameter	Settings
Resolution	Full (0.5 μm/px)
Prefilter	Maximum (dilation)
Smoothing Sigma	0
Threshold	4
Sigma	1.5 μm
Minimum Area	10 μm ^{2}
Maximum Area	250 μm ^{2}
Threshold	2
Split by Shape	Yes
Cell Expansion	2 μm
Include Cell Nucleus	Yes

Table 2.10: **QuPath Settings for Blood Vessel Segmentation**

Distance of Cells to Blood Vessels Measurement

The "Distance to annotations 2D" in QuPath (Bankhead et al. [2017]) was used to measure the straight-line distance of cells to the nearest blood vessels.

Nearest Neighbour Distances

The "Delaunay cluster features 2D" plugin in QuPath (Bankhead et al. [2017]) was used to measure distances between HLA positive cells. This plugin is based on Delaunay triangulation analysis, which is a geometric technique used to create a mesh of triangles from a set of points in a plane. In Delaunay triangulation, no point in the set lies inside the circumcircle of any triangle in the triangulation (Gabriel and Sokal [1969], Goltsev et al. [2018]). Those cells that had an HLA positive cell neighbour greater than 20μm away were classified as individuals, while the rest were classified as forming a cluster. 20μm

was used as the threshold distance, as it has been suggested that cells respond to stiffness changes approximately 20μm away from the cell (Buxboim et al. [2010]).

Statistical Analysis

Statistical analysis and data visualisation was performed using GraphPad Prism (GraphPad, USA). One-way analysis of variance (ANOVA) and Tukey's multiple comparison test were used to compare the distance between HLA-positive cells and GLUT-1-positive blood vessels between the cell lines JK2, RN1, SJH1 and WK1 in human GBM in mouse brain xenografts. Linear regression analysis was performed to determine the relationship between the expression of EGFR, p-EGFR, FAK, and p-FAK, if any, and GLUT-1 positive blood vessels in HLA positive cells using human GBM in mouse brain xenografts.

2.4 Spheroid Invasion Assay Imaging

Live-cell imaging was used for continuous spheroid imaging on the PAHG to investigate migration patterns using the Juli™Stage system incubator inverted microscope system (NanoEntek, South Korea). The microscope was housed within a Forma™ Steri-Cycle™ Hepa Class 100 Steri-cycle CO_2 incubator used for cell culture. In this assay, tumour cells were allowed to freely migrate away from the original spheroid. Bright-field time-lapse images were then captured over a period of 48 hours, every 10 minutes, in the '.tiff' format with bright-field illumination using a 4x objective lens. Only spheroids and the area of collective migration that did not interact with the wall of the well plate were included for

analysis.

2.4.1 Pre-processing of Spheroid Invasion Assay Images

Tumour spheroids invasion assay images were segmented into a “core” region representing the spheroid bulk, a surrounding “halo” of cells undergoing collective migration, and cells in the “periphery” which migrated mainly as individual cells (3.1).

To allow high-throughput analysis of spheroid images, time-lapse images were first converted to 8-bit ‘.png’ files using the open-source FIJI (ImageJ) software and a custom macro.

Custom Macro to Convert Time-Lapse Image to 8-bit Portable Network Graphic (.png) File

```
 macro split_stack{
dir1 = getDirectory("Choose source directory");
list = getFileList(dir1);
dir2 = getDirectory("Choose destination directory");
subst = 288;
a = 1;
Dialog.create("Input");
 Dialog.addNumber("Number of images per stack",a);
Dialog.show();
```

```
a = Dialog.getNumber();

setBatchMode(true);

for (i=0; i<list.length; i++) {

 open(dir1+list[i]);

 getDimensions(width, height, channels, slices, frames);

 counter=1;

 title = File.nameWithoutExtension;

 for (j=1; j< slices;j+=a){

  k = j+a-1;

  run("8-bit");

  run("Stack Splitter", "number="+subst);

  for (e=0; e<subst; e++)  {

  saveAs("png", dir2+title+"stack"+IJ.pad(subst-e,3)+

  ".png");

  close();

  counter+=1;

 }

 close();

}


}
```

GIMP 3.2 (GNU Image Manipulation Program, USA) was then used to convert the

resolution of the images to 1392x1040 pixels using the "Batch Image Manipulation" function.

2.4.2 High Throughput Analysis of Spheroid Core

To segment the core, which represents the spheroid tumour bulk, an adapted version of a previously published program known as the CIADIAC Spheroid Analyser was used (Cisneros Castillo et al. [2016]). This semi-automated program allowed for high-throughput analysis and corrected for uneven illumination and shadowing and is based on Otsu's threshold method (Otsu [1979]). To be compatible with the spheroid analysis program, 1392x1040 .png time lapse images were further pre-processed in FIJI (ImageJ, open source) with the "template matching" plugin, to minimise the effects of spheroid drift during the migration assay.

The CIADIAC program produced an image with the segmented areas overlaid on the original time-lapse image (Figure 2.2). A custom FIJI macro (below) was used to convert the output images into a mask. From this mask, the measure function in FIJI was used to obtain the size of the core region.

Custom Macro to Convert CIADIAC Output Image to Mask for Core Area Measurement

```
min=newArray(3);

max=newArray(3);

filter=newArray(3);

a=getTitle();

title = File.nameWithoutExtension;

run("RGB Stack");

run("Convert Stack to Images");

selectWindow("Red");

rename("0");

selectWindow("Green");

rename("1");

selectWindow("Blue");

rename("2");

min[0]=0;

max[0]=255;

filter[0]="pass";

min[1]=158;

max[1]=158;

filter[1]="pass";

min[2]=0;
```

```
max[2]=10;
filter[2]="pass";
for (i=0;i<3;i++){
  selectWindow(""+i);
  setThreshold(min[i], max[i]);
  run("Convert to Mask");
  if (filter[i]=="stop")  run("Invert");
}
imageCalculator("AND create", "0","1");
imageCalculator("AND create", "Result of 0","2");
for (i=0;i<3;i++){
  selectWindow(""+i);
  close();
}
selectWindow("Result of 0");
close();
selectWindow("Result of Result of 0");
rename(a);
```

2.4.3 High Throughput Analysis of Spheroid Periphery

The CIADIAC Spheroid Analyser program (Cisneros Castillo et al. [2016]) was also used to segment images into areas which represent single cell migration using a Canny edge

detection (Canny [1986]). 1392x1040 .png time-lapse images were used in this analysis without “template matching”. As a Canny edge detection is used, the resultant binary image does not directly image the number of cells, but rather the analysis is based on the proposition that as the number of cells increases, the number of detected edges increases.

The CIADIAC program produced images with the segmented areas overlaid on the original time-lapse image (Figure 2.2). A custom FIJI macro (below) was used to convert the output images into a mask image. From this mask image, the measure function in FIJI was used to obtain the area of cells migrating as individuals.

Custom Macro to Convert CIADIAC Output Image to Mask for Periphery Area Measurement

```
min=newArray(3);

max=newArray(3);

filter=newArray(3);

a=getTitle();

run("HSB Stack");

run("Convert Stack to Images");

selectWindow("Hue");

rename("0");

selectWindow("Saturation");

rename("1");

selectWindow("Brightness");
```

```
rename("2");

min[0]=100;

max[0]=180;

filter[0]="pass";

min[1]=0;

max[1]=255;

filter[1]="pass";

min[2]=144;

max[2]=255;

filter[2]="pass";

for (i=0;i<3;i++){

  selectWindow(""+i);

  setThreshold(min[i], max[i]);

  run("Convert to Mask");

  if (filter[i]=="stop")  run("Invert");

}

imageCalculator("AND create", "0","1");

imageCalculator("AND create", "Result of 0","2");

for (i=0;i<3;i++){

  selectWindow(""+i);

  close();

}
```

```
selectWindow("Result of 0");

close();

selectWindow("Result of Result of 0");

rename(a);
```

To minimise the effects of any extraneous structures (e.g. impurities in the hydrogel or shadows) present at t = 0, measurements of the area of single cell migration are reported as an increase in area compared to time t=0.

2.4.4 High Throughput Analysis of Cells Migrating as a Group Using a Spheroid Assay

Whilst the CIADIAC spheroid analyser program (Cisneros Castillo et al. [2016]) was effective in the segmentation of the core and area of cells migrating as individuals, the programs' use of a watershed algorithm struggled to segment the area of collective migration particularly during diffuse cell migration. To overcome the issue of segmenting a diffuse area of collective migration with ill-defined boundries, a custom program was developed alongside Dr Pablo Galaviz (Children's Medical Research Institute) which allowed for the semi-automated segmentation of the area of collective migration with a semi-automated estimate of the error in the measurement (Figure 2.2). This program, CellEye, can be accessed freely via https://github.com/pablogalaviz/CellEye.

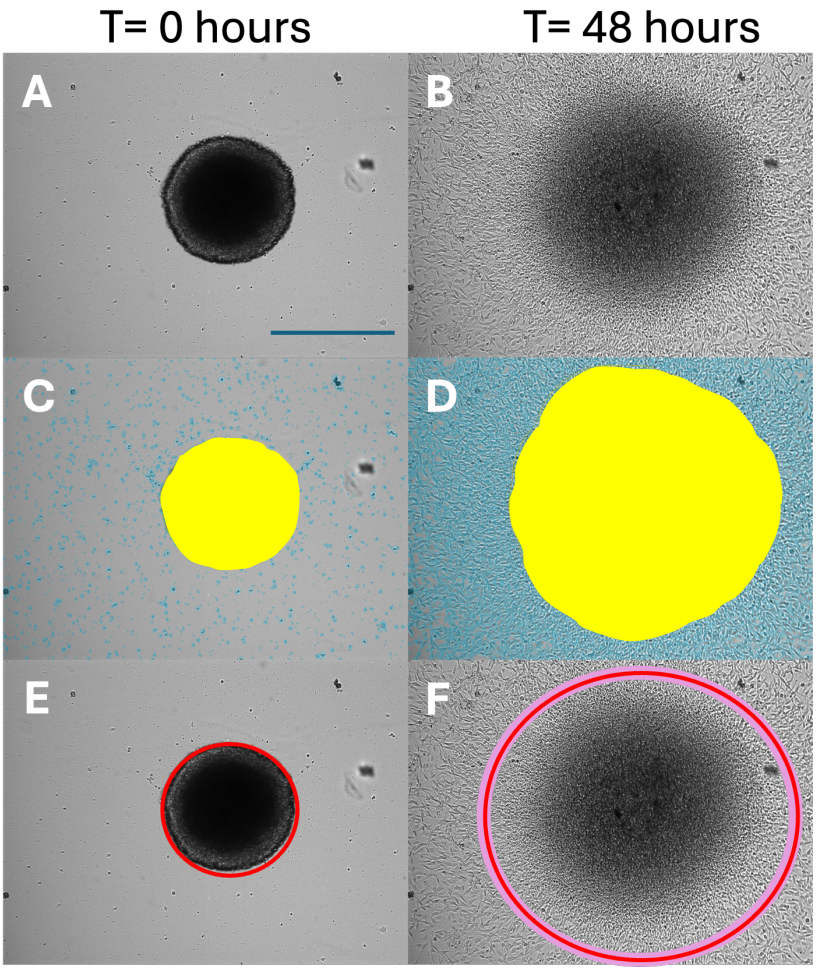

Figure 2.2: **Segmentation of Spheroid Images**

Representative bright-field images illustrate a typical spheroid cultured on a PAHG at T=0 hours (**A**) and T=48 hours (**B**). The CIADIAC Spheroid Analyser segmented the spheroid (yellow) and the peripheral cells (blue) (**C & D**). To analyse the area of cells migrating as a group, the custom program CellEye was used to estimate this area (red) with an estimate of the error in this measurement also obtained (pink) (**E & F**). As the boundary of the spheroid was ill-defined in diffuse emigration, the spheroid itself was included in the area of collective migration. Scale bar = 500 μm

Morphology Shape Analysis

The morphology of the cells that migrated out from spheroid on various substrate stiffnesses was determined at t=48 hours using the raw time lapse images. The images were analysed in FIJI (ImageJ, open source) using a custom macro (Shown Below). Images were first processed with the "despeckle" function to remove background noise, which utilised a median filtering method. Following this, images were converted to 8-bit to allow for subsequent thresholding. Images were colour inverted to allow for subsequent analysis. The "Auto-Local Threshold" function was utilised using the "mean" thresholding method to segment the migrating cells. The "Open" morphological function was utilised to further remove noise and isolated pixels, which combines an erosion operation, followed by dilation. The "Analyze Particles" functions was then used to filter and measure detections which had an area larger than 400 pixels and circularity greater than 0.01. Circularity was defined as:

$$Circularity = \frac{4\pi Area}{Perimeter^2} \tag{2.1}$$

Custom Macro to Measure the Circularity of Cells Migrating as Individuals Out Of the Spheroid

```
macro split_stack{

dir1 = getDirectory("Choose source directory");

list = getFileList(dir1);

dir2 = getDirectory("Choose destination directory");

setBatchMode(true);

for (i=0; i<list.length; i++) {

 open(dir1+list[i]);

  run("Despeckle");

  run("8-bit");

  run("Invert");

  run("Auto Local Threshold", "method=Mean radius=5

  parameter_1=0 parameter_2=0 white");

  run("Open");

  run("Analyze Particles...", "size=400-Infinity

  circularity=0.01-1.00 show=[Overlay Masks] exclude

  clear include add");

  run("Set Measurements...", "area mean min centroid

  perimeter shape feret's skewness kurtosis area_fraction

  redirect=None decimal=3");

  roiManager("Measure");
```

```
    filename = list[i];
    saveAs("Results", dir2 + File.separator + filename +
    ".csv");
    roiManager("reset");
    run("Clear Results");
    close();
  }
  }
```

2.5 Systematic Review

Systematic review was conducted in accordance with the Preferred Reporting Items for Systematic Reviews and Meta-Analysis (PRISMA) guidelines (Page et al. [2021]) and registered with the international prospective register of systematic reviews (PROSPERO 2024) (Registration Number: CRD42024567910), available from: https://www.crd.york.ac.uk/prospero/display_record.php?ID=CRD42024567910)

2.5.1 Search Methods

Ovid MEDLINE, Ovid Embase, PubMed, Web of Science and Google Scholar were searched on 11 July 2024. Combined database-specific subject headings with free text terms in the title, abstract and keyword fields for “Brain”, “Tumour”, “Cancer”, “MRE” and “Magnetic Resonance Elastography” were used. Articles with the term “review” in

the title and keyword field were excluded. Literature search files were downloaded in the ".ris" format and imported into Covidence (Covidence systematic review software, Veritas Health Innovation, Melbourne, Australia. Available at www.covidence.org.) which is a web-based collaboration software platform that streamlines the production of systematic reviews and other reviews of the literature. 2,203 studies were identified from database searching with 1,000 studies identified from Ovid MEDLINE, 511 studies identified from PubMed, 408 studies identified from Ovid Embase, 212 studies from Web Of Science and 72 identified from Google Scholar.

2.5.2 Study Screening

Of the 2,203 studies, 866 duplicate records were removed by Covidence.

Two reviewers evaluated the abstracts of the remaining 1,337 studies based on the following criteria:

1. **Inclusion Criteria**

   (a) Publications in English

   (b) Peer-Reviewed Journal Articles

   (c) Full-Text Articles

   (d) MRE on entirely normal healthy human brain with and without comparison to human subjects with brain tumours OR MRE in animal models reporting on results of tumours in the brain with and without comparison to healthy controls

2. **Exclusion Criteria**

   (a) Literature Review, Systematic reviews/Meta-analyses , Conference Abstracts, Thesis, Pre-Print Articles

   (b) Studies not reporting quantitative data

   (c) Studies without a statement of Ethics

1,229 studies were removed for not meeting all inclusion criteria or meeting exclusion criteria. Full-text review was performed for the remaining 202 studies, 112 studies were removed because they did not meet all inclusion criteria or exclusion criteria. The reasons for exclusion are summarised in Figure 5.1. A total of 90 studies were included in this thesis for systematic review.

2.5.3 Data Extraction

The following data was extracted from the selected studies by a reviewer and saved as an Excel spreadsheet (Microsoft Corporation, Washington, USA):

1. **Study Characteristics**

   (a) First Author

   (b) Year of Publication

   (c) Sample Size

2. **Clinical Characterisation**

(a) Age

(b) Sex

(c) Tumour Type (if applicable)

3. **MRE Parameters**

(a) Resolution

(b) Analysis Algorithm

(c) Transducer Frequency

(d) Measurement Location

4. **Outcomes**

(a) Estimate and Modality of Stiffness Measurements

The appendices were also reviewed for data. The estimates of the stiffness measurements were summarised as mean estimates with standard deviation estimates also collected, and segregated by the modality of the stiffness measurements obtained (see Chapter 5 for more information).

Where data were only presented as graphical data, PlotDigitizer (https://plotdigitizer.com) was used to extract the data. PlotDigitizer is a Java-supported programme that allows extraction of raw data from X-Y-type scatter or line plots (Aydin and Yassikaya [2022], Jelicic Kadic et al. [2016]).

Where data were not presented as mean and standard deviation, methods previously described by Wan et al. and Chi et al. were used to obtain estimates of the mean and

standard deviation of the data presented in the studies (Chi et al. [2023], Wan et al. [2014]).

2.5.4 Data Analysis

As factors such as transducer frequency and brain subregion influence the measured stiffness reported (Manduca et al. [2021], Pillai and Franze [2024]), data was segmented by these two factors and a subgroup analysis was performed. The methods described by Neyeloff et al. were used to estimate the mean stiffness of the population, segregated by the stiffness modality for each reported brain region at each reported frequency. This method allows for the meta-analysis of data using a Microsoft Excel spreadsheet (Microsoft Corporation, Washington, USA), using either a fixed-effects or random-effects model. Where random-effects modelling could not be used due to a single study sample, a fixed effects model was used to estimate the mean and errors of the population (Neyeloff et al. [2012]). The test for intra-study heterogeneity was measured using the Cochran Q test (Q) and I^2. Q is calculated as the weighted sum of squared differences between the effects of the individual study and the pooled effect between the studies (Neyeloff et al. [2012]). I^2 is expressed as a percentage of the total variability in a set of effect sizes due to heterogeneity, with higher values indicating more heterogeneity between studies. (Melsen et al. [2014], Neyeloff et al. [2012]).

Linear regression analysis was performed using Graphpad Prism (GraphPad, California, USA). Comparative statistics were performed using a Z-test with $\alpha = 0.05$.

Chapter 3

Mechano-Regulation of Single-Cell & Multi-cellular Emigration

---

The challenges in treating glioblastoma (GBM) are closely related to the highly migratory and invasive nature of GBM (Weller et al. [2015]), which are influenced by mechanosensation, a process in which cells interact with mechanical cues in their environment (Sarker et al. [2020]). Mechanosensation involves focal adhesions (FAs) that connect the cell cytoskeleton to the extracellular matrix (ECM) (Burridge et al. [1988], Elosegui-Artola et al. [2018], Kechagia et al. [2019]). As reviewed in chapter 1, GBM cells migrate using two main modes: mesenchymal migration, characterised by strong adherence to ECM and elongated morphologies, and amoeboid migration, characterised by weak adherence to ECM, rapid movement, and rounded cell bodies (Friedl and Alexander [2011], Hecht et al. [2015], Panková et al. [2010]). Cells can switch between these modes on the basis of various factors, including substrate stiffness (Friedl and Wolf [2010], Taddei et al. [2013],

Talkenberger et al. [2017]). Under conditions of low adhesion and high confinement, fibroblasts transition from mesenchymal migration to more rapid amoeboid types, a shift referred to as the mesenchymal to amoeboid transition (MAT) (Liu et al. [2015]). This change gives rise to two distinct amoeboid subtypes: the pseudopod mode, which is characterised by actin-rich extensions at the leading edge, and the stable bleb mode, which consists of a stable bleb lacking actin. The pseudopod mode involves localised assembly of actin and moderate contractility, whereas the stable bleb mode is driven by high global cortical contractility and rearward actomyosin flow. The stable bleb mode, especially, might play a crucial role in embryonic morphogenesis and invasion of cancer cells, providing a connection at the mechanistic level between cell movement and tissue dynamics in both normal and disease situations (Liu et al. [2015], Ruprecht et al. [2015], Welch [2015]).

Mechanosensation affects physiological and pathological processes and involves cell-cell and cell-ECM adhesion (Rea et al. [2013], Sarker et al. [2020], Umesh et al. [2014], Xin et al. [2023]). Studies show that substrate stiffness and cell-ECM adhesion influence cell fate (Engler et al. [2006]). In GBM, tumour cell interactions, especially in multicellular networks, play a crucial role in invasion (Canel et al. [2010], Gritsenko et al. [2017, 2012], Haeger et al. [2015], Osswald et al. [2015], Wu et al. [2021], Xin et al. [2023]).

In this chapter, the migration behaviour of four primary patient-derived GBM cell lines, representing the classical, proneural, and mesenchymal subtypes (Table 2.7), was investigated using a spheroid model to analyse the effect of cell-cell and cell-substrate

adhesions with change in substrate stiffness. Subsequently, publicly available RNA sequencing data, obtained at the time the cell culture was established, was analysed to identify differentially expressed genes and integrate with migration behaviour analyses.

3.1 Tumour Spheroid Model

As discussed in section 1.8, while single-cell assays have significantly advanced our knowledge of the environmental influences on HGG biology, they fail to capture the intricate mechanical interactions of HGG cells with each other, other cell types, and the broader ECM *in-vivo* (Cukierman et al. [2001], Haeger et al. [2015], Simian and Bissell [2017], Vollmann-Zwerenz et al. [2020]). As such, HGG migration and behaviour *in-vitro* poorly correlate to clinical observations of HGG migration and behaviour *in-vivo* and may help explain, in part, the lack of new therapies for GBM (Manini et al. [2018], Shergalis et al. [2018]).

The need to observe the behaviour of HGG cells in models with increased dimensionality to better replicate the *in-vivo* conditions, has led to the creation of spheroid models. These 3D models recapitulate cell-cell interactions, tumour architecture, and biochemical effects such as tumour hypoxia (Costa et al. [2016], Mark et al. [2020], Nath and Devi [2016], Nunes et al. [2019], Ryan et al. [2001]).

In this chapter, three-dimensional spheroids composed of primary patient-derived HGG cells, characterised by a pre-established single-cell mechanosensitive phenotype

and GBM subtype classification, were cultured on 2D mechanically tuned polyacrylamide hydrogels (PAHG), simulating the spectrum of physiological and pathological tissue stiffness (Arani et al. [2015], Chauvet et al. [2016], Franze [2013], Grundy et al. [2016], Paszek et al. [2005]). Within this experimental context, tumour cells were permitted to migrate freely from the spheroids. 2D assessments of cell emigration from 3D spheroids enabled differentiation between cells emigrating individually and those migrating in groups. This movement was influenced by interactions between cells and between cells and the substrate. Bright-field time-lapse imaging was conducted over a 48-hour period, capturing images every 10 minutes. Subsequently, the migration behaviours of the cells were quantified. The choice of 2D analyses, as opposed to 3D models with embedded spheroids, provided enhanced experimental control by restricting emigration to a single plane. This arrangement facilitated straightforward comparisons with previous studies on cancer cell emigration, many of which employ 2D models (Grundy et al. [2016], Nunes et al. [2019], Ryan et al. [2001], Wu et al. [2021]).

3.1.1 Migration of HGG Cells From the Spheroid Bulk Form Distinct Regions

To investigate how cell-cell and cell-ECM interactions jointly influence cellular mechanical responses, pre-formed spheroids were cultured on PAHGs with stiffness ranging from 0.2 to 50 kPa. Time-lapse imaging was undertaken over 48 hours. In the spheroid formation process, HGG cells engage in cell-cell interactions without involving cell-substrate interactions, leading to spheroid compaction (Han et al. [2021], Nath and Devi [2016]). Limited diffusion of oxygen and nutrients through the spheroid bulk, along with

the build-up of metabolic waste, results in three distinct concentric zones: a necrotic hypoxic core, a quiescent intermediate layer, and an outer layer of proliferating cells (Nath and Devi [2016]).

When spheroids are plated on a commercially supplied PAHG surface, coupled to a thin layer of Matrigel™ to allow cells to attach to the underlying substrate, the introduction of cell-substrate interactions coupled with biochemical pressures induced HGG cells to migrate away from the spheroid bulk onto the PAHG (Figure 3.1) (Berrier and Yamada [2007], Friedl et al. [2012], Friedl and Wolf [2003]).

Observing HGG emigration from the spheroid at times $t = 0$ and $t = 48$ hours, three distinct concentric zones form (Figure 3.1). Initially, at $t = 0$ hours, only the spheroid can be seen without any single-cells on the surrounding PAHG. By $t = 48$ hours, the three distinct zones are composed of cells that remain within the spheroid, cells engaged in collective migration that utilise both cell-cell and cell-substrate adhesions, and cells that migrate individually without cell-cell adhesions (Figure 3.1) (Nath and Devi [2016]).

3.1.2 Initial Migration of HGG Cells From the Spheroid Vary Between Cell Lines

Spheroids for each cell line were generated by seeding 1.5x10^4 cells in ultra-low attachment plates. Over five days, the cells aggregated to form a spheroid which was subsequently moved to the PAHG. Figure 3.2 shows representative bright-field images of spheroids at $t = 0$ after being plated on PAHG for each cell line. Although the initial cell seeding was consistent across cell lines, the spheroid size differed between each cell line (Figure 3.3). RN1 (mesenchymal) spheroids were smaller compared to JK2

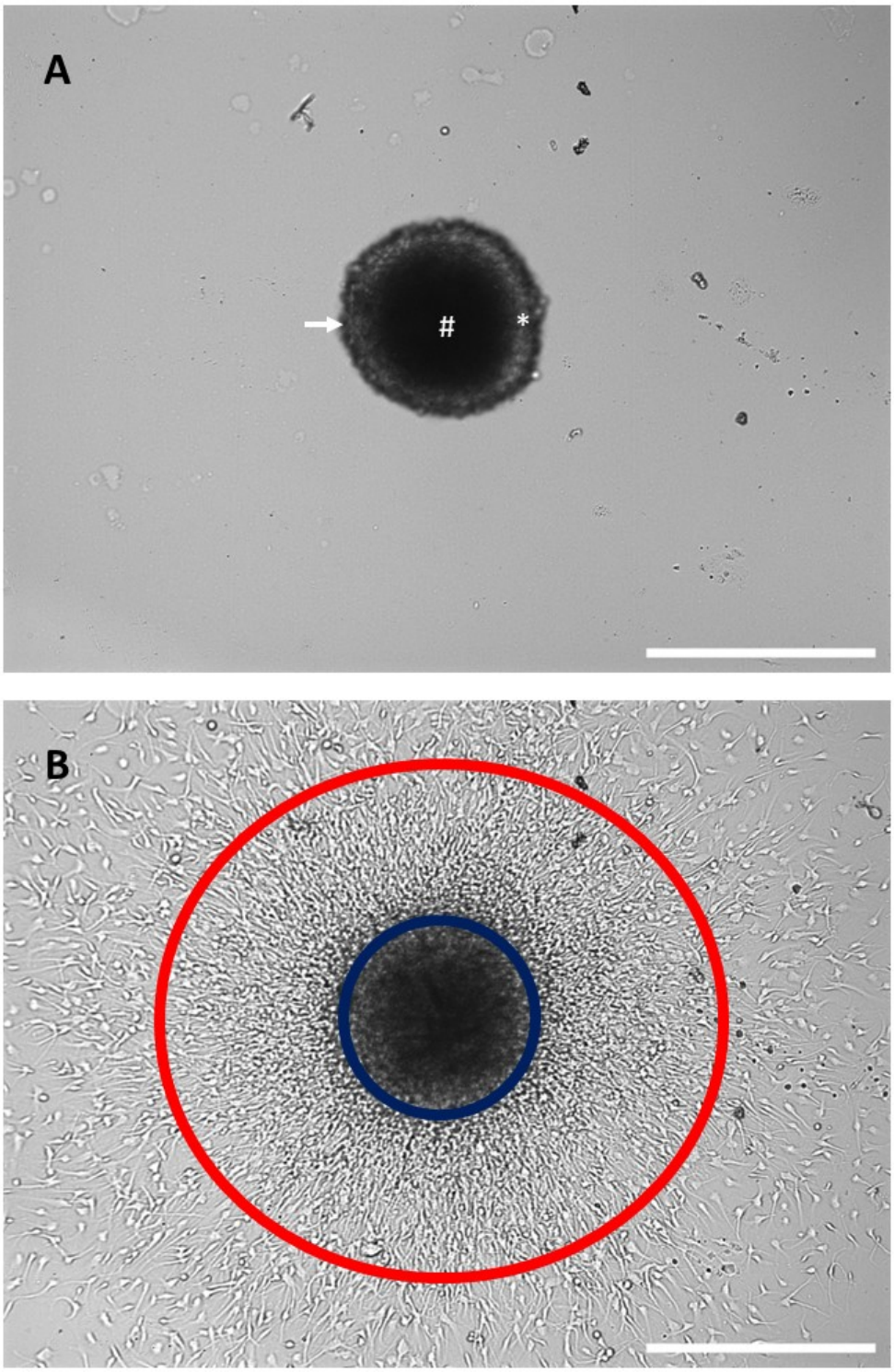

Figure 3.1: **Migration of HGG Cells From the Spheroid form Distinct Regions.**

Bright-field images illustrate a typical spheroid cultured on a PAHG. **A.** At time = 0, the spheroid reveals three distinct zones: a hypoxic core with necrosis (#), a middle layer containing quiescent cells (*), and an outer layer comprised of proliferating cells (white arrow). **B.** After 48 hours, the HGG cells migrate from the spheroid, forming three layers: HGG cells that remain within the spheroid (enclosed by a blue circle), cells engaging in collective migration (located between the blue and red circles), and HGG cells migrating individually (situated beyond the red circle). Scale bar = 500 μm

(proneural) and SJH1 (proneural) spheroids, which were, in turn, smaller than those of WK1 (classical). These variations were considered to indicate differences in proliferation or compaction capacity. However, growth rate quantification revealed no correlation between proliferation and spheroid size differences (Grundy [2019]). Growth rates were assessed by Grundy by plotting the confluence of cell lines in 96-well plates over time, using the slope at the curve's inflection point to represent growth rate. JK2 exhibited the highest proliferation rate, followed by RN1, while SJH1 and WK1 showed the lowest rates (Grundy [2019]). This lack of correlation suggests that variations in cell-cell interactions in themselves could enhance compaction, ultimately leading to smaller spheroids.

For the JK2 and RN1 GBM cell lines, only a small number of cells were observed to detach from the spheroids (Figure 3.2). In contrast, an increased migration of HGG cells from spheroid is observed in the SJH1 and WK1 GBM cell lines. These findings could indicate variations in the balance between cell-cell adhesion and cell-substrate interactions (Nath and Devi [2016], Ryan et al. [2001]).

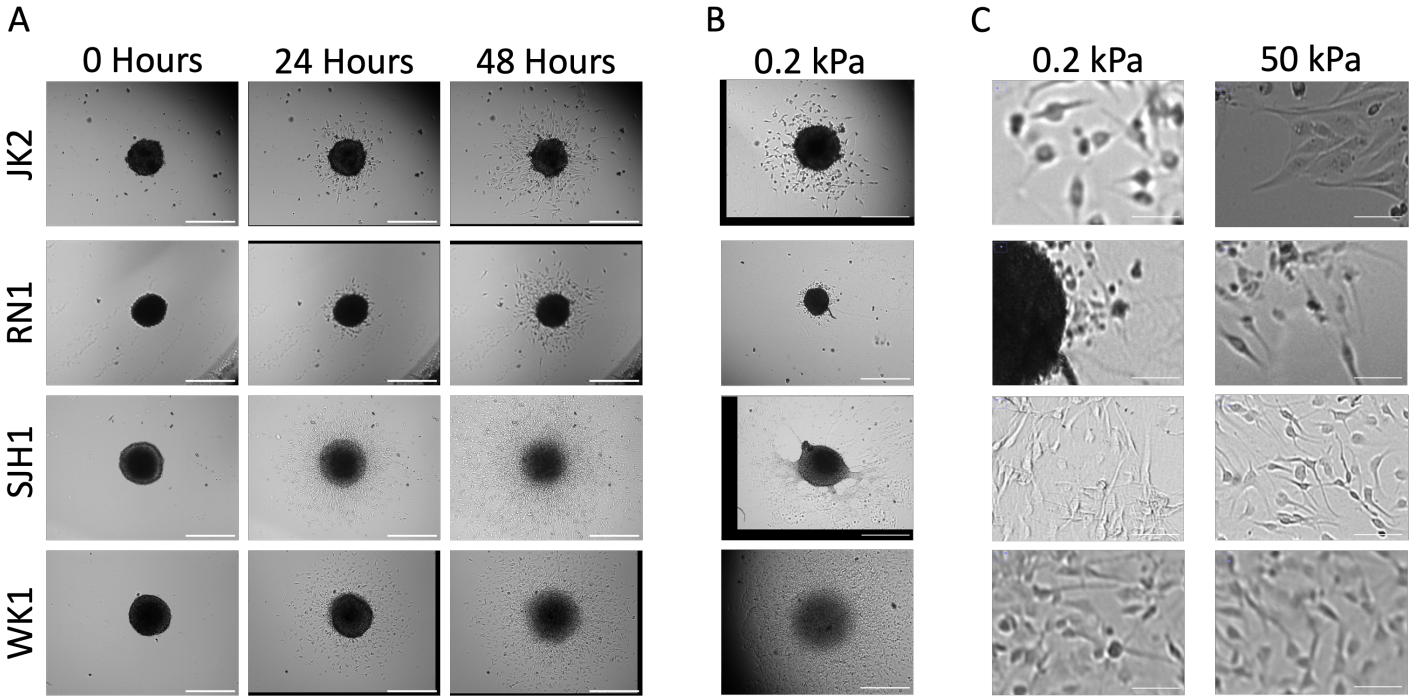

Figure 3.2: **Migration of HGG Cells from Spheroids on Polyacrylamide Hydrogels for Four Patient-Derived Primary Cell Lines**
A) Displayed are selected bright-field time-lapse images of spheroids cultured on 50kPa hydrogels using four distinct patient-derived primary cell lines: JK2, RN1, SHJ1, and WK1. The images capture the time points of 0, 24, and 48 hours following the plating of spheroid on the hydrogels. **B)** Shown are representative bright-field images of spheroids at 48 hours post-plating on PAHGs with tuned mechanical properties. The images illustrate the extremes of substrate stiffness used, comparing the softest (0.2kPa) with the stiffest (50kPa) substrates (last column of part (A)) for the four primary cell lines investigated in this chapter. **C)** Shown are representative bright-field images of spheroid assays at 48 hours post-plating on PAHGs to highlight the morphology of migrating HGG cells away from the spheroids, comparing the softest (0.2kPa) with the stiffest (50kPa) substrates. The scale bars measure 500 μm (parts **A** & **B**) and 80 μm (part **C**)

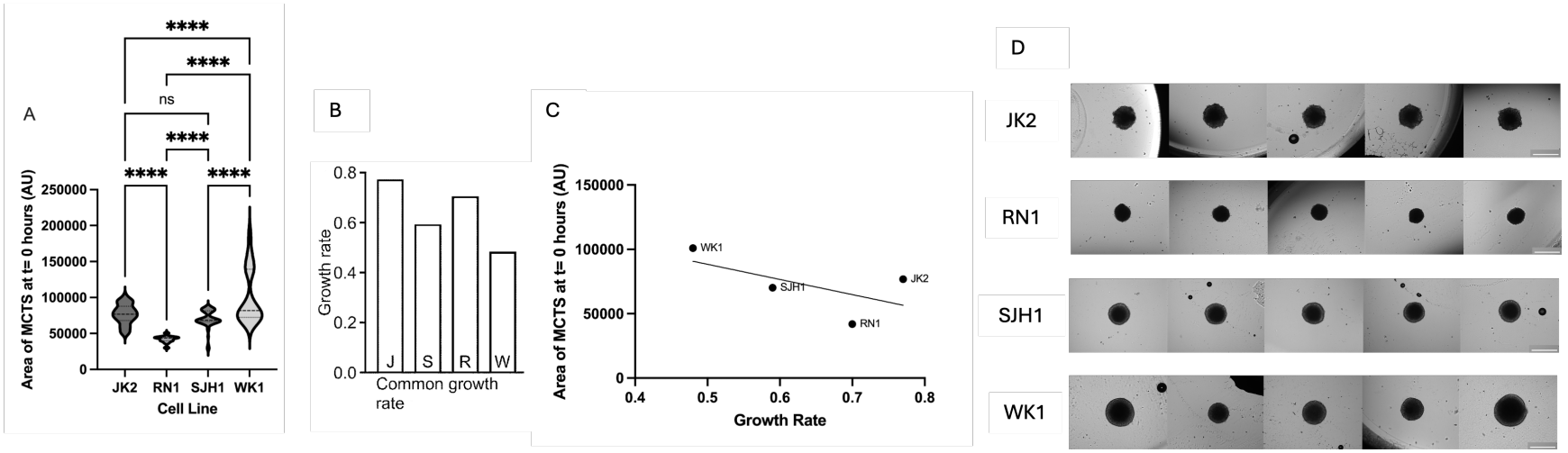

Figure 3.3: **Area of Spheroids After Compaction Varies Between Cell Lines**

A) Tumour spheroids (MCTS) for each cell line were developed with an initial seeding density of $1.5x10^4$ cells per well. These were left to compact and form a spheroid over a 5-day period. At time =0 hours after being plated onto PAHG, the area of each spheroid was measured using bright-field 2D images and pooled for all stiffness conditions (arbitrary units). A one-way ANOVA followed by Tukey's multiple comparisons test was carried out. Significance is indicated by symbols: ns, no significant difference; ****; $p<0.0001$ **B)** Growth rates were determined by analysing confluency data from cell lines cultured in 96-well plates. The growth rate was calculated from the slope of the inflection point of a logistic function when the confluency data was plotted over time. Cell lines are labelled [J]K2, [S]JH1, [R]N1, and [W]K1. Data, analysis and figure were provided by Dr Thomas J Grundy in his PhD thesis (Grundy [2019]). Data pooled from 3 biological replicates with $N \geq 4$ technical replicates per biological replicate. Further information on methodology and analysis can be found in Grundy [2019] **C)** The average area of the spheroid at time =0 hours was plotted against previously reported growth rates (Grundy [2019]). The linear regression line is displayed. An F test was conducted to determine if the slope is significantly non-zero, yielding P= 0.3831. The number of spheroids analysed includes: 45 JK2, 13 RN1, 67 SJH1, 22 WK1. **D)** Representative images of tumour spheroids at time =0 hours after being plated onto PAHG for each cell line. The scale bars measure 500 μm

3.1.3 Morphological Distinctions of Migrating Cells Inherent to Cell Lines and Substrate Stiffness

Cell morphology is strongly influenced by the stiffness of the underlying matrix. In general, GBM cells tend to exhibit rounder shapes on substrates with lower stiffness, whereas they adopt more elongated forms on stiffer substrates (Grundy et al. [2016], Kumar et al. [2016]). Weak attachment to a softer substrate diminishes strain within the cytoskeleton, resulting in reduced cell spreading. As a consequence, these cells adopt a round, dome-shaped, "amoeboid" morphology. In contrast, robust attachment to a firmer substrate leads to extensive cell spreading, giving rise to a "mesenchymal" appearance (Bell et al. [2019], Friedl et al. [2012], Friedl and Wolf [2003]).

The morphological response of GBM cells to tissue stiffness has previously been reported in cells that have been deliberately plated at low density to ensure that there is no cell-cell contact (Grundy et al. [2016], Kumar et al. [2016]). However, the impact of cell-cell interactions on the integration of mechanosensing and morphology remains uncertain. Thus, this question was addressed by quantifying the morphology of single cells that had actively migrated from the spheroid, here referred to as emigration, to emphasise the difference from earlier experiments where cells were plated as single cells and migration tracked. On soft substrates, individually emigrating JK2 HGG cells have rounded morphologies with limited cytoplasmic spread (Figure 3.2 & 3.4). In contrast, on more stiff substrates, the emigrating cells display a spindle-like morphology. Cell morphologies were next quantitatively assessed. A local automatic threshold was applied using FIJI (ImageJ Open Source Software) to segment the emigrating cells at $t = 48$

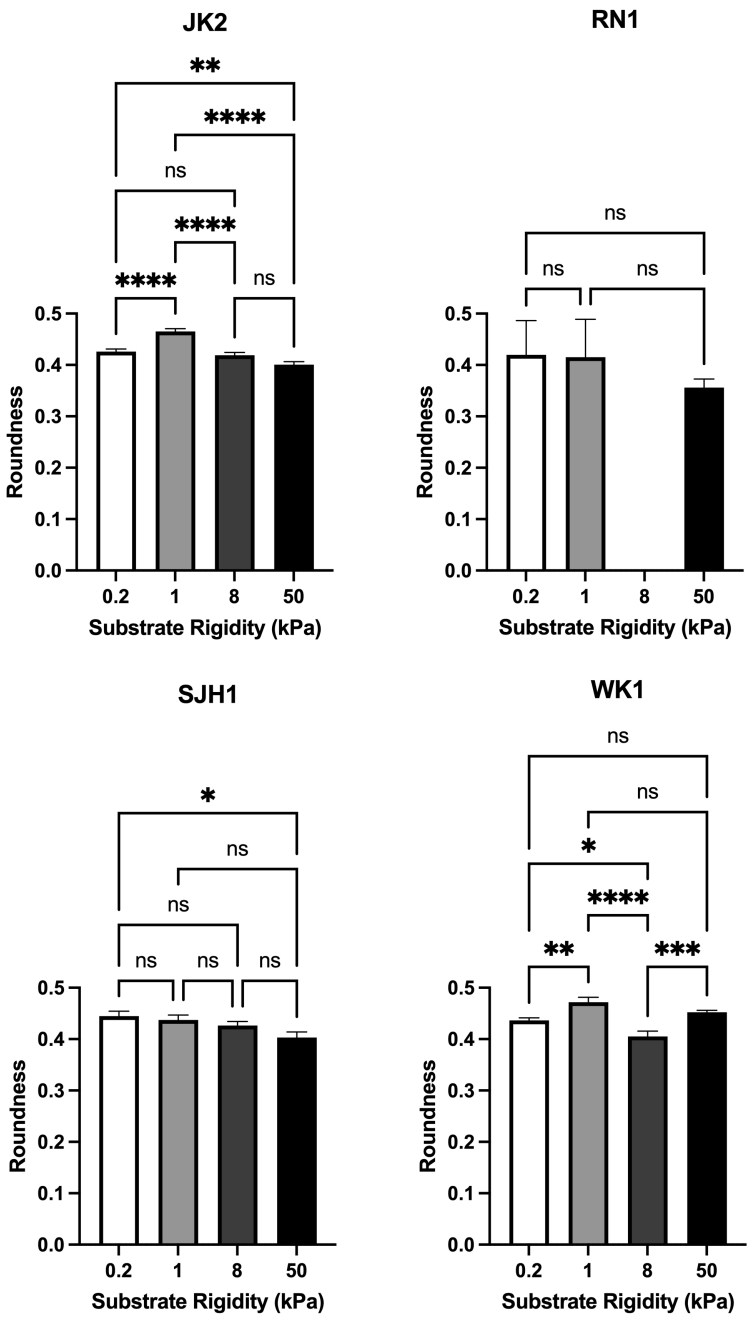

Figure 3.4: **Morphology of Migrating HGG Cells Over Increasing Substrate Stiffness**

The average cell roundness, calculated as $(4A/\pi M^2$; where A represents the area and M the Major Axis), is presented for cells cultured on PAHG gels exhibiting increasing stiffness values (0.2, 1.0, 8.0, 50kPa). For the JK2 condition, more than 1312 cells were analysed per stiffness condition. For RN1, over 12 cells were examined per condition. SJH1 involved analysis of more than 399 cells per condition, and for WK1, the analysis included over 321 cells per stiffness condition. Significance levels are indicated by *p<0.05, **p<0.01, ***p<0.001, and ns for non-significant results, all determined via One-way ANOVA and Tukey's post hoc test. Error bars represent the standard error of the mean (SEM).

hours. More information on analysis can be found in Chapter 2. Morphology of the cells were described by "roundness" (Figure 3.4) which was calculated by the formula :

$$Roundness = \frac{4 \times Area}{\pi \times MajorAxis^2} \tag{3.1}$$

A roundness of 1 represents a perfect circle, while values below 1 suggest greater elongation of cells. JK2 cells respond biphasically to increased substrate stiffness with a general trend for reduced roundness with increasing substrate stiffness, except on the 1 kPa substrate (Figure 3.4). The morphology of emigrating RN1 cells was found to be influenced by the stiffness of the substrate with a reduced roundness as the stiffness of the substrate increased (Figure 3.2); however, no statistical significance was demonstrated (Figure 3.4), likely reflecting the low number of cells available for analysis.

Both SJH1 and WK1 cell lines displayed a predominantly spindle-shaped morphology during emigration under both soft and stiff substrate conditions (Figure 3.4). Interestingly, SJH1 cells demonstrated reduced roundness with increasing stiffness. In contrast, WK1 cells, despite having significant differences in roundness in different substrate stiffnesses, did not demonstrate a clear trend with increasing substrate stiffness.

Overall, except for WK1 cells, all other cell lines exhibited more spread, spindle-shaped morphologies on stiffer substrates. These observation might indicate differences in adhesion to the underlying substrate among the cell lines (Grundy et al. [2016]). This can help classify the morphology of JK2, RN1, and SJH1 cell lines as being mechano-sensitive, while WK1 maintains mechano-insensitivity to stiffness in terms of morphology

during single-cell emigration (Table 3.1)

Cell Line	Morphology on Soft Substrate	Morphology on Stiff Substrate	Influence of Substrate on Morphology
JK2 (Proneural)	Amoeboid (Rounded)	Mesenchymal (Spindle)	Stiffness- Sensitive
RN1 (Mesenchymal)	Amoeboid (Rounded)	Mesenchymal (Spindle)	Stiffness- Sensitive
SJH1 (Proneural)	Mesenchymal (Spindle)	Increased Mesenchymal (Spindle)	Stiffness- Sensitive
WK1 (Classical)	Mesenchymal (Spindle)	Mesenchymal (Spindle)	Stiffness- Insensitive

Table 3.1: **Morphology of individually emigrating HGG cells, relative to substrate stiffness**

3.2 Single-Cell Emigration

HGG emigration from spheroids display a cell-line-dependent emigration pattern that employ both single-cell and collective emigration (Figure 3.2). In collective emigration, cells maintain connections with one another (Demuth and Berens [2004], Haeger et al. [2015]). JK2 cells exhibit minimal collective emigration, whereas WK1 mainly display collective emigration. Overall, the four GBM cell lines demonstrated a variety of emigration patterns, with cells migrating from the spheroids as both solitary units and groups (Figure 3.2, 3.5 & 3.6). These findings underscore the plasticity of cell migration within each line (Demuth and Berens [2004], Haeger et al. [2015], Wu et al. [2021]), emphasising both inter-tumour and intra-tumour diversity.

Several factors, including the molecular properties of the tumour cell itself, the strength of the cell-cell interaction, as well as the density and stiffness of the ECM, may play a role in influencing the mode by which HGG cells migrate (Kumar et al. [2016], Ryan et al. [2001], Wu et al. [2021]). To better understand this interaction, the following section examines the influence of the substrate stiffness on single-cell emigration.

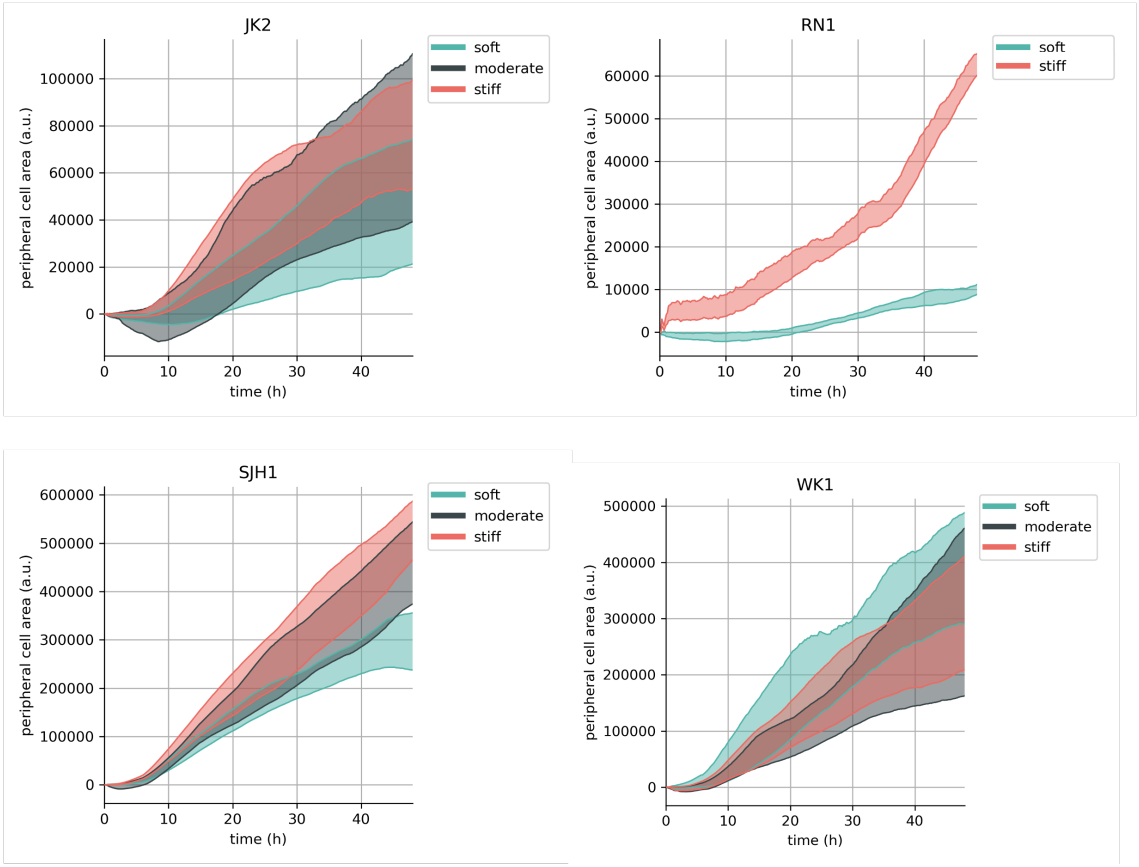

Figure 3.5: **Single-Cell Emigration of HGG Cells from a Spheroid is Differentially Regulated by Substrate Stiffness**

Collective area of cells undergoing single-cell emigration in the periphery zone over time for each cell line. Data is presented as pooled data with soft= 0.2, 0.5, 1 kPa; moderate = 2, 4, 8 kPa; and stiff = 12, 25, 50 kPa. Shaded area indicates SEM. Total number of replicates analysed for each cell line (soft, moderate and stiff); JK2 (18, 12, 12), RN1 (3, 0, 2), SJH1(21, 22, 23), and WK1 (7, 5, 9). Replicates in which the cells contacted the well wall and/or could not be segmented due to technical reasons were excluded from analysis.

3.2.1 Stiffer Substrates Increase Single-Cell Emigration

The effect of substrate stiffness on single cell emigration was evaluated over a 48-hour time period with images every 10 minutes, as described in Chapter 2. Data (Figure 3.5) show that single cells emigrate continuously during the time period observed for all cell lines.

The maximum collective area of cells undergoing single-cell emigration is shown in Figure 3.5. Except for the WK1 cells, data suggest that with increasing substrate stiffness, there is a tendency for greater single-cell emigration (Figure 3.5). From these observations, it can be concluded that JK2, RN1, and SJH1 cell lines exhibit single-cell emigration that is sensitive to substrate stiffness. Conversely, the WK1 cell line displays a unique biphasic behaviour with notably high levels of single-cell emigration observed on both the softest and stiffest substrates, and the lowest emigration on substrates of moderate stiffness. Therefore, WK1's emigration from the spheroid is also categorised as stiffness-sensitive. (Table 3.2). The findings reported align with earlier research by Grundy et al., which examined the stiffness characteristics of JK2 and RN1 cells as they migrate individually. Nonetheless, these findings differ from the earlier results concerning SJH1 and WK1 cells (Grundy et al. [2016]). In the prior study, SJH1 cells were identified as being unaffected by stiffness, and WK1 cells showed minimal individual cell movement on soft substrates. This contrasts with the individual cell emigration behaviours established for these cell lines in the current study. To explore the origins of these variations, the role of cell-cell interactions in collective emigration was subsequently investigated.

Cell Line	Influence of Substrate on Morphology	Behaviour in Single-Cell Emigration
JK2 (Proneural)	Stiffness- Sensitive	Stiffness- Sensitive
RN1 (Mesenchymal)	Stiffness- Sensitive	Stiffness- Sensitive
SJH1 (Proneural)	Stiffness- Sensitive	Stiffness- Sensitive
WK1 (Classical)	Stiffness- Insensitive	Stiffness- Sensitive

Table 3.2: **Comparison of Morphology and Emigration of HGG Cells During Single- Cell Emigration on Soft and Stiff Substrates**

3.3 Collective-Cell Emigration

GBM cells are able to migrate either individually or as groups (Garcia-Diaz et al. [2023], Gritsenko et al. [2017], Pillai and Franze [2024]). It is proposed that the mode of migration for GBM cells is influenced by alterations in the mechanical microenvironment surrounding the cells (Friedl et al. [2012], Gritsenko et al. [2017], Grundy et al. [2016], Volovetz et al. [2020]). Although the role of collective migration in cancer invasiveness is recognised, much of our understanding of this process originates from research in normal developmental biology (Volovetz et al. [2020]). In the following section, we examine the collective emigration of HGG cells from spheroids to understand how cell-substrate and cell-cell interactions affect emigration patterns. For the SJH1 and WK1 cell lines, the spheroid boundaries became challenging to distinguish as large numbers of HGG cells emigrated, resulting in an indistinct boundary between the spheroid core and the migrating edge (Figure 3.2). To address this issue, the calculated area of collective emigration for all cell lines included the spheroid.

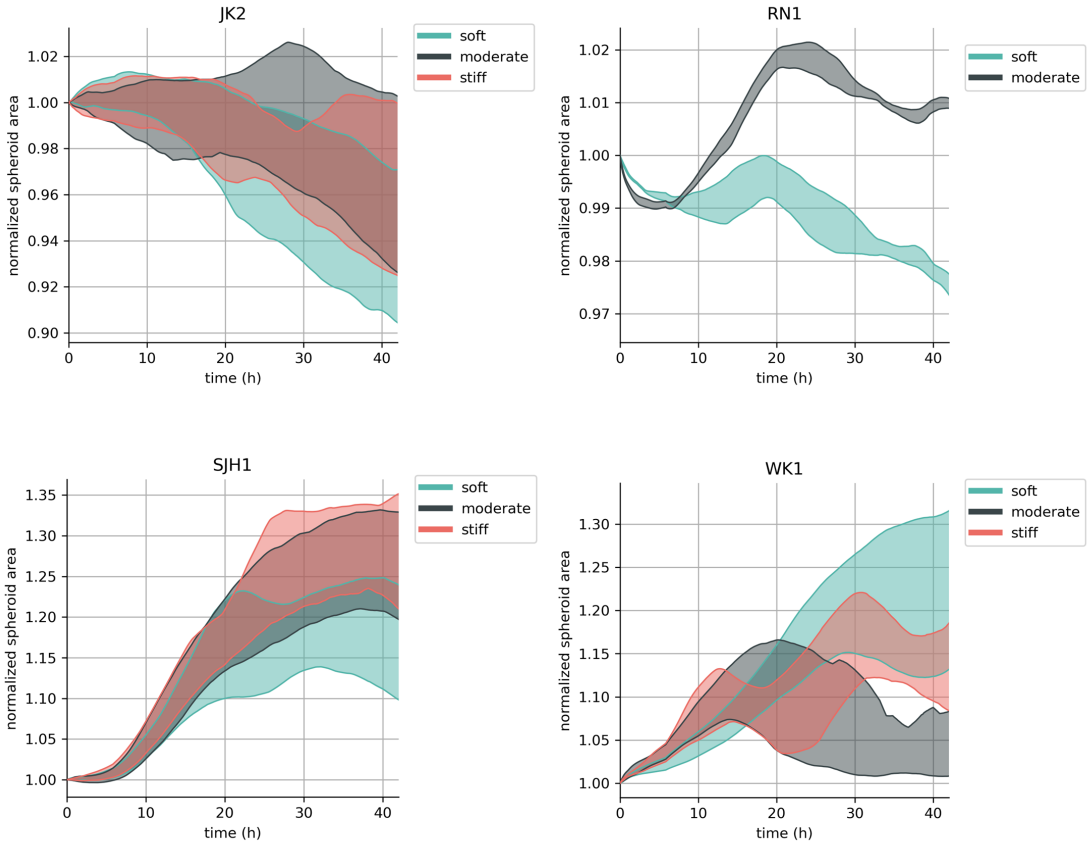

Figure 3.6: **Collective Emigration of HGG Cells is a Dynamic Process**

Area of cells undergoing collective emigration over time for each cell line. Area presented is normalised to the area of the spheroid at time=0 min. Data is presented as pooled data with soft= 0.2, 0.5, 1 kPa; moderate = 2, 4, 8 kPa; and stiff = 12, 25, 50 kPa. Shaded area indicates SEM.

3.3.1 The Area of Collective-Cell Emigration from the Spheroid is Dynamic

During collective emigration, cells remain connected to each other as they migrate across the substrate. Certain HGG cells that are rapidly moving detach from the cohesive sheet of collective migration and move individually (Figure 3.1). Therefore, the extent of the entire emigration sheet is affected by the quantity of HGG cells that depart from the spheroid and join the collective emigration area, as well as those that detach from the emigration sheet to proceed with single-cell migration.

For SJH1 cells, the area of collective emigration seems to be affected by substrate stiffness (Figure 3.7), with greater emigration rates recorded on stiffer substrates during the initial 8 hours. Over this period, the area of collective emigration grows as HGG cells depart from the core of the spheroid on PAHG (Figure 3.6). During the last 8 hours of observation, the emigrating area shrinks. This expansion and contraction pattern indicates a bimodal distribution of collective emigration concerning the substrate stiffness.

In the case of the WK1 cell line, the area of collective emigration initially expands within the first 8 hours across all tested substrate stiffness (Figure 3.6 & 3.7). However, unlike what is observed with the SJH1 cell line, there is no clear trend of a consistent increase with substrate stiffness. Rather, the rate of expansion in collective emigration during these initial 8 hours seems to follow a bimodal pattern. During the subsequent 8 hours of observation, no correlation with substrate stiffness is evident (Figure 3.7).

Although the RN1, SJH1, and WK1 cell lines show increased collective emigration during the first 8 hours, by contrast, this area contracts for the JK2 cell line (Figure 3.6).

This is most pronounced in the moderate substrate stiffness (8-12 kPa) (Figure 3.7). This suggests an ongoing contraction of the spheroid. The absolute value of the rate of change in collective emigration is lower in the RN1 cell line, and there is no observed relationship between this rate and the substrate's stiffness (Figure 3.7).

3.3.2 Substrate Stiffness Influences the Proportion of Collective Emigration

To further evaluate the expansion and contraction of the collective emigration area, the data were fitted with both a linear regression model and a switch-point model, which is a combination of two connected straight lines with opposing slopes. Data from the switch-point model were used when the collective emigration area demonstrated a bimodal behaviour, and data from the linear regression model were used when no such behaviour was observed (Figure 3.8). Specifically, the switch-point model was used instead of the linear regression model when the resulting deviation of the data from the switch-point model was at least 50% smaller than with the linear regression model. This approach (Figure 3.8) had the advantage over blunt segmentation of the data into the first and last 8 hours of the assay (Figure 3.7), as it allowed the nuances in cell behaviour to be explored, to determine when (as measured by the 'changepoint time') and if (as measured by the 'changepoint fraction') the collective area of emigration exhibited a bimodal behaviour. For RN1, SJH1, and WK1 cell lines, there was an initial expansion of the area of collective emigration (Figure 3.6 & 3.7). In some cases, this expansion was not sustained, and the area of collective emigration retracted. This is represented by a greater changepoint fraction in these three cell lines (Figure 3.8) compared to JK2 cells which showed an

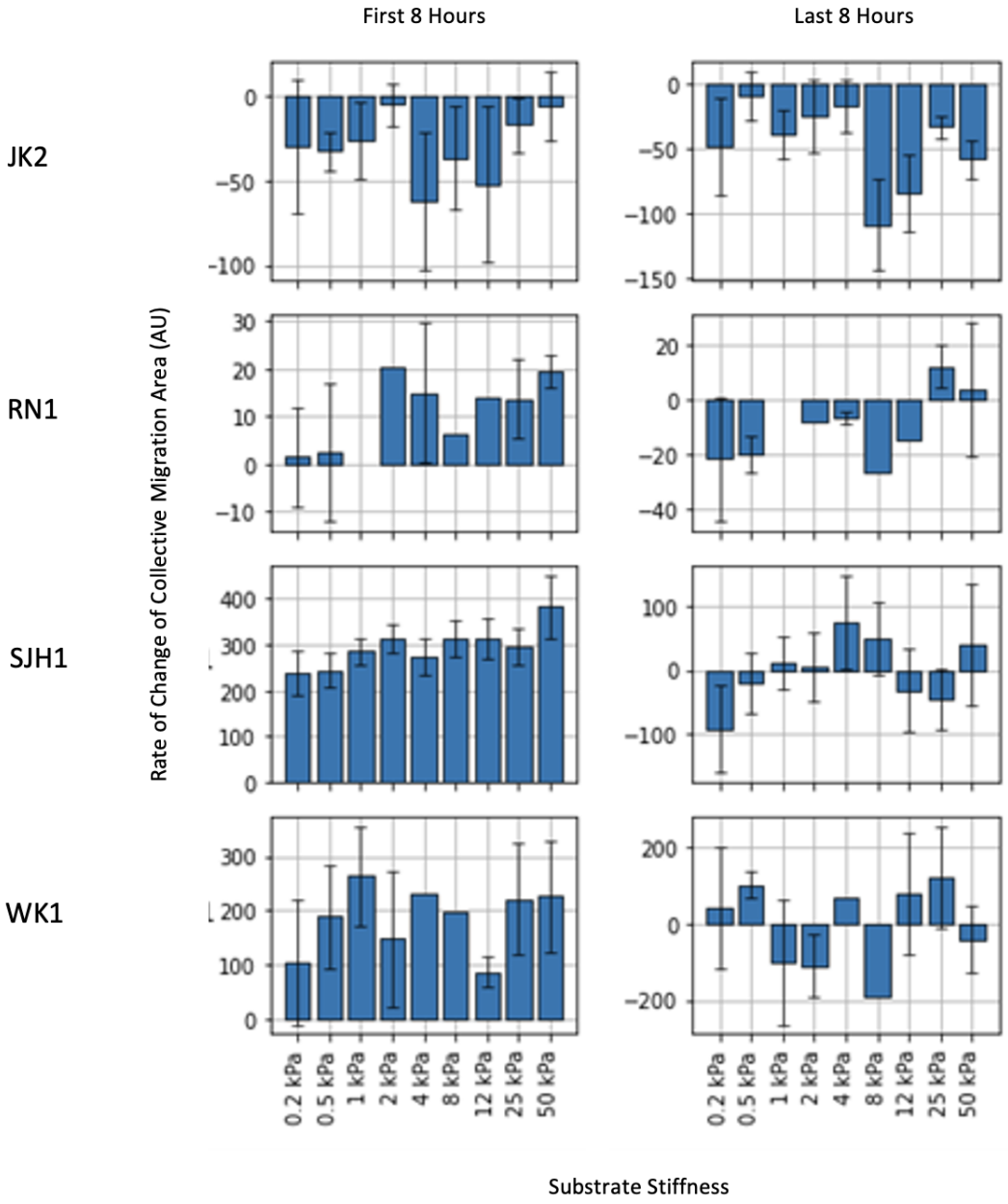

Figure 3.7: **Rate of Change in Collective Emigration Area**

The rate of change in the collective area of emigration was divided into the first 8 and last 8 hours for each cell line for each substrate stiffness examined. Error bars indicate SEM. Total number of replicates for each cell line; JK2 (64), RN1 (14), SJH1 (93), WK1 (25)

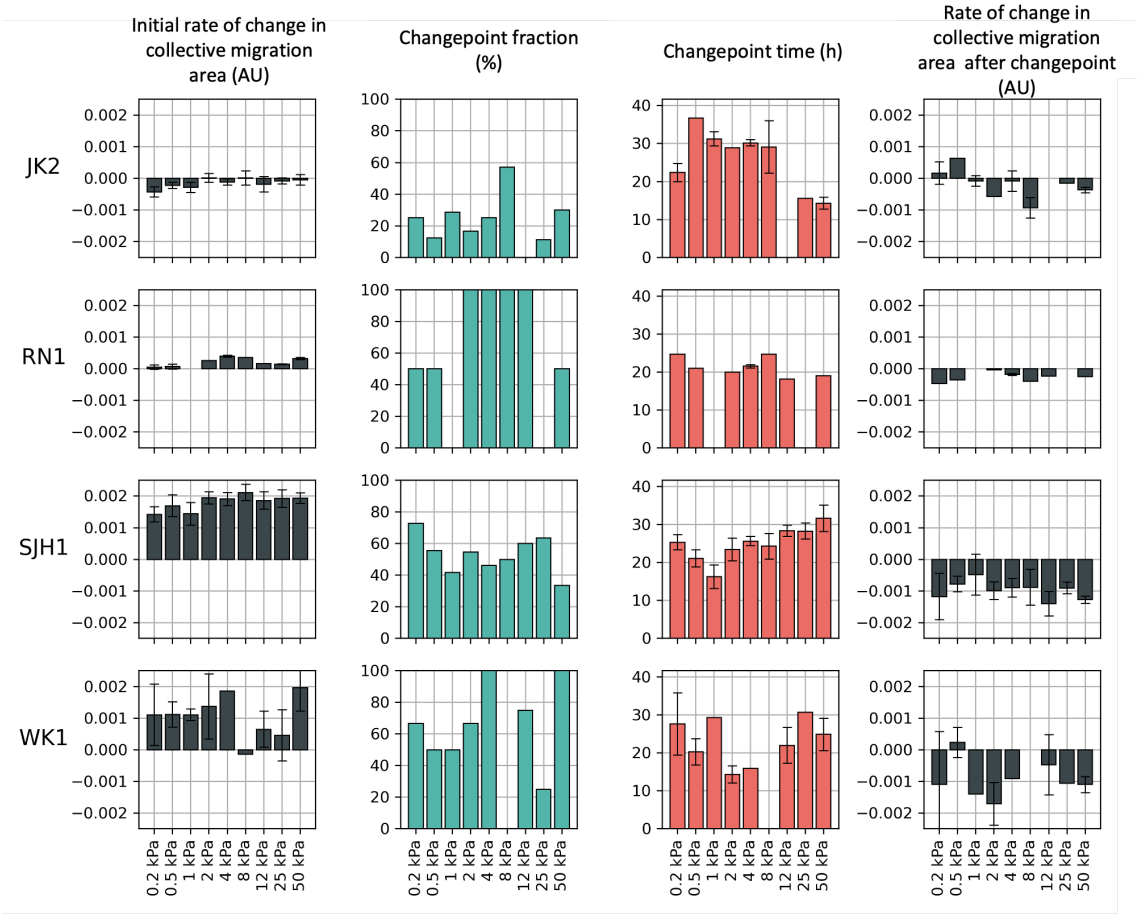

Figure 3.8: **Switch-Point Analysis**

A linear regression model or a switch point model was applied to measure the change in the area of collective-cell emigration over time. The slope from the linear regression or the slope of the initial segment in the switch point model indicates the initial rate of change in area. The changepoint fraction indicates the proportion of replicates where a switch point model was necessary for fitting each cell line on different substrate stiffnesses. The changepoint time is the moment when the two line segments with different slopes meet in the switch point model. The rate of change in the emigration area following the changepoint corresponds to the slope of the second segment of the switch point model. Error bars display SEM. The total number of replicates for each cell line is as follows: JK2 (64), RN1 (14), SJH1 (93), WK1 (25)

ongoing contraction of spheroid.

The magnitude of the difference in the rate of change in collective emigration before and after the changepoint time is greater for the SHJ1 and WK1 cells, compared to the minimal difference observed for the JK2 and RN1 cells (Figure 3.8). For SJH1 and JK2 cells, the initial rate of change appears to be influenced by the stiffness of the substrate (Figure 3.8) with higher rates on the stiffer substrates. Similarly, for SJH1 cells, the changepoint fraction appears to be influenced by the stiffness of the substrate (Figure 3.7) with lower percentages on the stiffer substrates, suggesting increased collective emigration on the stiffer substrates.

For the JK2 cell line, bimodal behaviour emerged only under specific conditions, where collective emigration was delayed on substrates of moderate stiffness and accelerated on both the softest and the firmest substrates. Similarly, SJH1 and WK1 cells showed an influence of the substrate: "switching" occurred sooner on moderately stiff substrates and later on on the softest and firmest substrates.

Together, the data suggest that the GBM lines analysed exhibit collective mechanosensitive emigration.

Cell Line	Behaviour in Single-Cell Emigration	Behaviour in Collective Emigration
JK2 (Proneural)	Stiffness- Sensitive	Stiffness- Sensitive
RN1 (Mesenchyma)	Stiffness- Sensitive	Stiffness- Sensitive
SJH1 (Proneural)	Stiffness- Sensitive	Stiffness- Sensitive
WK1 (Classical)	Stiffness- Sensitive	Stiffness- Sensitive

Table 3.3: **Behaviour of HGG cells during Single-Cell and Collective Emigration**

3.4 Focal Adhesions May Be Implicated In Mechanosensitive Behaviour

Utilising normalised RNA-sequencing data obtained at the time of establishment of cell culture, from the publicly accessible Q-Cell resource (D'Souza et al. [2020]), and with the guidance of Dr Christoph Mark, an *in-silico* pathway analysis was conducted to pinpoint differentially expressed genes and associated molecular pathways that might explain the distinct behaviours of GBM cell lines observed (Table 3.3). Comprehensive details, including patient demographics for the cell lines, are available on the Q-Cell (https://www.qimrb.edu.au/qcell) website.

3.4.1 Cell-lines Differ in the Fraction of Differentially Expressed Genes using RNA-Sequencing

For each of the 12 cell lines in the Q-Cell database (including the WK1, RN1, SJH1, and JK2 lines utilised in this thesis), differentially expressed genes were detected using a one-sample t-test (Figure 3.9). Genes were considered significantly upregulated or downregulated if their expression levels varied by more than 2-fold from the average across all cell lines and had an adjusted p-value of less than 0.05 (Figure 3.10). This analysis showed that among the four cell lines examined, the SJH1 line exhibited the highest percentage of differentially expressed genes, while the JK2 line had the lowest percentage (Figure 3.9).

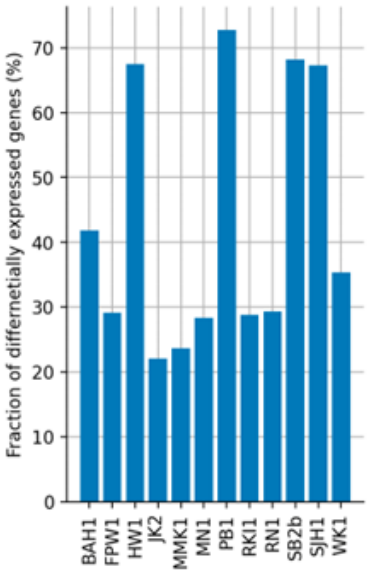

Figure 3.9: **Percentage of Differentially Expressed Genes in Cell Lines from the Q-Cell Database**

Differentially expressed genes were identified from the 12 cell lines listed in the Q-Cell RNA sequencing database using a one-sample t-test. Differentially expressed genes for a particular cell line were defined as genes that deviated in expression by more than 2-fold compared to the mean of the remaining cell lines and an adjusted p-value <0.05.

3.4.2 Association of Differentially Expressed Genes with Emigration Pattern

Next, gene set enrichment analysis (GSEA) was performed (Subramanian et al. [2005]). The GSEApy package (Fang et al. [2023]), which uses the Enrichr tool for over-representation analysis (Chen et al. [2013a]) was employed to analyse the genes identified above in section 3.4.1. GSEA is a statistical method used to query whether a gene expression pattern seen in a test sample overlaps with a similar one previously found in other cell types, disease conditions, or treatment responses (Fang et al. [2023]). The gene set library used in this analysis was derived from The Gene Ontology Consortium (The Gene Ontology Consortium [2019]). Enrichr uses several ranking methods to determine enrichment. In this analysis, the combined score (CS) was used to determine the genetic pathways of the cellular components are be enriched for the cell lines SJH1, JK2, WK1, and RN1. The

CS is calculated by multiplying the odds ratio with the negative natural logarithm of the p-value. The p-value is determined via Fisher's exact test, assuming the independence of each gene (Xie et al. [2021]).

GSEA analysis (Figure 3.10) showed that no gene sets were enriched for the JK2 cell line, while the RN1 cell line revealed two enriched gene sets. This suggests that the differentially expressed genes in these cell lines are not associated with any known molecular pathway in the studied gene set library (The Gene Ontology Consortium [2019]). In contrast, GSEA indicated enrichment across several cellular pathways for WK1 and SJH1 cells, with significant enrichment in pathways such as focal adhesions (GO0005925) and cell-substrate junction (GO0030055) (The Gene Ontology Consortium [2019]), as depicted in Figure 3.10. This enrichment may potentially shed light on the cell behaviours observed in this study (Table 3.3).

3.5 Chapter Discussion:Cells Act Differently When They Socialise as A Group

The invasive nature of GBM cells contributes significantly to resistance to therapy, often leading to tumour regrowth from cells that have invaded beyond the surgical margins (Cuddapah et al. [2014], Garcia-Diaz et al. [2023], Gupta et al. [2024]). Traditional 2D culture assays do not fully capture the dynamics of GBM cell adhesion and the collective migration process, which are crucial for invasion (Haeger et al. [2015], Wu et al. [2021]). Research shows that GBM cells can invade 3D scaffolds and brain tissues

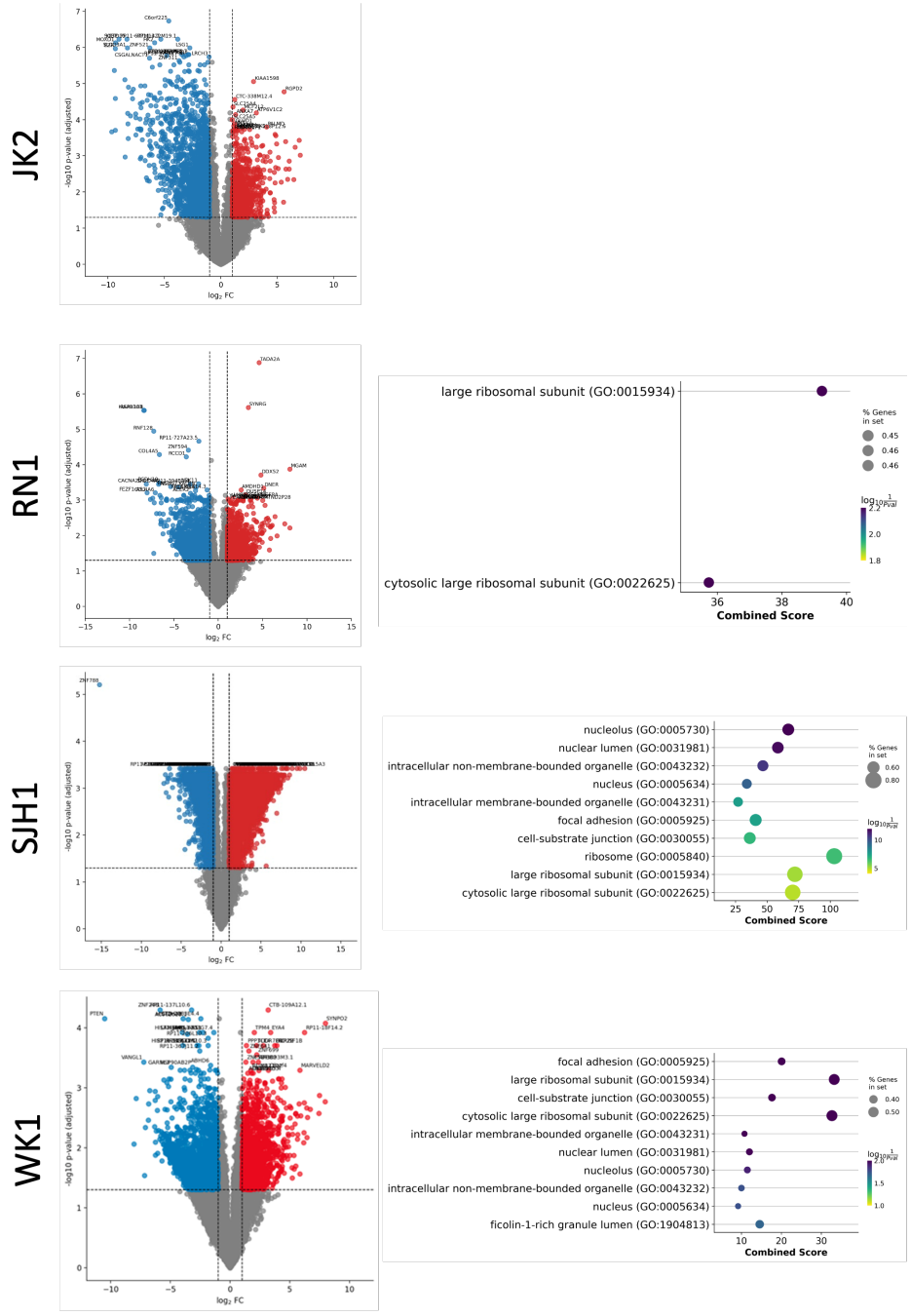

Figure 3.10: **Gene Set Enrichment Analysis of Differentially Expressed Genes in Cell Lines from the Q-Cell Database**

Differentially expressed genes were identified from the 12 cell lines listed in the Q-Cell RNA sequencing database using a one-sample t-test. Differentially expressed genes for a particular cell line were defined as genes that deviated in expression by more than 2-fold compared to the mean of the remaining cell lines and an adjusted p-value <0.05. Volcano plots (Left hand side of figure) display increased (Red) and decreased (Blue) genes. Gene set enrichment analysis (GSEA), using the GSEApy package which uses the Enrichr tool for over-representation analysis was used to analyse differentially expressed genes identified. The Gene Ontology Consortium gene library was used (The Gene Ontology Consortium [2019]). Enrichr uses several ranking methods to determine enrichment. In this analysis, the combined score (CS) was used to determine the genetic pathways of the cellular components that were enriched for the cell lines SJH1, JK2, WK1, and RN1 (right hand side of figure).

both individually and collectively, maintaining cell-cell connections during this process (Gritsenko et al. [2017]). This collective migration is significant, as GBM cells invade along blood vessels, the neuroaxis and the astrocyte-rich brain parenchyma (Bordignon et al. [2006], Cuddapah et al. [2014], Farin et al. [2006], Gritsenko et al. [2017], Volovetz et al. [2020], Winkler et al. [2009]). Studies involving embedded spheroids in collagen highlight a tendency for collective migration (Grundy et al. [2016]), and multicellular networks observed in mouse models are associated with GBM invasion (Osswald et al. [2015]). GBM cells respond to mechanical environmental signals via focal adhesions, in a process known as mechanosensation (Burridge et al. [1988], Sarker et al. [2020]).

Previous work in the host lab has shown the influence of the mechanical environment on single-cell GBM migration (Bradbury et al. [2017], Grundy et al. [2016]). Similarly, it has been postulated that these differing mechanosensitive behaviours could be subclass-specific (Grundy et al. [2016], Mair et al. [2018]). The results in this chapter build on this and highlight sub-type and cell-line-specific changes in emigration patterns in response to different substrate stiffness in both single-cell and collective emigration between patient-derived primary GBM cell lines in a 3D spheroid plated on predefined mechanically tunable PAHGs. The 2D analysis of cell emigration from the 3D spheroid facilitated the comparison between cells emigrating individually and those undergoing collective movement. This emigration was influenced by interactions between cells as well as between cells and the substrate. The use of 2D analyses, rather than 3D analyses with an embedded spheroid model, provided stronger experimental control due to the confinement of emigration to a single plane. Moreover, although 3D embedded spheroid

analysis protocols are well-established, they face challenges due to the need for significant computer memory, the time-intensive nature of the process, and the difficulty in guaranteeing accurate cell segmentation at each stage of processing (Blacher et al. [2014]). The experimental setup used in this chapter enabled a straightforward comparison of results with previously published studies on cancer cell emigration, the majority of which were conducted using 2D models (Grundy et al. [2016], Nunes et al. [2019], Ryan et al. [2001], Wu et al. [2021]).

3.5.1 The Influence of The Mechanical Environment on Morphology and Emigration of HGG Cells

When spheroids were seeded on hydrogels, very few JK2 and RN1 cells emigrated, while many WK1 and SJH1 emigrated onto the hydrogels (Figure 3.2 & 3.5). The large emigration of cells of the classical subtype and the poor emigration of cells of the mesenchymal type are consistent with previous reports of 2D cell culture (Rosén et al. [2023]), however, both JK2 and SJH1 cells are classified as proneural subtype and demonstrate differing behaviours. It has previously been postulated that migration of the proneural subtype may be rigidity independent, mirroring the rigidity-independent manner by which neurones branch (Mair et al. [2018]), however, this was not observed in this thesis.

These observations might indicate variations in the comparative strengths of cell-cell versus cell-substrate interactions. When cell-cell interactions are more robust than cell-substrate interactions, they promote the retention of HGG cells within spheroids. In

contrast, if cell-substrate interactions prevail, exceeding cell-cell interactions, they may drive HGG cells to migrate from the spheroid (Nath and Devi [2016], Ryan et al. [2001]).

Individual cells have been suggested to use at least two main modes of emigration, amoeboid and mesenchymal, and these two modes are characterised by differences in morphology and adhesion to the underlying substrate (Lintz et al. [2017]). Amoeboid emigration is characterised by rounded cell bodies, weak adhesions to the ECM, and rapid motility. In contrast, mesenchymal emigration is characterised by cell polarisation with a leading and trailing edge and strong stress fibres (Bell et al. [2019], Friedl et al. [2012], Friedl and Wolf [2003], Liu et al. [2015], Panková et al. [2010]). On soft substrates, both JK2 and RN1 cell lines exhibited rounded cell bodies, whereas the SJH1 and WK1 cells displayed spindle-shaped morphologies. On substrates with greater stiffness, all cell lines tended to have more spindle-shaped morphologies, along with a general increase in the number of emigrating cells (see Figure 3.2 and 3.5). These findings help to establish the stiffness-sensitive morphological characteristics of the JK2, RN1, and SJH1 cell lines, as well as the stiffness-insensitive morphological characteristics of the WK1 cells (refer to Table 3.1).

Interestingly, it has been previously reported that WK1 HGG cells show a rounded morphology, similar to the JK2 cell line, when seeded as single cells on soft substrates. This differs from what is noted in section 3.1.3 and figure 3.2, which indicates that emigrated WK1 cells exhibit a spindle-shaped morphology on the soft PAHG. The potential explanation for this phenomenon might be modified mechanosensing arising from interactions among cells within the spheroid before they emerge from the spheroid onto the

PAHGs. Alternatively, cell-cell interactions in the spheroids alongside cell-substrate interactions might exert selective pressure, influencing which cells emerge from the spheroid. In scenarios where cells are plated sparsely to ensure isolated individual cells (Grundy et al. [2016]), cells do not experience such pressures. In this case, regulation of cell migration and morphology depends solely on adhesion to the underlying matrix. In contrast, in spheroid cultures, only cells with robust cell-substrate interactions, often indicated by a spindle-shaped morphology, might manage to exit the spheroid. This could explain the prevalent spindle-shaped morphology observed on PAHG (Figure 3.2) (Friedl et al. [2012], Lu et al. [2015], Nath and Devi [2016], Panková et al. [2010], Ryan et al. [2001]).

A well-established mathematical framework for describing cell migration is based on the motor-clutch mechanism (Case and Waterman [2015], Elosegui-Artola et al. [2018]). Within this model, F-actin filaments polymerise at the plasma membrane, advancing the cell's leading edge. Simultaneously, these filaments are withdrawn from the trailing edge by ATP-dependent myosin II, which functions as molecular "motors", and are also propelled by the forces generated from ATP-driven polymerisation. To mitigate retrograde F-actin flow, mechanical linkages, frequently integrin-mediated adhesions, are established between F-actin and the ECM. These "clutches" generate traction and direct cellular movement toward areas exhibiting increased adhesion (Case and Waterman [2015], Elosegui-Artola et al. [2018], Isomursu et al. [2022]). Figure 3.5 shows a positive correlation between individual cell emigration and substrate stiffness in all lines tested, indicating that single-cell and group emigration are mechanosensitive in these cell lines.

Recent research indicates that differences in internal contractility and cell adhesion to the ECM may elucidate why certain cells exhibit a stronger tendency toward durotaxis while others show adurotaxis (Isomursu et al. [2022], Yeoman et al. [2021]). In addition, cellular traction forces have been shown to maximise on substrates with a particular "optimal stiffness", which can be predicted using the motor–clutch model (Elosegui-Artola et al. [2018], Isomursu et al. [2022]). This might explain why the WK1 cell line displays distinct biphasic behaviour, with notably high levels of single-cell emigration on both the softest and stiffest substrates, but reduced emigration on substrates with intermediate stiffness (Figure 3.5). Similarly, JK2 cells exhibit a biphasic response to increased substrate stiffness, generally showing a decrease in roundness with greater stiffness, except for those on a 1 kPa substrate (Figure 3.4).

The lack of notable single cell migration in RN1 cell spheroids (Figure 3.3) implies that RN1 cells exhibit strong cell-cell adhesion. These interactions are expected to hinder the initial movement of HGG cells away from the spheroid (Friedl et al. [2012], Nath and Devi [2016], Ryan et al. [2001], Wu et al. [2021]). This hypothesis is further supported by the observation that the RN1 spheroids at $t = 0$ were the smallest among the cell lines studied (Figure 3.3), although future research should examine the contribution of apoptosis to spheroid compaction. Despite this, this finding could indicate a subclass-specific behaviour, as mesenchymal GBM cells show limited migration in 2D culture compared to the classical subtype (Rosén et al. [2023]).

Spheroid models offers the benefit of replicating collective emigration processes in a manner that more accurately mirrors *in-vivo* conditions (Ahmed [2023], Friedl et al.

[2012], Haeger et al. [2015], Wu et al. [2021]). The analyses carried out in this study lead to the conclusion that each investigated cell line shows mechanosensitive collective emigration (Figure 3.6, 3.7 & 3.8). It seems that mechanosensitivity observed in single-cell emigration is preserved in the context of collective-cell emigration; however, the straightforward relationship noted between substrate stiffness and behaviours in single-cell emigration becomes more intricate in the case of collective-cell emigration. Notably, the WK1 cell line, which exhibited mechano-insensitive morphological traits in single-cell emigration, intriguingly exhibits mechano-sensitive behaviour during collective emigration (Table 3.3).

This suggests that complex interplay between cell-cell and cell-substrate interactions that direct GBM emigration. In fact, a great body of work has been published detailing the role of cell-cell interactions, as well as interactions of HGG cells with their surroundings during emigration (Demuth and Berens [2004], Eikenberry et al. [2009], Haeger et al. [2015]). However, it is unclear why certain cells stay within the spheroid, some persist in migrating collectively, and others opt for single-cell movement. These variations might indicate heterogeneity within the spheroid that mechanical factors and GBM subtyping alone cannot explain (Patel et al. [2014]).

3.5.2 Genetic Basis for Mechanosensation

To better understand the potential genetic basis of the behaviours observed in this study, publicly accessible RNA sequencing datasets were examined. These sequences were performed after cell culture establishment. GSEA analysis pointed to the enrichment

of gene sets associated with FAs for both WK1 and SJH1 cell lines. Cells leverage FAs to respond to mechanical signals in their environment. The components of FAs includes elements that mediate cellular functions, such as kinases, GTPases, phosphatases, proteases, and lipases, and FAs have roles in several cellular pathways (Wozniak et al. [2004]). In their 2D cell culture experiments, Liu et al. demonstrated that mesenchymal cells, when experiencing high levels of confinement and minimal adhesion to the underlying substrate, can transition to an amoeboid migration phenotype. This transition is facilitated by the deformation of the cell nucleus, leading to stretching of the nuclear envelope and subsequently activating cell contractility pathways (Lomakin et al. [2020]). Although the model used in this thesis does not replicate conditions of confinement once cells leave the spheroid, it was observed that the mesenchymal RN1 cells demonstrate a rounded amoeboid morphology on soft substrates. Ulrich et al. revealed that commercially sourced HGG cells, when plated as individual cells on mechanically adaptable PAHG, show elongated FAs on stiff substrates and disbanded FAs on soft substrates (Ulrich et al. [2009]). WK1 and SJH1 exhibited distinct mechanical sensitivities in morphology, single-cell migration, and collective migration (Table 3.2 & Table 3.3). This indicates a possible pathway mediated by FAs that modulates the mechanical responsiveness of cell lines in both single-cell and collective migration scenarios (Bershadsky et al. [2006]).

It is important to acknowledge that the RNA sequencing data used in this study were obtained after cell culture was established from HGG cells subjected to different experimental conditions than those utilised here (resource available at https://www.qimrb.edu.au/qcell (D'Souza et al. [2020]). Consequently, the RNA sequencing data may not precisely

represent the RNA transcription by HGG cells under the experimental conditions applied in this study, with alterations in RNA transcription induced by substrate rigidity having been previously reported (Darnell et al. [2018], Wolfram et al. [2024]).

3.5.3 Considerations of Using a Canny Edge Detection tool to measure the Collective Area of Single-Cell Emigration

The area of single-cell emigration was segmented and then examined by Canny edge detection as previously described and therefore does not directly detect individual cells (Cisneros Castillo et al. [2016]). Despite this, it is intuitive that the more single-cells in an area, the higher the number of determined edges. The resultant binary image produced from edge detection reflects the perimeter of the individual cells, and it is the area of the binary image which is used as an alternative metric for the area of single-cell emigration. As such, the morphology of the cells themselves can affect this measurement. In section 3.1.3, it was noted that the JK2 and RN1 cell lines tend to exhibit a rounded shape on softer substrates; however, they adopt a spindle-like form on firmer substrates. Additionally, as substrate stiffness increases, cells tend to spread more on the stiffer surfaces. Consequently, the perimeter of each cell generally appears larger on harder substrates than on softer ones, which can lead to an overestimation of the calculated area for emigration.

To reduce the influence of extraneous elements (such as hydrogel impurities or shadows) present initially at $t = 0$, single-cell emigration areas are reported based on the increase in area from time $t = 0$. Although effective against extraneous structures,

these relative increase measurements fail to address camera noise and fluctuations in brightness gradients, which may create artificial edges during edge detection processing. To mitigate shadow effects, especially prominent near the well's perimeter, all time-lapse images underwent manual examination. Spheroid time-lapse images exhibiting significant brightness gradients were discarded. Future experiments might resolve these issues by using a nuclear stain compatible with live cell imaging to directly quantify the cells at the periphery.

3.6 Concluding Remarks

The analyses in this chapter used a 3D spheroid plated on mechanically tuned polyacrylamide hydrogels to assess the influence of substrate stiffness on the emigration of four primary patient-derived HGG cell lines. The use of spheroids and the analysis of the cells emerging from the spheroid allowed for the inference of not only the cell-substrate interactions that affect emigration but also the cell-cell interactions. The data presented suggested a complex interplay between these two interactions, potentially mediated by FA, independent of GBM subtype. It is necessary to investigate the hypothesis that, contrary to Friedl and Wolf's suggestion, the mode of emigration is not solely dictated by the comparative strengths of cell-cell versus cell-substrate interactions. Instead, it is the interplay and mutual influence of these interactions that ultimately shape the HGG migration.

Chapter 4

Relationship Between Spatial Arrangement of Glioblastoma Cells and Protein Expression

---

As reviewed in chapter 1, the brain parenchyma is a unique structure with a low Young's modulus (Budday et al. [2015], Butcher et al. [2009], Christ et al. [2010], Elkin et al. [2007], Taylor and Miller [2004]). Mechanically heterogeneous regions within the brain, like grey matter, white matter fibre tracts, and vasculature, create micro-environments that might influence glioblastoma multiforme (GBM) migration patterns (Budday et al. [2015], Hrapko et al. [2008], Scherer [1938]). Hans Joachim Scherer described glioma invasion into the brain from the main tumour, forming the 'Secondary Structures of Scherer,' which include peri-neuronal satellitosis, perivascular satellitosis, sub-pial spread, and invasion along the white matter tracts (Scherer [1938]).

In GBM, epidermal growth factor receptor (EGFR), a receptor tyrosine kinase, is frequently overexpressed and correlates with poorer survival (Furnari et al. [2007], Jones

and Holland [2011], Shinojima et al. [2003], Verhaak et al. [2010]). This mutation is frequently amplified in the classical subtype of GBM (Brennan et al. [2013], Chen et al. [2017b], Verhaak et al. [2010], Wang et al. [2017]). When EGFR is phosphorylated (p-EGFR), it enhances cell proliferation and invasion through phosphorylation of downstream signalling molecules phosphoinositide 3-kinase (PI3K) and protein kinase B (PKB or Akt) (Burgess et al. [2003], Sarker et al. [2020], Umesh et al. [2014]). Greater substrate stiffness in 2D cell cultures promotes the proliferation of high-grade glioma cells (HGG) and the expression of EGFR, Akt, and PI3K (Umesh et al. [2014]). On stiff, but not soft substrates, EGFR and focal adhesion (FA) markers co-localise, indicating that mechanical cues might cause EGFR clustering (Umesh et al. [2014]). Focal adhesion kinase (FAK), a non-receptor tyrosine kinase, links EGFR with the cell's mechanosensitive machinery. It is recruited to focal adhesions (FAs) upon integrin activation (Hao et al. [2013], Luu et al. [2024], Rea et al. [2013], Sieg et al. [2000]), and binds to EGFR, thereby and forming a mechanistic connection between the two (Kim et al. [2017], Nuñez et al. [2021], Rea et al. [2013], Sieg et al. [2000]). FAK's presence and its phosphorylation are especially notable in contexts of increased stiffness (Zhou et al. [2021]).

As such, this chapter aims to elucidate the spatial arrangement of EGFR and FAK signalling as a function of proximity to more stiff structures such as blood vessels in the otherwise soft brain parenchyma (Bellail et al. [2004], Reiter et al. [2023]). Formalin-fixed human xenografts in a whole brain slice mouse model were used with four primary patient-derived GBM cell lines. Archival tissue was used instead of newly created mouse models to address the 3Rs of animal research; replacement, reduction and refinement

(Russell [1995]). Multiple cell lines, representing the three molecular subtypes of GBM; classical (WK1), mesenchymal (RN1) and proneural (JK2 and SJH1); were used to determine the specific and independent behaviour of the cell line. EGFR and FAK phosphorylation levels were hypothesised to decrease with increasing distance from blood vessels, this gradient being more pronounced in the classical subtype, moderate in the mesenchymal subtype, and less apparent in the proneural subtype, reflecting a differential dependence on vascular-derived growth factors and extracellular matrix signalling among molecular subtypes (Brennan et al. [2013], Chen et al. [2017b], Verhaak et al. [2010], Wang et al. [2017]).

4.1 Thick Section Analysis Is Hampered By Auto-Fluorescence

The exploration of the spatial correlation between EGFR and FAK expression and phosphorylation and their proximity to stiffer structures such as blood vessels was attempted using thick 50 μm histological sections (Reiter et al. [2023]). The two predominant molecular techniques for detecting specific proteins in histological sections are immunohistochemistry (IHC) and immunofluorescence (IF) (Im et al. [2019], Magaki et al. [2019]). In IHC analysis, brightfield microscopy visualises a coloured chromogen, whereas, in IF, fluorescence microscopy helps to visualise a fluorochrome. IHC is advantageous for its durable signalling that does not degrade over time, allowing stained sections to be archived. However, the spatial precision of IHC is limited due to the chromogen being deposited through an enzyme-dependent reaction (Magaki et al. [2019]). In contrast, IF utilises fluorophores directly attached to a secondary antibody, enabling more detailed

localisation of target proteins and is frequently used for analysing co-localisation of protein expressions. Given the variety of fluorophores available, multiplex IF staining can be performed, detecting multiple proteins within a single histological sample (Im et al. [2019], Magaki et al. [2019], Taube et al. [2020]).

One benefit of using thicker sections, as illustrated in Figure 4.1, is the preservation of spatial details that are typically lost when employing the conventional thickness of 4-5μm.

Although thick sections offer certain benefits, they have not been commonly adopted in IF on formalin-fixed paraffin-embedded (FFPE) tissues by the scientific community for several reasons. These include the increased brittleness of thick sections during cutting compared to thin sections, the occurrence of photobleaching during imaging, and the limited penetration of antibodies in thicker sections (Ciani et al. [2023], Smart et al. [2023], Taqi et al. [2018]). Despite these established limitations, attempts were made to undertake staining of thick sections, to determine whether these limitations could be overcome, thus preserving important 3D tissue information.

4.1.1 Auto-fluorescence of FFPE Sections is a Hindrance to Multiplex IF

Significant levels of autofluorescence (AF) were observed (Figure 4.2) when thick sections were stained (Section 2.3) with a long multi-day incubation time. For this experiment, healthy mouse brain tissue was incubated for two days with a rabbit anti-CD31 antibody to identify blood vessels. Visualisation of CD-31 staining was performed using Alexa 568 anti-rabbit conjugated antibodies. IF imaging employed a 561 nm excitation laser, capturing detection spectra between 585 and 625 nm. A maximum projection of the

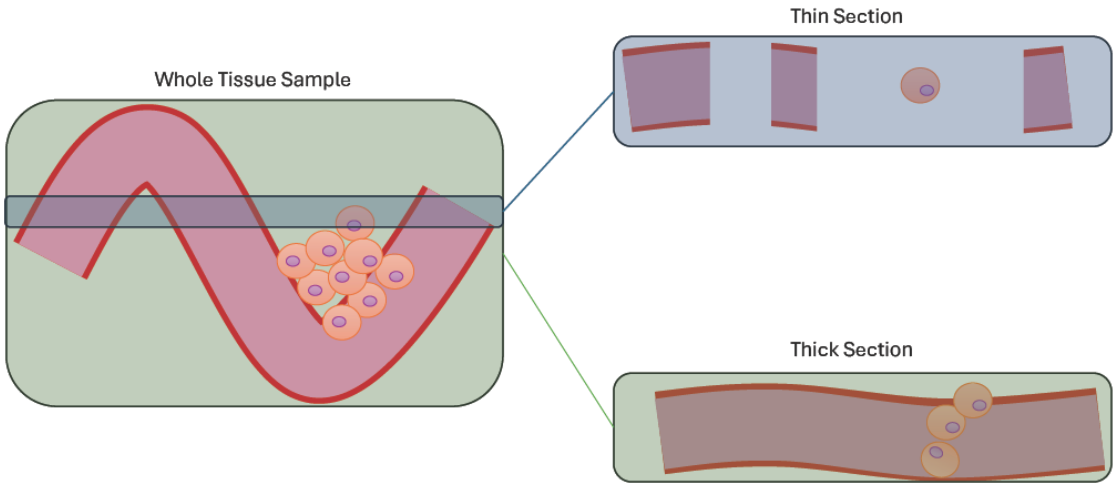

Figure 4.1: **Demonstration of Loss of Data with Thin Sections in Comparison to Thick Sections**
When tissues (left) are sectioned as thick sections (green box), there is a preservation of spatial data which would otherwise be lost when thin sections (blue box) are taken

Z-stack was generated using FIJI (ImageJ, Open Source).

AF has been reported to arise from many sources, including connective tissue components, cellular cytoplasmic contents, as well as fixatives and preservatives used to embed tissues (Davis et al. [2014]). Each substance possesses distinct excitation and emission spectra that, when observed across the whole tissue, can significantly impede imaging attempts of the sections. To investigate this further, spectral analysis was conducted on unstained, deparaffinised, and rehydrated sections of human colon and skin, mouse brain, and rat heart by collaborating PhD student Dr. Heeva Baharlou. Confocal microscopy was conducted using excitation laser lines at 405 nm, 473 nm, and 559 nm. Emission spectra were collected with a 20 nm bandpass filter, adjusted in 20 nm steps within the ranges of 415-795 nm, 490-790 nm, and 575-795 nm for each respective laser line. As

shown in Figure 4.2, the peak intensity of the emission spectra is significantly higher in the brain than in the tissues of the skin, colon, and heart. In addition, the emission profile of the unstained brain section spans a broader wavelength range compared to that of the skin, colon, and heart tissues (Baharlou [2022]), aligning with the widely used excitation/emission spectra in IF (Im et al. [2019]).

4.1.2 Sudan Black B Quenches Auto-Fluorescence in Thick FFPE Sections but Also Hinders Staining

Sudan Black B (SBB) is a lipophilic dye that has been shown to be useful in quenching AF in thin sections of frozen and FFPE tissues of the central nervous system, as well as in reducing the AF signal by 60-95% in pancreatic tissue (Erben et al. [2016], Oliveira et al. [2010]). To investigate whether similar results would be apparent in the application of this technique in thick histological sections, 60μm histological sections of normal mouse brain were treated with 0.1% SBB in 70% ethanol for one hour to quench AF (Oliveira et al. [2010]). Signal-to-noise ratio of confocal z-stack images of sections stained for CD31 with a conjugated Alexa 568 secondary antibody (Figure 4.4A) was used to determine whether SBB application was better used before antibody staining, after the antibody staining step, or not at all (Figure 4.3). An excitation laser at 561 nm was used and emission spectra were captured over 585-625 nm. To quantify the level of AF, mean pixel intensities were calculated from a region of interest, selected to avoid positive staining for CD31 for blood vessels (Figure 4.4B). Each of the images was acquired with identical microscope equipment and settings (see Table 2.1.4). In agreement with previous studies,

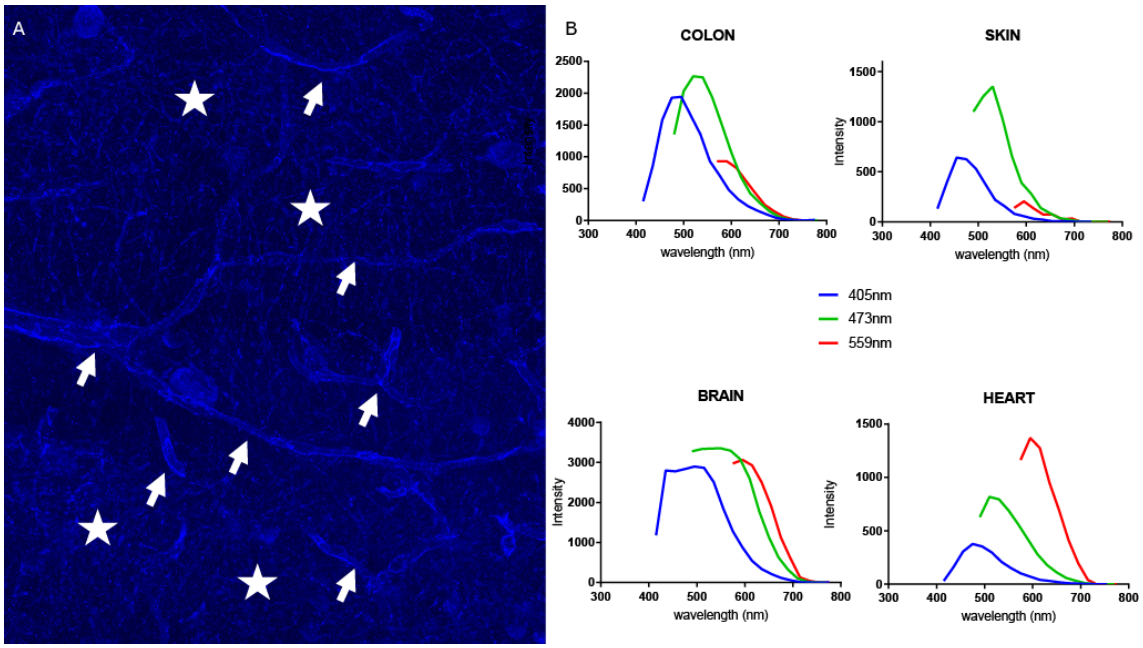

Figure 4.2: **Auto-fluorescence in FFPE Sections**

A) Maximal Z-projection of a thick section of normal mouse brain white matter stained with anti-CD31 antibody (Blue). Tubular structures are blood vessels (white arrows) which are positive for CD31. Speckled background represents noise from autofluorescence (AF) sources (white stars). **B)** Adapted from Baharlou [2022]. Tissue autofluorescence emission spectra following 405, 461 ad 568 nm laser excitation wavelengths. The intensity of pixels corresponding to AF structures measured at 20nm intervals upon excitation. Results are shown for a single image for each tissue type.

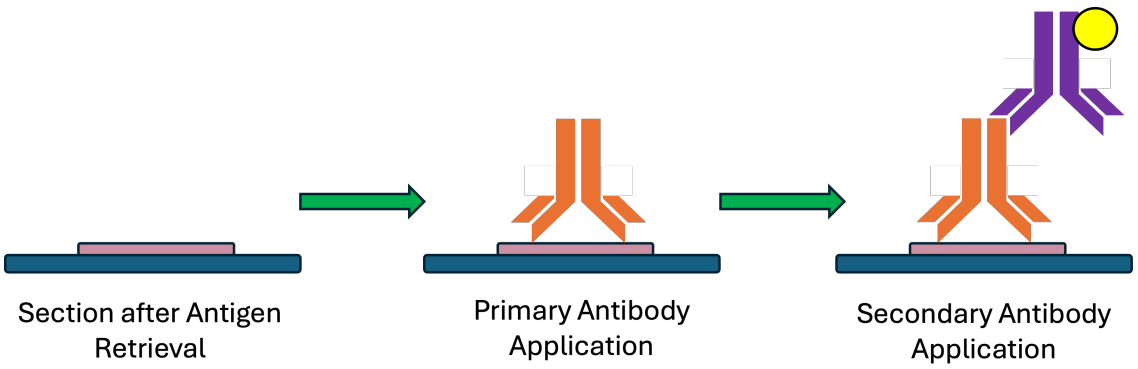

Figure 4.3: **Steps in Immunofluorescence**

SBB reduced the mean pixel intensity of sections when used after antibody staining (Oliveira et al. [2010]), however, background AF increased when SBB was used prior to antibody staining. Sections without SBB quenching had the best signal-to-noise ratio (Figure 4.4). Overall, the data revealed that SBB treatment did not improve the AF of the thick brain sections. Consequently, it was not possible to proceed with thick sections, but instead IF was next performed in thin histological sections of FFPE tissue.

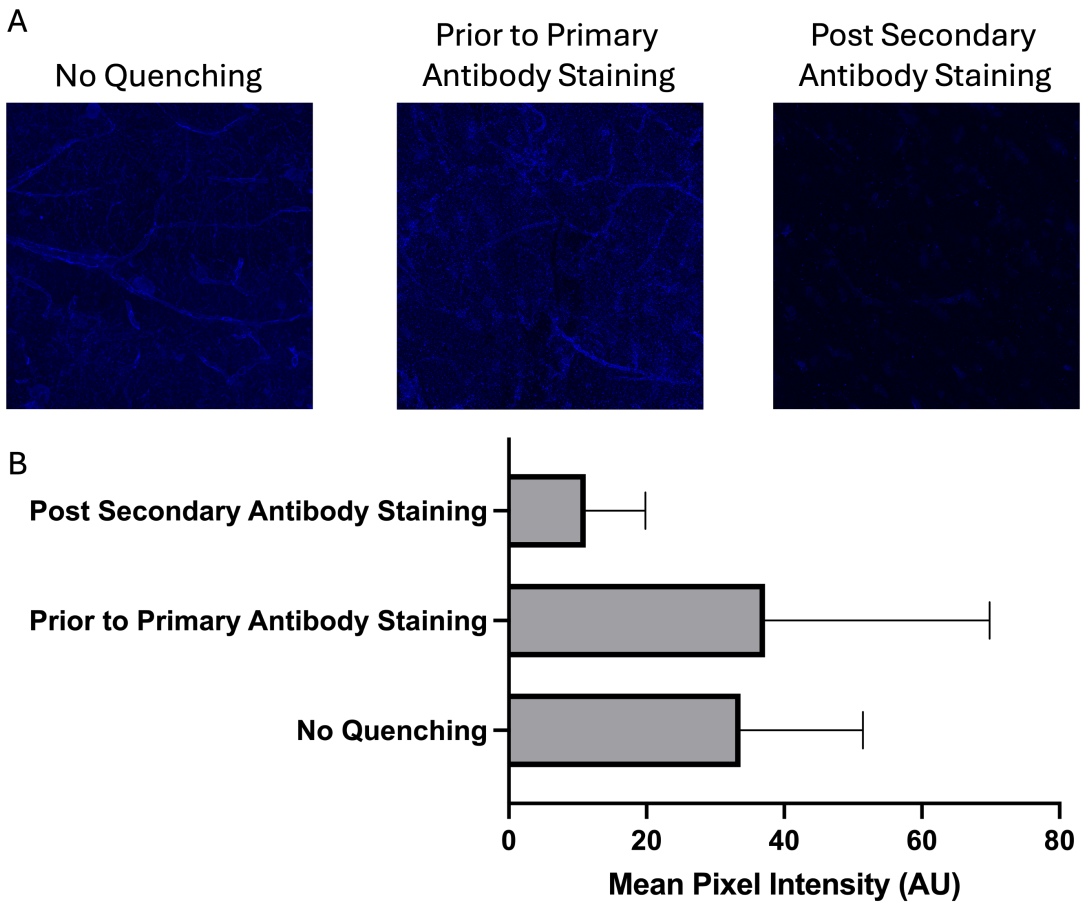

Figure 4.4: **Comparison of the Effect of Sudan Black B on Autofluorescence Quenching**

Sudan Black B (SBB) was applied to thick histological sections of normal mouse brain either prior to primary antibody staining, after secondary antibody incubation or not at all. **A)** Representation of a maximum projection of a z-stack through an imaged section. **B)** Mean pixel intensity was evaluated in a region of interest from images, excluding areas with positive blood vessel staining. N=1 for each condition. Data presented as Mean & SD

4.2 The Opal Staining Method

The OPAL staining method (PerkinElmer) is a powerful multiplex IF technique that uses individual tyramide signal amplification (TSA) to covalently deposit conjugated flurophores to detect various antigen targets (Parra et al. [2017], Willemsen et al. [2021]). Heat-induced epitope retrieval (HIER) is then used to remove the antibody after each cycle (Parra et al. [2017], Willemsen et al. [2021]). The OPAL (PerkinElmer) staining was first validated in uniplex staining and compared with traditional IHC.

4.2.1 IHC and Uniplex IF Validation

Uniplex IF and chromogenic IHC methods were employed to achieve comparable staining patterns, which were then evaluated against data from the publicly accessible Protein Atlas (proteinatlas.org) website (Sjöstedt et al. [2020], Thul et al. [2017], Uhlén et al. [2015], Uhlen et al. [2017]) (Table 4.1). EGFR and p-EGFR exhibited prominent membranous and cytoplasmic staining in decidual and trophoblastic cells within the human placenta, with minor staining observed in normal mouse brains, serving as positive and negative controls, respectively (Figure 4.5). FAK and p-FAK similarly showed intense cytoplasmic staining with moderate membranous staining in the same cell types within the human placenta, and minimal staining in human spleen sections, again used as positive and negative controls, respectively (Figure 4.9). Human leukocyte antigen class I (HLA) is present in all human nucleated cells and platelets, absent in cells from non-human species (Shiina et al. [2009]), making it an effective marker to identify human cells in

xenograft tissues (Allaway et al. [2016], D'Souza et al. [2020], Lee et al. [2019], Stringer et al. [2019]). HLA staining was confirmed using human spleen tissues, showing diffuse staining as a positive control, while the normal mouse brain, showing no staining, acted as a negative control (Figure 4.7). Tissue samples from mouse xenografts of human GBM cells were utilised to ensure the specificity of HLA staining (Figure 4.7). GLUT-1 is densely present in the endothelial lining of blood vessels, with staining verified by tubular structures in uniplex IF staining of mouse brain tissues (Figure 4.7) (Tang et al. [2017]). The anticipated and actual staining patterns are detailed in Table 4.1.

Table 4.1: **Staining patterns expected and seen in IHC and IF staining**

Protein	Tissue	Expected Staining	Staining seen in IHC	Staining seen in IF
EGFR	Human Placenta	Membranous>cytoplasmic staining in decidual and trophoblastic cells	Expected staining	Expected staining
	Mouse Brain	No staining	Non-specific background staining	No staining
	Human GBM (Xenograft)	Membranous and cytoplasmic staining	Not performed	Expected staining
p-EGFR	Human Placenta	Membranous>cytoplasmic staining in decidual and trophoblastic cells	Expected staining	Expected staining
	Mouse Brain	No staining	No staining	No staining
	Human GBM (Xenograft)	Membranous and cytoplasmic staining	Not performed	Expected staining
FAK	Human Placenta	Cytoplasmic>membranous staining in decidual and trophoblastic cells	Expected staining	Expected staining
	Human Spleen	No staining	Non-specific background staining	No staining
	Mouse Brain	Weak cytoplasmic>membranous staining	Not performed	Expected staining
	Human GBM (Xenograft)	Diffuse membranous and cytoplasmic staining	Not performed	Expected staining
p-FAK	Human Placenta	Cytoplasmic>membranous staining in decidual and trophoblastic cells	Expected staining	Expected staining
	Human Spleen	No staining	Non-specific background staining	No staining

Table 4.1 Staining patterns expected and seen in IHC and IF staining- ***continued from previous page***

Protein	Tissue	Expected Staining	Staining seen in IHC	Staining seen in IF
	Mouse Brain	Weak cytoplasmic>membranous staining	Not performed	Expected staining
	Human GBM (Xenograft)	Diffuse membranous and cytoplasmic staining	Not performed	Expected staining
HLA	Human Placenta	Diffuse staining of all cells	Expected staining	Expected staining
	Human Spleen	Diffuse staining of all cells	Expected staining	Expected staining
	Mouse Brain	No staining	No staining	No staining
	Human GBM (Xenograft)	Diffuse staining of all cells	Not performed	Expected staining
GLUT-1	Mouse Brain	Membranous staining of endothelial cells	Expected staining	Expected staining
	Human Placenta	Membranous staining of endothelial cells	Expected staining	Expected staining
	Human Spleen	Membranous staining of endothelial cells	Expected staining	Expected staining

4.2.2 Mulitplex IF Validation

Next, human spleen, human placenta and normal mouse brain were used to establish conditions for the multiplex IF assay. Throughout multiplex staining, the distribution patterns of each individual marker were consistent with those seen in IHC and uniplex IF assays. (Figure 4.8). HLA staining was observed diffusely in the human placenta and spleen sections, while no staining occurred in the mouse brain. GLUT-1 staining was observed around blood vessels in the human placenta, human spleen, and mouse brain. Both EGFR and p-EGFR strongly stained the membrane and cytoplasm in decidual and trophoblastic cells in the human placenta and minimally stained the normal mouse brain. Similarly, both FAK and p-FAK strongly stained the cytoplasm with moderate membranous staining in decidual and trophoblastic cells in the human placenta, and minimal staining in human spleen sections. FAK and p-FAK demonstrated weak cytoplasmic staining in the mouse brain.

4.2.3 Multiplex IF of Study Sections

Multiplex IF staining was performed on four human GBM in mouse xenografts (JK2, RN1, SJH1, and WK1). Whole sections of mouse brain of 5 μm thickness were stained and compared to Hematoxylin and Eosin (H&E) staining of adjacent cut sections from the same tissue blocks to confirm the location of tumour cells. The HLA staining was shown to be in agreement with the pattern of tumour cell distribution that was observed in the H&E staining, thus confirming the utility of HLA antibody to detect human tumour cells in mouse xenografts (Allaway et al. [2016], D'Souza et al. [2020], Lee et al. [2019]).

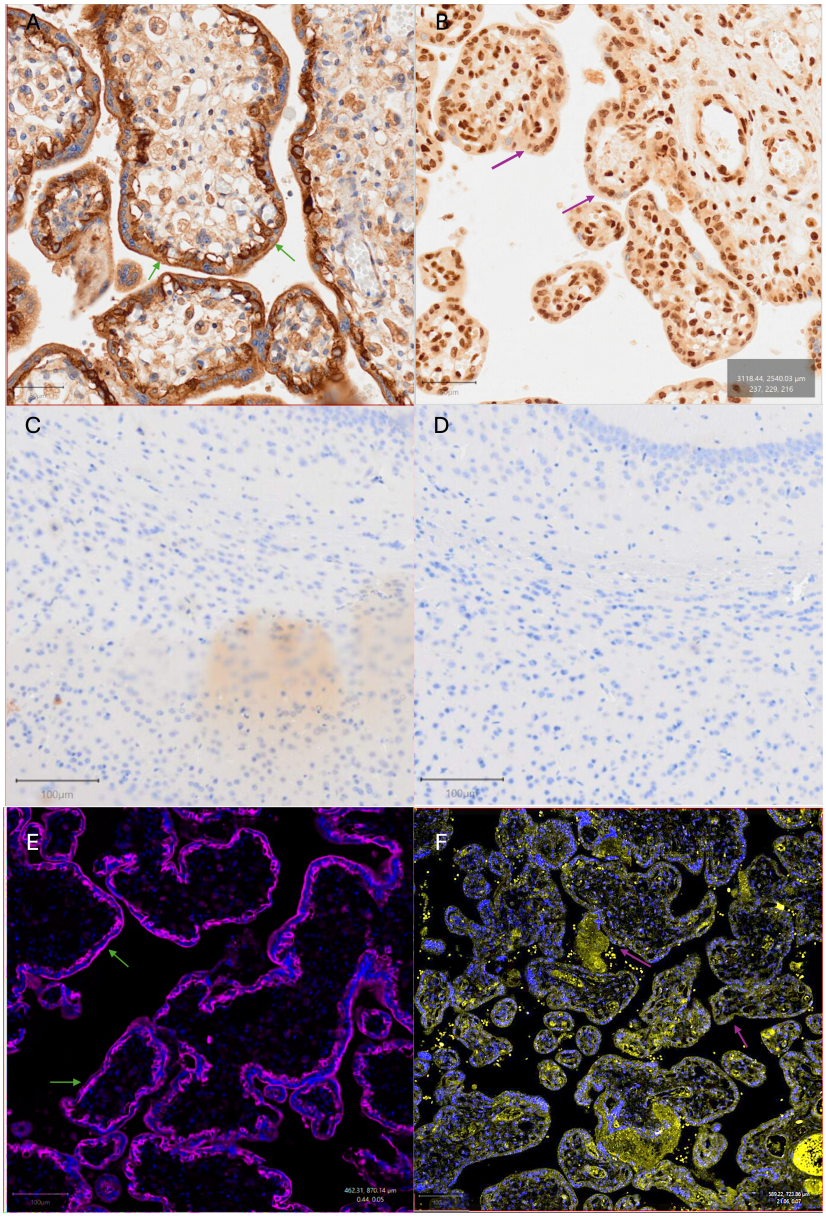

Figure 4.5: **IHC and Uniplex IF Validation of EGFR and p-EGFR Staining**

A) IHC staining of EGFR (brown pigment) on human placenta (positive control). Green arrows indicate membranous pattern of staining in trophoblast cells **B)** IHC staining of p-EGFR (brown pigment) on human placenta (positive control). Purple arrows indicate areas of cytoplasmic staining in trophoblast cells **C)** IHC staining of EGFR (brown) on normal mouse brain (negative control) showing only diffuse non-specific background staining **D)** IHC staining of p-EGFR (brown) on normal mouse brain (negative control). No staining seen **E)** Uniplex IF staining of EGFR on human placenta (purple staining). Green arrows indicate membranous pattern of staining in trophoblast cells **F)** Uniplex IF staining of p-EGFR on human placenta (yellow staining) Purple arrows indicate areas of cytoplasmic staining in trophoblast cells. All sections counter stained with the nuclear stain 4,6-diamidino-2-phenylindole (DAPI) (Blue). Scale bars A-B = 50 μm, C-F = 100 μm